LBNL-46423

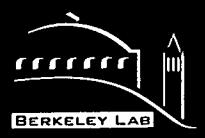

ERNEST ORLANDO LAWRENCE
BERKELEY NATIONAL LABORATORY

Complex Behavior in Simple Spin Systems

Seth D. Bush

Materials Sciences Division

May 1999

Ph.D. Thesis

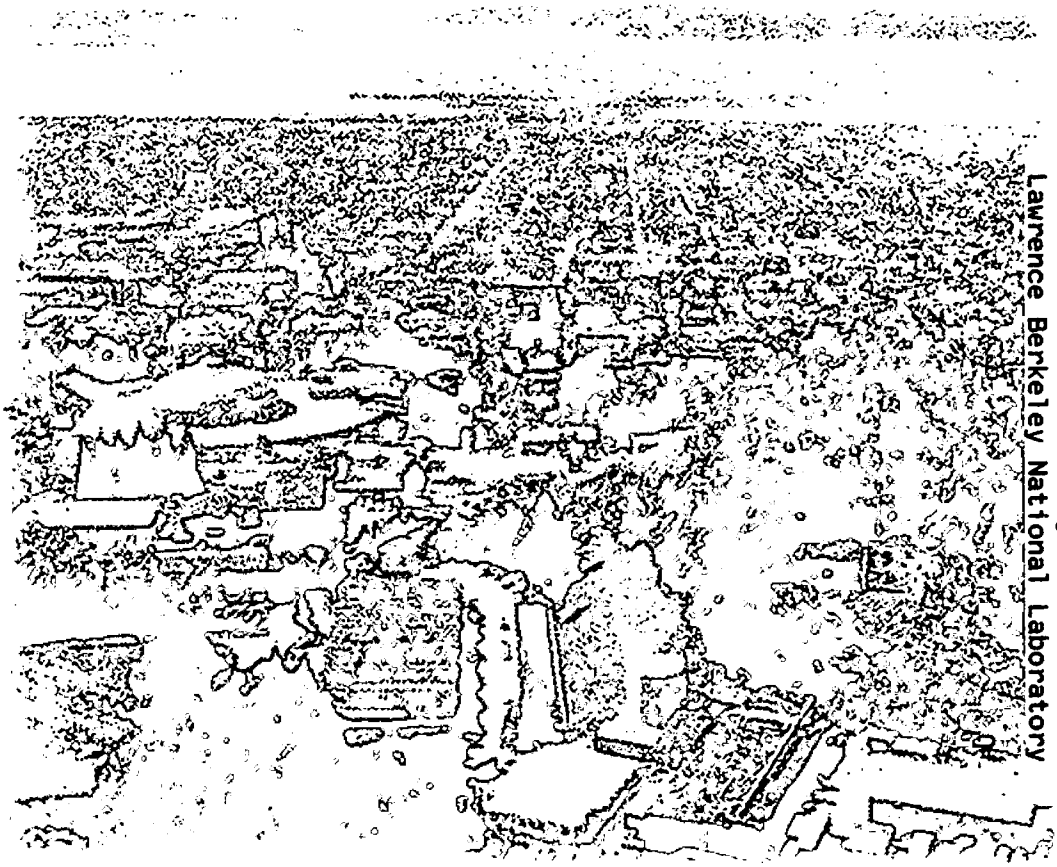

DISCLAIMER

LBNL-46423

Complex Behavior in Simple Spin Systems

Seth Daniel Bush
Ph.D. Thesis

Department of Chemistry
University of California, Berkeley

and

Materials Sciences Division
Ernest Orlando Lawrence Berkeley National Laboratory
University of California
Berkeley, CA 94720

May 1999

This work was supported by the Director, Office of Science, Office of Basic Energy Sciences, Materials Sciences Division, of the U.S. Department of Energy under Contract No. DE-AC03-76SF00098.

Complex Behavior in Simple Spin Systems

By

Seth Daniel Bush

B. A. (Reed College) 1994

A dissertation submitted in partial satisfaction of the

requirements for the degree of

Doctor of Philosophy

in

Chemistry

in the

GRADUATE DIVISION

of the

UNIVERSITY OF CALIFORNIA, BERKELEY

Committee in charge

Professor Alexander Pines, Chair

Professor Herbert Strauss

Professor Jeffrey Reimer

Spring 1999

Complex Behavior in Simple Spin Systems

by

Seth Daniel Bush

for Emmett and Anita

ACKNOWLEDGMENTS

It is hard for me to believe that it is time to write this section. It seems that only yesterday I was a prospective Pinenut, lost in the D level of Hildebrand. There are a number of people I would like to acknowledge for making this thesis possible. First I would like to thank Alex Pines for creating a fertile hub of scientific exchange and allowing me to be a part of it. I thank Dione Carmichael, the glue that holds the Pinenuts together, for her support, patience, and the occasional cookie.

One of the benefits of working in the Pines "Hub" is the sheer number of creative and talented people who pass through. During my time here I have had the good fortune of collaborating with a number of these world class scientists. I would like to thank: Matt Augustine for teaching me the ins and outs of gonzo science till dawn, Erwin Hahn for giving me new perspective on science and an introduction to the NMR community, David Rourke for having enough confidence in me to let me in on his pet project, George and Anya Kaiser for

donating their mother, Lana Kaiser, to science, and last but certainly not least, Matthias Ernst, Marco Tomaselli and Jay Shore, for being there to answer all my questions (no small task).

I would not be writing this today without the support of my family. I would like to thank my mother, Peggy Bush of Aptos, for being a constant source of encouragement and instilling in me the curiosity and tenacity that has got me here today. I would like to thank my grandparents Anita and Emmett Bush for always having confidence in me and showing me just how important family is.

Finally I would like to thank my friends and comrades who have seen me through my time in Berkeley. Thanks to: Andre Miller and Ryan Trump who offered me a safe haven to brew beer, play bridge, and pontificate on the inner workings of the world, Ray Wells who helped keep me grounded throughout this whole process, The Pinenuts who accepted me into the fold and made the lab my second home, and Bob Lamoreaux who kept me sane during my stints as head TA.

TABLE OF CONTENTS

ABSTRACT

Complex Behavior in Simple Spin Systems

by

Seth Daniel Bush

Doctor of Philosophy in Chemistry

University of California, Berkeley

Professor Alexander Pines, Chair

Research over the past five years has focused on using simple spin systems to develop interesting new nuclear magnetic resonance techniques in solid and liquid samples, as well as achieve substantial gains in both the contrast and resolution in magnetic resonance imaging. Specifically, this work reports on the development of soft radio frequency (RF) pulses that can be used to

selectively excite different spectral features as a function of transverse relaxation (T_2) properties. Soft RF pulses designed to selectively excite resonances with a specific physical property (e.g. resonance frequency) have found many applications in both magnetic resonance imaging and NMR. Here, research focused on the design and implementation of a new class of RF pulses that are sensitive to the relaxation properties of a sample. Soft RF pulses that create a final magnetization response that is parameterized as a function of T_2 and act as effective 'notch' filters for T_2 were designed by treating the solutions of the Bloch equations as an inverse scattering problem. Examples of one and two dimensional maps of proton density as a function of T_2 were obtained in model samples of aqueous $MnCl_2$ and $CuSO_4$ solutions.

A second project reported here in considers the highly non–linear interaction between the NMR detection coil and sample (radiation damping) to create a sensitive detector of magnetic resonance. This radiation damping is proportional to the current induced in the NMR detection coil following a RF pulse, a quantity dependent on the size of a sample's magnetization. This current produces a RF reaction field that drives the sample back towards equilibrium. Consequently, radiation damping is often viewed as a nuisance as it can broaden spectral features, thus lowering the overall resolution. In the course of developing a new theory for this phenomenon in an inhomogeneous magnetic field, it was realized that several new applications directed towards improving NMR detection sensitivity could be made. After a π pulse and under conditions of strong radiation damping, thermal noise in the NMR detection coil is capable of creating transverse magnetization that can feed back into the coil

and sample thus initiating a nonlinear and somewhat unexpected burst of signal. Using this phenomenon, one can in principle detect any signal, larger than the coil noise, as a perturbation on the burst induced by radiation damping. This idea was tested theoretically and experimentally in water and in solutions of ^{13}C labeled benzene in benzene. All of these experiments involved the design of several new pulse sequences specially tailored to use radiation damping instead of eliminating it.

The final thesis project investigates an apparent second-order recoupling of the chemical-shielding and dipolar-coupling tensors that occurs under magic angle spinning conditions when continuous wave decoupling is used in a simple two spin system. This second-order effect is investigated both theoretically and experimentally. This recoupling results in an information rich broadening that can be fit to determine the relative orientations of the chemical-shielding and dipolar-coupling tensors. Simple symmetric decoupling sequences will be presented which remove this recoupling leaving narrow spectral features with enhanced resolution.

CHAPTER 1

INTRODUCTION

1.1 Introduction

From its modest beginnings in 1946[1,2], nuclear magnetic resonance (NMR) has evolved to fill a central role in modern chemistry. Finding applications from material science to molecular biology, magnetic resonance has the ability to examine complex systems and return useful chemical information. Advances in NMR, like many other fields, come from the bottom up. Only through understanding the complex behavior of relatively simple systems can one hope to design experiments to gain insight into the chemistry of larger, more interesting, molecular systems. This thesis will report on three continuing avenues of research which seek to advance the field of NMR by exploring and exploiting the rich physics in simple model systems.

This thesis has been broken up into four sections. The first chapter will outline the basics concepts of NMR used throughout this text. For more detail the reader is referred to [3,4 and 5]. The second chapter will focus on the development and use of relaxation-selective radio-frequency pulses. The first relaxation-selective magnetic resonance images will be presented using a series of aqueous salt solutions. The next section will present our initial attempts at harnessing the non-linear nature of radiation damping to push the detection limitation of NMR. The final chapter will focus on the second-order recoupling of the chemical-shielding and dipolar-coupling tensors seen in a powdered sample of Tri(trideuteromethyl)-amine hydrochloride.

1.2 The Interactions

Following a time honored Pines lab tradition, this section will outline the interactions fundamental to NMR. One can begin by constructing a general NMR Hamiltonian as a sum of individual interaction Hamiltonians,

$$H_{NMR} = H_Z + H_{RF} + H_{CS} + H_D + H_J + H_Q. \qquad (1.1)$$

While useful as a launching platform, equation 1.1 gives no real physical insight into NMR. As such, to follow each interaction will be given its due.

1.2.1 Zeeman

The Zeeman interaction, H_Z, describes the direct coupling between a magnetic moment, $\vec{\mu}$, and an external magnetic field $\vec{B}$

$$H_Z = \hbar\vec{\mu}\cdot\vec{B} \tag{1.2}$$

In the special case where $\vec{B}$ is chosen to lie along the z-axis and $\vec{\mu}$ is the magnetic moment of a nuclear spin, $\vec{I}$, equation 1.2 becomes a scalar product,

$$H_Z = \gamma\hbar I_Z \cdot B_0 \tag{1.3}$$

Here we have chosen B_0 to define the z-axis and γ is the gyromagnetic ratio, an intrinsic property of a given nuclei. Taking the expectation value of H_Z, we can calculate the Zeeman energy, E_Z,

$$E_Z = \gamma\hbar B_0\langle I_Z\rangle, \tag{1.4}$$

where,

$$\langle I_Z\rangle = \langle m,I|I_Z|I,m\rangle = m,$$
$$m \in \{-I,-I+1,...,I-1,+I\}. \tag{1.5}$$

Here m is the azmuthal quantum number and I is the spin quantum number. For a spin 1/2 nucleus, such as ^1H or ^{15}N, m=±1/2, and E_Z becomes

$$E_Z = \pm\frac{1}{2}\gamma\hbar B_0. \tag{1.6}$$

This describes a two level system with $\Delta E_Z = \omega = \gamma\hbar B_0$, where ω is the Larmor frequency. In standard superconducting magnets, B_0 is on the order of 10 T (10^5 Gauss), E_Z is far and away the largest contribution to equation 1.1. As an example, for ^{15}N, γ = -2.7 x10^7rad/Tsec, ΔE_Z = -2.7 x 10^8 rad/sec or 43 MHz. As we will later see, the dipolar coupling energy for a directly bound ^{15}N-^1H (r=10.5 nm) spin pair is about 66 kHz. This is three orders of magnitude smaller than the Zeeman interaction.

Returning to the two level system above, for nuclei with a positive γ value, the lower energy level corresponds to spins that align parallel B_0 and the upper energy level corresponds to spins that align anti-parallel to B_0. The opposite is true for spins with negative values of γ. The sensitivity of NMR is proportional to the difference in population between the upper and lower energy levels. From Boltzmann statistics we know,

$$\frac{n_{low}}{N_{total}} = e^{-E_{low}/kT}, \tag{1.7a}$$

$$\frac{n_{hi}}{N_{total}} = e^{-E_{hi}/kT}. \tag{1.7b}$$

Where n_{low} and n_{hi} are the population of the lower and upper states respectively. We can then define P as the polarization, or population difference,

$$P = \frac{n_{low} - n_{hi}}{N_{total}}. \tag{1.8}$$

We can the expand equation 1.7a in a power series,

$$\frac{n_{low}}{N_{total}} = 1 - \frac{E_{low}}{kT} + \frac{\left(\frac{E_{low}}{kT}\right)^2}{2!} - \cdots. \tag{1.9}$$

Taking note of the fact that $E_{low} << kT$ we can truncate equation 1.9 to include only terms linear in kT. This simplification is known as the high temperature approximation and is used to describe most NMR experiments. A similar expansion and truncation can be made for equation 1.7b. We can now recast P as,

$$P \cong \frac{\Delta E}{kT}. \tag{1.10}$$

Returning to the example of ^{15}N spins in a 10 T field, at room temperature, the net polarization, is ~7 ppm or $7x10^{-6}$. In comparison to optical experiments where P≈1, NMR suffers from an inherently low sensitivity.

While the Zeeman Hamiltonian clearly plays a central role in the overall NMR experiment, by itself it holds very little structural information. The gyromagnetic ratio is inherently insensitive to its local environment and little information of chemical import can be gain from its measurement. NMR becomes a viable tool for determining local structure when one includes smaller interactions that are sensitive to local environment.

1.2.2 RF

So far we have noted that in the presence of a large external magnetic field, our spin system is split into two energy levels. Transitions between spin levels can be induced with the application of an oscillating magnetic field perpendicular to the static magnetic field. In practice this oscillating field is generated with a linearly polarized radio frequency (RF) field that is applied perpendicular to the static external magnetic field. The RF Hamiltonian can be written as,

$$H_{RF} = -2\gamma\hbar B_1 \cos(\omega t - \phi) I_X . \tag{1.11}$$

Where B_1 is the strength of a magnetic field RF component perpendicular to B_0, ω, is the Larmor frequency, and ϕ is the phase of the RF. Thus our Hamiltonian can be written as the sum of two terms, the time independent H_z and the time dependent H_{RF},

$$H = \omega_o I_Z - 2\gamma\hbar B_1 \cos(\omega t - \phi) I_X . \tag{1.12}$$

It is convenient to move into a reference frame where equation 1.12 is time independent. This is readily achieved if we choose a coordinate system that is rotating about the Z-axis at the frequency of the applied RF, ω. In this rotating frame of reference the RF contribution to the overall Hamiltonian appears static,

$$H_{Rot} = \Delta\omega I_Z - \gamma\hbar B_1\left(I_X\cos(\phi) - I_Y\sin(\phi)\right). \tag{1.13}$$

Here, $\Delta\omega = \omega_o - \omega$, where ω is the frequency of the rotating frame and the RF, and $\Delta\omega << \omega, \omega_o$. Let us now turn our attention towards chemical shielding.

1.2.3 Chemical Shielding

Chemical shielding describes the interaction between an applied magnetic field and the electronic environment surrounding a magnetic moment. If one imagines a bare spin 1/2 nucleus, the magnetic field felt by the spin is simply the applied magnetic field. For real chemical systems, the electronic cloud "shields" the nucleus from the external magnetic field. The actual field felt by a spin is dependent not only on the applied field but also the local electronic environment surrounding it. We can then write,

$$H_{CS} = \gamma\hbar\vec{I}\cdot\hat{\sigma}\cdot\vec{B}. \tag{1.14}$$

where $\hat{\sigma}$ represents the coupling between the magnetic field $\vec{B}$ and the spin vector $\vec{I}$. In its most general form, $\hat{\sigma}$ is a second rank tensor and can be described by a 3 x 3 matrix. As will be the case for many NMR interactions, moving into an irreducible tensor representation is helpful. For the case of chemical shielding in the laboratory frame, H_{CS} can be written as,

$$H_{CS} = \gamma\hbar\sum_{l=0}^{2}\sum_{m=-2}^{2}(-1)^{m} R_{l-m}^{CS} T_{lm}^{CS} \tag{1.15}$$

Where R_{l-m}^{CS} are spin-state independent coupling constants written in terms of the cartesian matrix elements of $\hat{\sigma}$ and T_{lm}^{CS} are tensors constructed from the spin vector $\vec{I}$ and the external magnetic field vector $\vec{B}$. Here l represents the tensor rank and m takes on values of $\pm$ l. For symmetric tensors, which all the interactions we will discuss are, the l = 1 terms are zero. The utility of spin tensor representation becomes apparent when we calculate our $R_{l-m}^{CS(lab)}$ values in the laboratory frame, from $R_{l-m}^{CS(pas)}$ in the principle-axis. Such a transformation can be readily achieved by using the Wigner rotation matrices [6].

$$R_{l-m}^{CS(lab)} = \sum_{n=-1}^{n=1} D_{n,-m}^{(1)} R_{l,n}^{CS(pas)} \tag{1.16}$$

Where $D_{n,-m}^{(l)}$ are the Wigner rotation matrices, and the reduced Wigner elements $d_{n,-m}^{(l)}$ for l=2 are outlined in table 1.1.

The principle-axis system (PAS) can be thought of as the Hamiltonian's "frame of reference". In the PAS $\hat{\sigma}$ is diagonal and can be written as,

$$\hat{\sigma} = \begin{pmatrix} \sigma_{xx} & 0 & 0 \\ 0 & \sigma_{yy} & 0 \\ 0 & 0 & \sigma_{zz} \end{pmatrix} \tag{1.17}$$

If we look at a powder pattern resulting from a chemical-shielding interaction in figure 1.1 we can determine each component σ_{nm} directly.

N M	2	1	0	-1	-1
2	$\frac{(1+\cos\beta)^2}{4}$	$-\frac{(1+\cos\beta)\sin\beta}{2}$	$\sqrt{\frac{3}{8}}\sin^2\beta$	$-\frac{(1-\cos\beta)\sin\beta}{2}$	$\frac{(1-\cos\beta)^2}{4}$
1	$\frac{(1+\cos\beta)\sin\beta}{2}$	$\cos^2\beta-\frac{(1-\cos\beta)}{2}$	$-\sqrt{\frac{3}{8}}\sin^2\beta$	$\frac{(1+\cos\beta)}{2}-\cos^2\beta$	$-\frac{(1-\cos\beta)\sin\beta}{2}$
0	$\sqrt{\frac{3}{8}}\sin^2\beta$	$\sqrt{\frac{3}{8}}\sin^2\beta$	$\frac{3(\cos^2\beta-1)}{2}$	$-\sqrt{\frac{3}{8}}\sin^2\beta$	$\sqrt{\frac{3}{8}}\sin^2\beta$
-1	$\frac{(1-\cos\beta)\sin\beta}{2}$	$\frac{(1+\cos\beta)}{2}-\cos^2\beta$	$\sqrt{\frac{3}{8}}\sin^2\beta$	$\cos^2\beta-\frac{(1-\cos\beta)}{2}$	$-\frac{(1+\cos\beta)\sin\beta}{2}$
-2	$\frac{(1+\cos\beta)^2}{4}$	$\frac{(1-\cos\beta)\sin\beta}{2}$	$\sqrt{\frac{3}{8}}\sin^2\beta$	$\frac{(1+\cos\beta)\sin\beta}{2}$	$\frac{(1+\cos\beta)^2}{4}$

Table 1.1 Reduce Wigner rotation matrix elements, taken from [6].

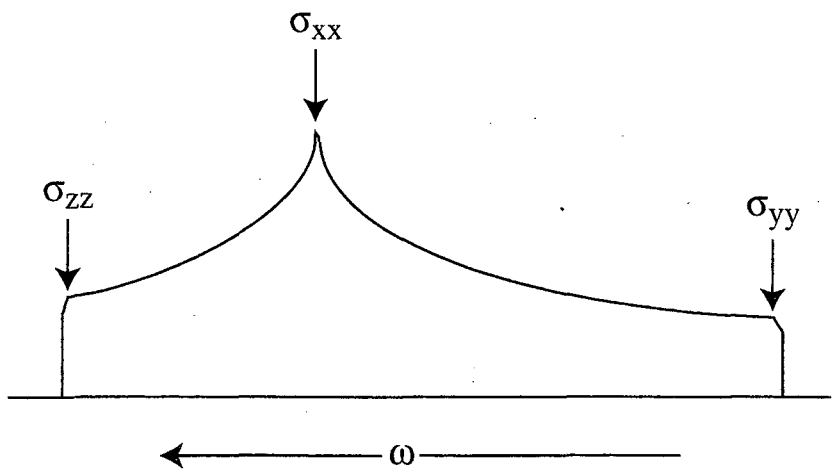

Fig 1.1 Cartoon of a typical asymmetric chemical shielding powder pattern. The three principle values, σ_{yy}, σ_{xx}, and σ_{zz} are sufficient to define the chemical shielding tensor in its principal axis system.

Here we have followed the convention $\sigma_{zz} \geq \sigma_{xx} \geq \sigma_{yy}$. We can write our $R_{l-m}^{CS(pas)}$ values in terms of the σ_{nm} components,

$$R_{0,0}^{CS(pas)} = \frac{1}{3}(\sigma_{xx} + \sigma_{yy} + \sigma_{zz}), \tag{1.18a}$$

$$R_{2,0}^{CS(pas)} = \sqrt{\frac{3}{2}}\left(\sigma_{zz} - \frac{1}{3}(\sigma_{xx} + \sigma_{yy} + \sigma_{zz})\right), \tag{1.18b}$$

$$R_{2,\pm 1}^{CS(pas)} = 0, \tag{1.18c}$$

$$R_{2,\pm 2}^{CS(pas)} = 1/2\left(\sigma_{yy} - \sigma_{xx}\right). \tag{1.18d}$$

Typically at this point one rewrites equations 1.18 a-d in terms of σ_{iso}, δ, and η where,

$$\sigma_{iso} = \frac{1}{3}(\sigma_{xx} + \sigma_{yy} + \sigma_{zz}), \tag{1.19}$$

$$\delta = \sigma_{zz} - \sigma_{iso}, \tag{1.20}$$

$$\eta = \frac{\sigma_{yy} - \sigma_{xx}}{\delta}. \tag{1.21}$$

Here, σ_{iso} is the isotropic chemical shift (observed in liquids), δ is know as the anisotropy parameter, and η is known as the asymmetry parameter. With these substitutions equations 1.18 a-d become

$$R_{0,0}^{CS(pas)} = \sigma_{iso}, \tag{1.22a}$$

$$R_{2,0}^{CS(pas)} = \sqrt{\frac{3}{2}}\delta, \tag{1.22b}$$

$$R_{2,1}^{CS(pas)} = 0, \tag{1.22c}$$

$$R_{2,2}^{CS(pas)} = \frac{1}{2}\delta\eta. \tag{1.22d}$$

Turning our attention to the spin portion of equation 1.15, we can write out our T_{lm}^{CS} values in the laboratory frame as,

$$T_{0,0}^{CS} = I_z B_0, \tag{1.23a}$$

$$T_{2,0}^{CS} = \sqrt{\frac{2}{3}} I_z B_0, \tag{1.23b}$$

$$T_{2,\pm 1}^{CS} = \mp \frac{1}{2} I_{\pm} B_0, \tag{1.23c}$$

$$T_{2,\pm 2}^{CS} = 0. \tag{1.23d}$$

Noting that the chemical shielding anisotropy is much smaller than the Zeeman contribution, we can move into the rotating frame and make the secular approximation. As such we keep only terms that commute with H_Z. Thus terms that contain $T_{2,\pm 1}^{CS}$ are dropped. Putting this all together we can recast equation 1.15 as,

$$H_{CS} = \gamma \hbar B_0 I_z \left(\sigma_{iso} + \frac{\delta}{2} \left(\left(3\cos^2 \beta - 1 \right) - \eta \sin^2 \beta \cos 2\alpha \right) \right). \tag{1.24}$$

Where β and α are Euler angles that result from a transformation of $R_m^{(l)PAS}$ to the laboratory frame. In liquids molecular motion averages β and α and equation 1.24 looses its angular dependence resulting in,

$$H_{CS} = \gamma \hbar B_0 I_z \sigma_{iso}, \tag{1.25}$$

an isotropic scalar quantity.

The chemical shielding interaction gives us our first taste of how NMR can be a useful structural tool. Chemical shielding is inherently sensitive to its local environment, and in solids carries with it an implicit orientational dependence. Our attention now will turn towards how spins interact with each other.

1.2.4 Dipolar Coupling

The dipolar-coupling interaction describes the through space coupling between two nuclear spins. Here we are interested in how one dipole moment affects a neighboring dipole moment. For a general spin system, H_D can be written as,

$$H_D = \frac{\hbar^2 \mu_0}{2\pi} \sum_j \sum_k \gamma_j \gamma_k \vec{I}_j \cdot \hat{D}_{jk} \cdot \vec{I}_k . \tag{1.26}$$

Where the summation accounts for each spin pair and $\hat{D}_{jk}$ is a second rank tensor describing the coupling between the j^{th} and k^{th} spin. Following our treatment of chemical shielding, we can move into a convenient spherical tensor representation. Limiting our discussion to the interaction of two spins, H_D in the laboratory frame can be written as,

$$H_D = \frac{\hbar^2 \gamma_I \gamma_S \mu_0}{2\pi} \sum_{l=0}^{2} \sum_{m=-2}^{2} (-1)^m R^D_{l-m} T^D_{lm} . \tag{1.27}$$

As with chemical shielding we can utilize the Wigner rotation matrices to transform R^{D}_{l-m} from the principle axis system to the laboratory frame,

$$R^{D(lab)}_{l-m} = \sum_{n=-1}^{n=1} D^{(l)}_{n,-m} R^{D(pas)}_{l,n} . \tag{1.28}$$

Here $D^{(l)}_{n,-m}$ are the Wigner rotation elements, not to be confused with $\hat{D}_{jk}$ the dipolar coupling tensor. Just as in the case of chemical shielding, the dipolar coupling tensor is symmetric and as such $l = 1$ terms are zero. Unlike the chemical shielding interaction, the dipolar coupling tensor $\hat{D}_{jk}$ is axially symmetric and traceless. In the PAS system we can write $R^{D(pas)}_{l-m}$ as,

$$R^{D(pas)}_{0,0} = R^{D(pas)}_{2,\pm1} = R^{D(pas)}_{2,\pm2} = 0, \tag{1.29a}$$

$$R^{D(pas)}_{2,0} = \sqrt{\frac{3}{2}} r^{-3} . \tag{1.29b}$$

Because the isotropic component of the dipolar coupling is zero, there is no direct manifestation of dipolar coupling in liquids. Continuing, we can write our two spin T^{D}_{lm} components as,

$$T^{D}_{0,0} = \vec{I} \cdot \vec{S}, \tag{1.30a}$$

$$T^{D}_{2,0} = \sqrt{\frac{1}{6}} \left(3 I_z S_z - \vec{I} \cdot \vec{S} \right), \tag{1.30b}$$

$$T^{D}_{2,\pm1} = \mp \frac{1}{2} \left(I_{\pm} S_z - I_z S_{\pm} \right), \tag{1.30c}$$

$$T^{D}_{2,\pm2} = \frac{1}{2} \left(I_{\pm} S_{\pm} \right). \tag{1.30d}$$

Noting that the dipolar interaction is several orders of magnitude smaller than the Zeeman interaction, we can again move into a rotating frame and make a secular approximation. Keeping only terms that commute with H_Z, i.e. terms proportional to $T^D_{2,0}$, equation 1.26 becomes,

$$H_D = \frac{\hbar^2 \gamma_I \gamma_S \mu_0}{2\pi r^3}(1-3\cos^2\beta)\left(3I_zS_z - \vec{I}\cdot\vec{S}\right), \tag{1.31}$$

where β is the angle between the z-axis defining the PAS and the z-axis of the laboratory frame set by the direction of B_0. For heteronuclear dipolar coupling, where $\vec{I},\vec{S}$ represent nuclei having very different larmor frequencies, the second portion of equation 1.31 simplifies to,

$$H_{D(het)} = \frac{\hbar^2 \gamma_I \gamma_S \mu_0}{\pi r^3}(1-3\cos^2\beta)\left(I_zS_z\right). \tag{1.32}$$

Of practical significance, dipolar coupling is dependent upon the internuclear distance between spins. Thus in our arsenal of structural tools, dipolar coupling can be used as a "molecular ruler". Because the isotropic portion of the dipolar coupling is zero, measurements of dipolar coupling in both liquids and solids under magic angle spinning conditions (to be discussed shortly), can only be achieved via indirect means.

1.2.5 J-Coupling

J-coupling describes the indirect coupling of nuclear spins mediated through the local electrons. Where dipolar coupling is a through-space interaction, J-Coupling is a through-bond interaction. We can write a J-Coupling Hamiltonian, H_J as,

$$H_J = \sum_j^N \sum_k^N I \cdot \hat{J}_{IS} \cdot S \tag{1.33}$$

Where in principle $\hat{J}_{IS}$ is a second rank tensor. In practice, the anisotropic portion of $\hat{J}_{IS}$ is negligible and only the isotropic portion of $\hat{J}_{IS}$ is kept. For a two spin system, $J = Tr\{\hat{J}_{IS}\}$, and equation 1.33 can be rewritten as,

$$H_j = J_{IS} I \cdot S \tag{1.34}$$

Isotropic J-couplings are on the order of 1-100 Hz so we can safely make a secular approximation, leaving,

$$H_j = J_{IS} I_z S_z \tag{1.35}$$

Because J-coupling is isotropic, it is not averaged away by the molecular motion in liquids and plays a central role in liquids NMR. However, due to the fact that J-couplings are relatively small compared to dipolar coupling and chemical shielding, it has to date found only limited use in the solid state.

1.2.6 Quadrupole

The last interaction that we will briefly outline is the electrical quadrupole moment. An asymmetric nuclear spin, I>1/2, couples to the electric field gradient at the site of the nucleus generating an orientational dependence. For a single spin in an external field we can write H_Q,

$$H_Q = \frac{eQ}{2I(2I-1)\hbar}\vec{I}\cdot\hat{V}\cdot\vec{I}. \qquad (1.36)$$

Where e is the elementary charge, Q is the quadrupole moment, and $\hat{V}$ is a second-rank tensor that describes the electric field gradient at the nucleus. Because spin-1/2 nuclei are symmetric they do not experience quadrupole coupling. The work presented in this chapter focuses on spin-1/2 particles and as such the quadrupole moment plays a very small role and further attention is eliminated.

1.3 Bloch Equations

The Bloch equations, developed by Felix Bloch in 1946 [7], provide a classical description of the evolution of a spin-systems' magnetization, **M**(t),

during a typical NMR experiment. In the absence of relaxation, the evolution of **M**(t) can be written as,

$$\frac{d\mathbf{M}(t)}{dt} = \gamma \mathbf{M}(t) \times \mathbf{B}(t) \quad . \tag{1.37}$$

We can write **M**(t) in terms of its components as,

$$\mathbf{M}(t) = \begin{pmatrix} M_x(t) \\ M_y(t) \\ M_z(t) \end{pmatrix} \tag{1.38}$$

Similarly we can write **B**(t) in terms of in its components as,

$$\mathbf{B}(t) = \begin{pmatrix} B_x(t) \\ B_y(t) \\ B_z(t) \end{pmatrix} . \tag{1.39}$$

Expanding equation 1.37 we obtain three differential equations, each describing the evolution of one of the components of **M**(t):

$$\frac{dM_x(t)}{dt} = \gamma M_y B_z - \gamma M_z B_y \quad , \tag{1.40a}$$

$$\frac{dM_y(t)}{dt} = \gamma M_z B_x - \gamma M_x B_z \quad , \tag{1.40b}$$

$$\frac{dM_z(t)}{dt} = \gamma M_x B_y - \gamma M_y B_x \quad . \tag{1.40c}$$

We can then make a number of simplifications. **B**(t) can be broken down into time-independent and time-dependent terms. The static magnetic field, B_0, and

the small "offsetting" magnetic field caused by the presence of the sample, $B_{off}(t)$, is time-independent and can be arbitrarily chosen to lie along the z-axis. The RF irradiation used to perturb the spin system from equilibrium is intrinsically time-dependent and can be represented as a small oscillating magnetic field, $B_{x,y}(t)$, with components, perpendicular to B_0. With this in mind we can write the components of **B**(t) as,

$$\gamma B_z(t) = \gamma B_o - \omega_{off}, \tag{1.41a}$$

$$\gamma B_x(t) = -\cos(\omega_{rf} t), \tag{1.41b}$$

$$\gamma B_y(t) = -\sin(\omega_{rf} t). \tag{1.41c}$$

Where we have substituted ω_{off} (the offset frequency) for γB_{off}, $\cos(\omega_{rf}t)$ (the real component of the applied RF field) for $\gamma B_x(t)$, and $\sin(\omega_{rf}t)$ (the imaginary component of the applied RF field) for $i\gamma B_y(t)$. We can further note that if we move into a frame of reference rotating at the Larmor frequency,

$$\gamma B_z(t) = -\omega_{off} \tag{1.42a}$$

$$\gamma B_x(t) = -\omega_{real}(t) \tag{1.42b}$$

$$\gamma B_y(t) = -\omega_{imag}(t) \tag{1.42c}$$

We can now incorporate the effects of relaxation into equation 1.40. Phenomenologically, we know that **M**(t) should tend towards its equilibrium state as t gets large,

$$\mathbf{M}(0) = \begin{pmatrix} 0 \\ 0 \\ M_0 \end{pmatrix}. \tag{1.43}$$

Consequentally, $M_X(t)$ and $M_Y(t)$ should tend towards zero with time, while $M_Z(t)$ should tend towards M_0. This evolution can be described with the following three differential equations, which introduce two time constants, T_1 and T_2,

$$\frac{dM_x(t)}{dt} = \frac{-M_x}{T_2}, \tag{1.44a}$$

$$\frac{dM_y(t)}{dt} = \frac{-M_y}{T_2}, \tag{1.44b}$$

$$\frac{dM_z(t)}{dt} = \frac{-(M_z - M_0)}{T_1}. \tag{1.44c}$$

T_1, or spin-lattice relaxation, involves the exchange of energy between the spin system and the lattice as the system returns to the equilibrium M_0 along z. This is in contrast to T_2, spin-spin relaxation, which involves only energy exchanges between spins in the system, during the systems return to its equilibrium M_X and M_Y.

We can now reconstruct equation 1.40 with the effects of relaxation, in matrix form as,

$$\frac{d}{dt}\begin{pmatrix} M_x(t) \\ M_y(t) \\ M_z(t) \end{pmatrix} = \begin{bmatrix} -\Gamma_2 & -\omega_{off} & \omega_{imag}(t) \\ \omega_{off} & -\Gamma_2 & -\omega_{real}(t) \\ -\omega_{imag}(t) & \omega_{real}(t) & -\Gamma_1 \end{bmatrix} \begin{bmatrix} M_x(t) \\ M_y(t) \\ M_z(t) \end{bmatrix} + \begin{bmatrix} 0 \\ 0 \\ M_0\Gamma_1 \end{bmatrix} \tag{1.45}$$

Here, Γ_1 and Γ_2 have been substituted for $1/T_1$ and $1/T_2$ respectively. This very general form of the Bloch equations will serve as a starting point for our discussion of the inverse scattering problem in section 2.2.1.

At this point a brief note about the relative magnitudes of the time constants T_1 and T_2 is in order. In general, $T_1 > T_2$. In the liquid state, as we will see in the next section, strong intermolecular interactions are averaged. This leads to T_1 and T_2 values on the order of 0.1 to 10 sec. On the other hand, in solids, where there are strong interactions between spins and hindered molecular motion, T_1 values are very long and can be anywhere from seconds to hours while T_2 values tend to be very short, in the msec regime.

1.4 Making Solid State Measurements

Making meaningful measurements in solid state can be difficult in multi spin systems. While the broad spectral features resulting from chemical shielding and dipolar coupling are information rich, they can be difficult to disentangle. With broad lines the potential for spectral overlap is high and overall resolution is correspondingly low. A further result of the broad line width is that the signal is spread out over a large spectral range, lowering the overall sensitivity. This section will outline some of the techniques used to overcome these resolution and sensitivity problems to make measurements in the solid state. In this section there is an implicit assumption that we are concerning ourselves with powdered samples. In a powdered sample we can envision small micro-crystals that have identical structure, but have random orientations with respect to the static magnetic field. While this section is by no

means comprehensive, it will describe the tools used for this study. We will begin by outlining "spin-space" averaging, or decoupling.

1.4.1 Decoupling

Continuous-wave decoupling (CW) is the simplest example of a spin-space averaging technique. Taking an ^{15}N-^{1}H spin pair, the CW decoupling experiment amounts to applying a long RF pulse at (or very near) the resonance of one of the spin species during acquisition. The spin species being irradiated precesses perpendicular to the RF field. Thus the spin pair evolves under a Hamiltonian reflecting both dipolar couplings and the RF field. If the decoupling field is stronger than the dipolar interaction, the dipolar coupling is dynamically averaged to zero. Conversely, if the decoupling field is weaker than the dipolar interaction, the second spin will evolve under a partially averaged dipolar coupling. More complicated decoupling schemes exist, and will be discussed as needed. A second means of gaining spectral resolution and sensitivity involves spatial averaging.

1.4.2 Magic Angle Spinning

Mechanical sample spinning offers a second means of spectral deconvolution. Dipolar coupling and chemical shielding both contain terms

which impart a spatial dependence upon the orientation of the spin's magnetic moment with respect to the external magnetic field,

$$H_D, H_{CSA} \propto (1 - 3\cos^2 \beta) \tag{1.46}$$

Again, β is the angle of the magnetic moment with respect to the external field B_o. There thus exists a "magic angle" where these interactions are averaged, when $(1 - 3\cos^2 \beta)=0$. This particular angle is 54.7°. Spinning a sample about a solid angle (in this case the magic angle) averages components that are not colinear with the rotor axis. This can be seen pictorially in figure 1.2.

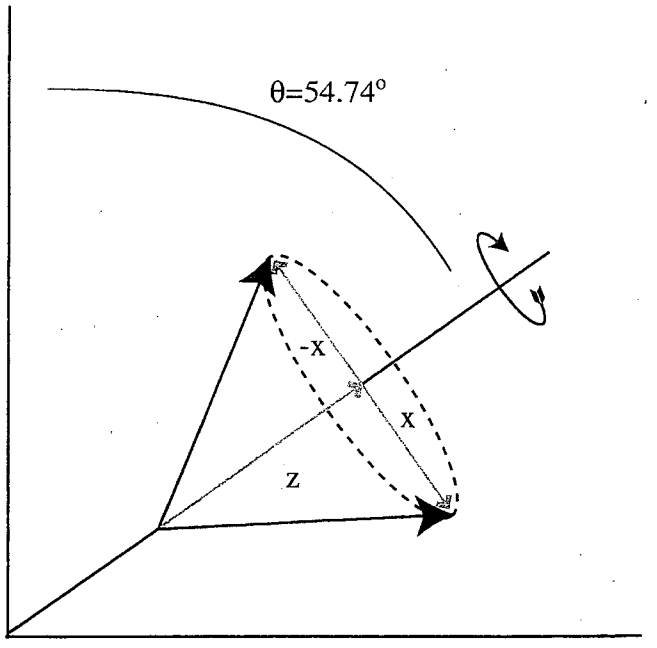

Figure 1.2 A an arbitrary crystallite spinning about an axis at the magic angle. The magnetization components perpendicular to the axis of rotation are averaged to zero while the magnetization components parallel to the axis of rotation are left unchanged.

Here we see that spinning averages the components of the magnetic moment that are not parallel to the spinning axis. The net effect spinning at the magic angle is to incline, on average, all the magnetic moments at the magic angle. This results in an averaging of both chemical shielding and dipolar coupling.

As with spin decoupling, when the magic angle spinning speeds are larger than the interaction being averaged, one sees complete averaging and is left with only isotropic contributions. In the case of dipolar coupling this is observed to be zero. For chemical shielding this is the isotropic chemical shift. Again, when the spinning speed is less that the interactions being averaged, we see only a partial averaging. This results in series of lines separated by the spinning speed or spinning side bands. Next our attention will turn towards techniques which clarify spectra by simplifying the spin-systems being observed.

1.4.3 Isotropic Enrichment

Isotropic enrichment allows one a direct means of increasing sensitivity in heteronuclear (^{13}C and ^{15}N) experiments. At natural abundance, ^{13}C and ^{15}N, the spin 1/2 species commonly used in NMR, compose only 1.1% and 0.37% of the carbon and nitrogen in the sample. By artificially enriching samples with spin active isotopes one raises the number of active spins in the system and hence the overall sensitivity of the experiment.

Often complete isotropic enrichment is spectrally cumbersome. One introduces a multitude of coupling that may lower the overall resolution of the

spectrum with the addition of extra active spins. Site selective isotropic enrichment is one means of both increasing sensitivity and resolution. With site selective enrichment specific sites within a given molecule are enriched. This has the effect of making these sites more sensitive than their un-labeled counterparts and as such increase the over all resolution.

1.4.4 Cross Polarization

The final solid state NMR tool that we will address is cross-polarization. Before we delve into the mechanics of cross-polarization, let us develop a qualitative picture. From 1.2.1, we know that the overall sensitivity of a nuclei is proportional to it gyromagntic ratio, γ. As γ is raised the energy difference between the "spin up" and "spin down" energy levels increases (at constant temperature) the net polarization increases. This polarization dictates the overall sensitivity of a nucleus. In comparing spins with different γ values, one could describe a system of nuclei with a high γ and correspondingly high polarization, as a "cool" spin reservoir. Similarly a low γ spin system could be described in relative terms as a "hot" spin reservoir. This thermodynamic analogy is known as the spin-temperature hypothesis[8]. The spin-temperature hypothesis is predicated on the notion that for times t such that $T_2<t<T_1$ the probability of finding a spin in a given energy level is dictated by the Boltzmann distribution. The Boltzmann distribution in turn dictates the spin temperature, T_s. This type of thermodynamic description can be immediately useful. If two thermal reservoirs are placed in contact, at equilibrium they will reach a common

temperature. In terms of spin systems this can lead to a sensitivity enhancement for the spins that were initially "hot".

Cross polarization describes experiments that establish a contact between a "cold" spin reservoir and a "hot" spin reservoir. With this contact the reservoirs equilibrate, effectively "cooling" one spin system and increasing its sensitivity. This contact is mediated through the dipolar coupling and depicted graphically in figure 1.3.

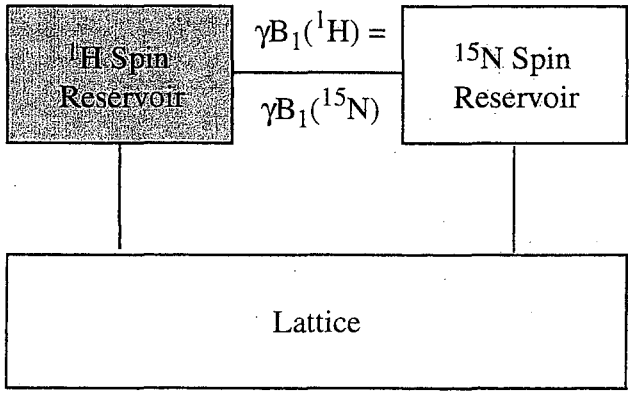

Figure 1.3 Cross polarization block diagram. The ^{1}H and ^{15}N spin reservoirs are normally only coupled to each other via the lattice. When a RF field is places on both the carbon and the proton spin systems such that the Hartmann-Hahn condition [9] is matched, the spin reservoirs can mix. This effectively "cools" the carbon reservoir while "warming" the proton reservoir.

For our purposes we will be discussing ^{1}H-^{15}N cross polarization in which the overall sensitivity of the ^{15}N spins is increased by transferring polarization from the ^{1}H to the ^{15}N. The question then becomes, how does one allow these reservoirs to mix.

Effective thermal contact can occur between two spin reservoirs I and S when the Hartman-Hahn[9] condition is met such that,

$$\gamma_I B_{1I} = \gamma_S B_{1S}, \tag{1.47}$$

where B_{1I} and B_{1S} are the strengths of the oscillating RF field applied to each nuclei. This describes a situation where, in the double-rotating frame, each species is nutating at the same frequency. During this mixing time the spin polarizations begin to equilibrate. With a sufficiently long mixing time, the spin temperature of each spin species is equilibrated. A general pulse sequence can be seen in figure 1.4.

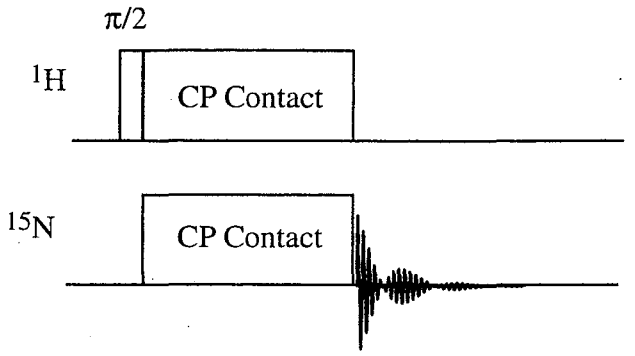

Figure 1.4 Simple Hartmann-Hahn cross polarization sequence.

Here we see that after a $\pi/2$ degree pulse on the I spins, an effective field of B_{1I} and B_{1S} are applied to I and S, respectively, to initiate the cross-polarization thermal contact. In the case of ^{1}H-^{15}N spin pair, $B_1{}^{15}$N ~10* $B_1{}^1$H. Under ideal conditions, one can expect an ^{15}N sensitivity enhancement of 500%.

An indirect advantage of the cross polarization technique is seen when one signal averages many spectra. The delay between acquisitions is mandated by the time it takes the system to return to its equilibrium magnetization. Because the polarization being monitored is transferred from the ^{1}H spin bath, the recycle delay is dictated by the ^{1}H relaxation dynamics. In general the ^{1}H relaxation times are much faster than ^{15}N (or ^{13}C) relaxation times. As such, under cross polarization conditions, one is able to take more acquisitions in a given amount of time than under directly detected conditions. This has the effect of reducing experiment time, and increasing the signal to noise. The later statement is a direct result of the fact that when signal averaging, the signal-to-noise scales as the square root of the number of acquisitions.

REFERENCES

1. E. M. Purcell, H. C. Torrey, and R. V. Pound, *Phys. Rev.*, 69, 37 (1946).

2. F. Bloch, W. W. Hansen, and M. Packard, *Phys. Rev.*, 70, 474 (1946).

3. R. R. Ernst, G. Bodenhausen, and A. Wokaun, *Principles of Nuclear Magnetic Resonance in One and Two Dimensions*, (Clarendon Press, Oxford, 1992).

4. C. P. Slichter, *Principles of Magnetic Resonance*, (Springer, Berlin, 1996).

5. J. Cavanagh, W. J. Fairbrother, A. B. P. III and N. J. Skelton, *Protein NMR Spectroscopy*, (Academic Press, Inc., San Diego, 1996).

6. U. Haeberlen, *High Resolution NMR in Solids – Selective Averaging*, (Academic Press, New York, NY, 1976).

7. F. Bloch, *Phys. Rev.*, 70, 460 (1946).

8. M. Goldman, *Spin Temperature and Nuclear Magnetic Resonance in Solids*, (Clarendon Press, Oxford, 1970).

9. S. R. Hartmann and E. L. Hahn, *Phys. Rev.*, 128, 2042 (1962).

CHAPTER 2

T_2-SELECTIVE PULSES; INVERSION OF THE BLOCH EQUATIONS

2.1 Introduction to Magnetic Resonance Imaging

Over the past few years considerable progress has been made towards improving Magnetic Resonance Imaging (MRI) as both an analytical imaging tool and as a non-invasive medical diagnostic [1,2]. The basic MRI experiment relies on the fact that, for a nucleus with a non-zero spin such as ^1H in water, the resonance frequency, ω, is linearly dependent upon the size of the external magnetic field, $\mathbf{B}_o$,

$$\omega = \gamma B_o, \tag{2.1}$$

where γ is the gyromagnetic ratio. With the incorporation of a magnetic field gradient, **G**, a spatial dependence can be imparted upon the resonance frequency,

$$\omega(r) = \gamma B_o + \mathbf{G} \cdot \mathbf{r} \tag{2.2}$$

In this manner, one is able to create a map of spin density as a function of position.

One of the drawbacks of the basic magnetic resonance spin density imaging scheme is that it is intrinsically non-selective. As can be seen in figure 2.1, it is often difficult to image one spin species in the presence of a second. In this example we have depicted an imaging phantom with two parallel sample tubes. Each tube has a different spin species. In the idealized case, figure 2.1a, each spin species has nearly the same resonance frequency and relaxation times. As such, imaging either tube in 2.1a is rather straight forward. In the more realistic case, 2.1b, each tube has a spin species with different physical characteristic. As is readily apparent, the species depicted by the lighter shade, has faster relaxation properties (broader line) and a different chemical shift than the species depicted by the darker shade. In constructing an image, all spins within a given resonance frequency range will be lumped together to give a local spin density. Such background spin density often masks the spins of interest, making imaging problematic. This is seen in the image depicted in figure 2.1b. To combat this a number of techniques have been developed to create spin selective images [3,4,5].

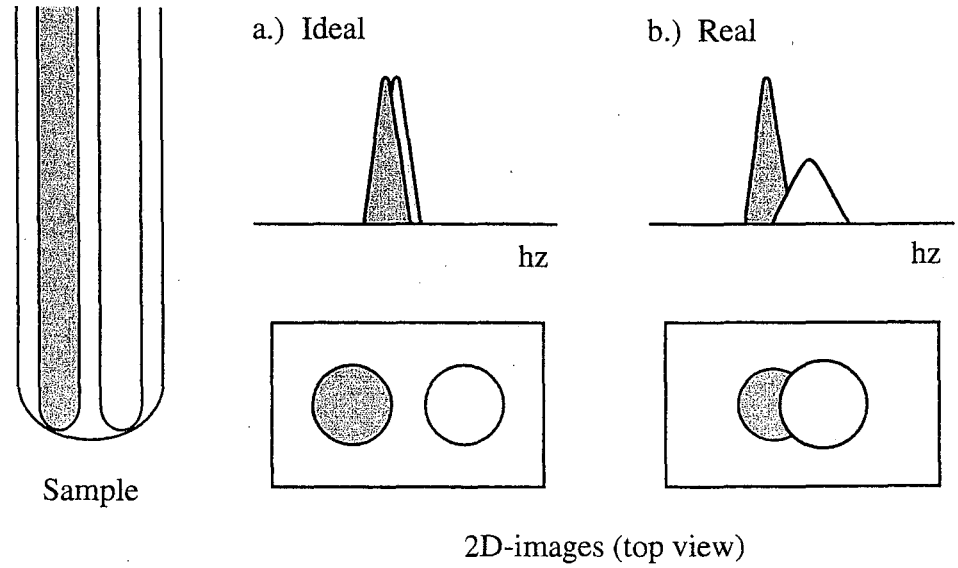

Figure 2.1 Cartoon of a simple imaging experiment. The sample phantom consists of two parallel tubes, containing potentially different spin systems. a.) depicts a mock spectrum and 2D-image of an idealized system. Here each spin system has almost the same physical characteristics. b.) depicts a mock spectrum and 2D-image of a more realistic system where the physical properties of each spin system are different.

Differences in resonance frequency offer one means of creating spin selective images. Two examples of frequency selective excitation are depicted in figure 2.2. To first order, the frequency excitation profile of a RF pulse is simply the Fouier transform of the pulse profile. Thus, the longer an excitation pulses is made, the narrower its excitation profile becomes. This leads to the use of long low-power soft pulses. Clearly these techniques work best for species with very different resonance frequencies. This can become a practical problem for typical medical imaging experiments that operate at low external magnetic field strengths. Under these conditions there is little chemical shift dispersion.

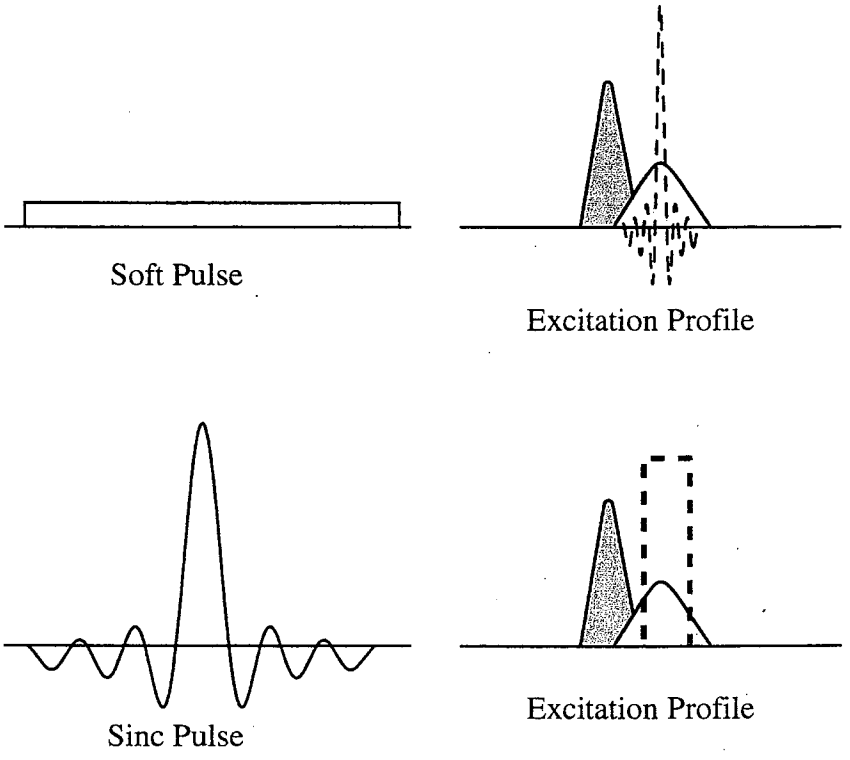

Figure 2.2 Frequency selective pulses and their resultant excitation profiles.

Externally introduced agents offer a second means of spin density contrast. These fall into two categories: those which alter their local environment, such as the addition of Ga^{3+} which augments local relaxation dynamics[6], and those which function as "spies" such as polarized noble gases[7] and fluorine-rich compounds such as C_2F_4 [8], which offer a selective group of spins to image. These techniques have the advantage that they enable one to include only spins of interest in a given spin density image. A disadvantage inherent in many of these techniques is that using ex-vivo agents may detract from the relative non-invasiveness of the basic MRI experiment.

A third method for creating differential spin images relies on the use of the relaxation dynamics of the spins as an internal contrast agent [9]. As

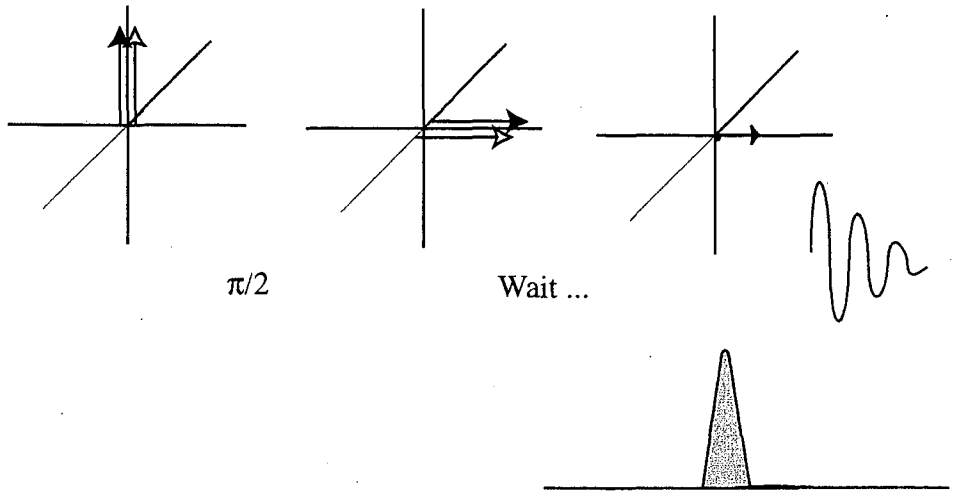

Figure 2.3 Vector diagrams for experiments that incorporate a "wait" period to differentiate spins with different relaxation properties. The vectors with the shaded arrow heads represent a species with slow relaxation dynamics and the vectors with open arrow heads represent species with fast relaxation dynamics, corresponding to the dark and light species depicted in figure 2.1. The cartoon below each experiment is a mock spectrum in which magnetization from the fast relaxing species has been removed.

outlined in section 1.3, after excitation, the return to equilibrium for an ensemble of spins, can be described by two exponential relaxation processes: spin-lattice relaxation, T_1, and spin-spin relaxation, T_2. Relaxation differentiation is achieved by incorporating a "wait" domain in the basic MRI experiment. For example, for spins differentiated by T_2, during this wait period, spins that relax quickly are nulled leaving only spins with slow relaxation to add to the overall spin density image [3,10]. A series of vector diagrams that outline the fundamental of T_2 weighted experiments are shown in figure 2.3.

While these relaxation-weighting techniques offer a non-invasive means of selecting which spins are imaged, this selectivity is quite inflexible. They can act either as a 'high pass' or a 'low pass' filter, removing signal from spins with relaxation parameters below or above a certain threshold. These methods then tend to be quite inflexible when imaging one spin species in the presence of two or more other spin species, where each species has unique relaxation behavior. A second disadvantage of these relaxation-weighted techniques is that during the "wait" domain, one is throwing away signal. For many MRI experiments, one is limited by signal-to-noise and thus the use of these relaxation weighting techniques becomes problematic.

Presented in this chapter are the first relaxation *selective* images. Using theory detailed in the next section, in which the inversion of the Bloch equations is treated as a scattering problem, we were able to design and implement T_2-selective RF pulses for imaging. These RF pulses create a final magnetization response that is parameterized as a function of T_2, and as such act as effective 'notch' filters for T_2. To follow will be a brief explanation of the theory behind the pulse design, a description of our experiment and our results compared to theory.

2.2 Theory

This section will outline how inversion of the Bloch equations was used to create T_2-selective pulses. It will start by introducing scattering theory. Then it will show how the Bloch equations can be written as an invertible scattering problem. Finally, it will describe how this process was used to

create relaxation-selective pulses capable of creating a final magnetization parameterized by T_2. For a more detailed discussion of this theory the reader is refereed to [11].

2.2.2 Scattering Theory

Prior to launching into a description of the inner workings of inverse scattering theory, it would be fruitful to pause and address what we hope to gain by inverting the Bloch equations. To do this we will first develop a qualitative picture of the forward scattering problem.

The coupling of the Sun's light and the Earth's atmosphere is a classic example of a scattering problem. The apparent white light of the Sun is "scattered" by Earth's atmosphere leaving, on a clear day, blue skies. We can depict this more generally in figure 2.4.

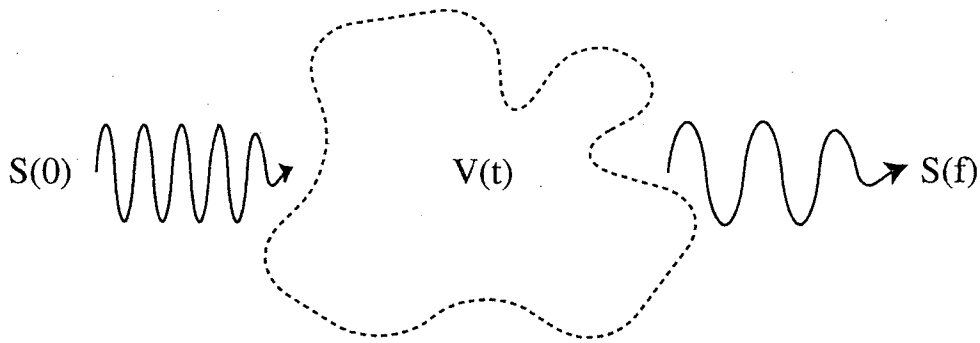

Figure 2.4 A graphical depiction of the general scattering problem. S(0) is the initial state of the system, S, V(t) is the potential the system is passed through and S(f) is the final state of the system. We have neglected to include the back scattered contribution.

Here we see that our system, S, which corresponds to the Sun's light, begins in an initial state, S(0), or white light. It is then passed through, a potential V(t), the atmosphere, leaving the system in a state S(f), in our example the blue we see on a clear day. The forward scattering problem amounts to determining the S(f), given S(0) and V(t). The inverse scattering problem is to determine V(t) given S(0) and S(f). Extending the example of Sun's light and the Earth's atmosphere, the inverse scattering problem would ask, given the white light of the sun, and the fact that I want to observe a sunset with green, red and purple, what contaminants should I place in the Earth's atmosphere? Where this becomes of practical interest is when one chooses a clever S(f).

Inverse scattering theory allows the "inversion" of systems of the form,

$$\frac{\partial \Phi}{\partial t} = \left[i\xi \mathbf{J} + V(t) \right] \Phi(\xi, t) \tag{2.1}$$

where $\Phi(\xi,t)$, $\mathbf{J}$, and $\mathbf{V}(t)$ are n x n matrices, and ξ is a scalar (the scattering parameter). Given initial and final values of Φ as functions of ξ, inverse scattering theory allows the determination of $\mathbf{V}(t)$ [12]. This inversion is particularly straightforward for "pure-soliton" type systems, where $\mathbf{V}(t)$ may be determined (in principle, in closed-form) using the dressing method [13].

2.2.1 Recasting the Bloch Equations

As introduced in section 1.3, the Bloch equations offer a classical description of the evolution of the bulk magnetization of a spin system

during a typical NMR experiments. In matrix form we wrote the Bloch equation as,

$$\frac{d}{dt}\begin{pmatrix} M_x(t) \\ M_y(t) \\ M_z(t) \end{pmatrix} = \begin{bmatrix} -\Gamma_2 & -\omega_{off} & \omega_{imag}(t) \\ \omega_{off} & -\Gamma_2 & -\omega_{real}(t) \\ -\omega_{imag}(t) & \omega_{real}(t) & -\Gamma_1 \end{bmatrix} \begin{bmatrix} M_x(t) \\ M_y(t) \\ M_z(t) \end{bmatrix} + \begin{bmatrix} 0 \\ 0 \\ M_z(0)\Gamma_1 \end{bmatrix}. \tag{2.2}$$

This very general form of the Bloch equations will serve as a starting point for our discussion of the inverse scattering problem. Since we will want to design "relaxation-selective pulses", it is helpful to separate out the relaxation terms in this equation. This gives,

$$\frac{d}{dt}\begin{pmatrix} M_x(t) \\ M_y(t) \\ M_z(t) \end{pmatrix} = \left[\begin{bmatrix} -\Gamma_2 & 0 & 0 \\ 0 & -\Gamma_2 & 0 \\ 0 & 0 & -\Gamma_1 \end{bmatrix} + \begin{bmatrix} 0 & -\omega_{off} & \omega_{imag}(t) \\ \omega_{off} & 0 & -\omega_{real}(t) \\ -\omega_{imag}(t) & \omega_{real}(t) & 0 \end{bmatrix}\right] \begin{bmatrix} M_x(t) \\ M_y(t) \\ M_z(t) \end{bmatrix} + \begin{bmatrix} 0 \\ 0 \\ M_z(0)\Gamma_1 \end{bmatrix}. \tag{2.3}$$

Which looks somewhat like equation 2.1, here a relaxation matrix has taken the place of **J** and the potential **V**(t) is the driving fields or the ω terms.

To get equation 2.3 into a form that we can easily invert we need to make four simplifications. First we will assume that $T_1 >> T_2$. Experimentally in the samples used in this work, T_1 tended to be ~5 x T_2, so this assumption is justified. Then we assume that we are on resonance and that we are only using a real RF source. Thus $\omega_{off} = \omega_{imag} = 0$. Finally we note that at equilibrium our initial magnetization is along the Z axis and is $M_Z(0)$. Thus equation 2.3 becomes,

$$\frac{d}{dt}\begin{pmatrix} M_x(t) \\ M_y(t) \\ M_z(t) \end{pmatrix} = \begin{bmatrix} -\Gamma_2 & 0 & 0 \\ 0 & -\Gamma_2 & -\omega_{real}(t) \\ 0 & \omega_{real}(t) & 0 \end{bmatrix} \begin{bmatrix} M_x(t) \\ M_y(t) \\ M_z(t) \end{bmatrix}. \tag{2.4}$$

This further simplifies when we note that initially, i.e. at t=-∞, $M_X$is zero and hence $M_X = 0$ for all time. Also, the behavior of M_Y and M_Z does not depend on M_X, thus,

$$\frac{d}{dt}\begin{pmatrix} M_y(t) \\ M_z(t) \end{pmatrix} = \begin{bmatrix} -\Gamma_2 & -\omega_{real}(t) \\ \omega_{real}(t) & 0 \end{bmatrix} \begin{bmatrix} M_y(t) \\ M_z(t) \end{bmatrix}. \tag{2.5}$$

Hence,

$$\frac{d}{dt}\left(e^{\Gamma_2 t/2}\begin{pmatrix} M_y(t) \\ M_z(t) \end{pmatrix}\right) = \begin{pmatrix} M_y(t) \\ M_z(t) \end{pmatrix}\frac{d}{dt}e^{\Gamma_2 t/2} + e^{\Gamma_2 t/2}\frac{d}{dt}\begin{pmatrix} M_y(t) \\ M_z(t) \end{pmatrix}. \tag{2.6}$$

But,

$$\begin{pmatrix} M_y(t) \\ M_z(t) \end{pmatrix}\frac{d}{dt}e^{\Gamma_2 t/2} = \frac{\Gamma_2}{2}\left(e^{\Gamma_2 t/2}\begin{pmatrix} M_y(t) \\ M_z(t) \end{pmatrix}\right) = \begin{bmatrix} \frac{\Gamma_2}{2} & 0 \\ 0 & \frac{\Gamma_2}{2} \end{bmatrix}\left(e^{\Gamma_2 t/2}\begin{bmatrix} M_y(t) \\ M_z(t) \end{bmatrix}\right), \tag{2.7}$$

and, from equation 2.5,

$$e^{\Gamma_2 t/2}\frac{d}{dt}\begin{pmatrix} M_y(t) \\ M_z(t) \end{pmatrix} = \begin{bmatrix} \frac{-\Gamma_2}{2} & -\omega_{real}(t) \\ \omega_{real}(t) & 0 \end{bmatrix}\left(e^{\Gamma_2 t/2}\begin{bmatrix} M_y(t) \\ M_z(t) \end{bmatrix}\right). \tag{2.8}$$

Hence equations 2.6, 2.7, and 2.8 yield,

$$\frac{d}{dt}\left(e^{\Gamma_2 t/2}\begin{pmatrix}M_y(t)\\M_z(t)\end{pmatrix}\right)=\begin{bmatrix}\frac{-\Gamma_2}{2} & \omega_{real}(t)\\ -\omega_{real}(t) & \frac{\Gamma_2}{2}\end{bmatrix}\left(e^{\Gamma_2 t/2}\begin{bmatrix}M_y(t)\\M_z(t)\end{bmatrix}\right) \tag{2.9}$$

This is a special case of the Zakharov-Shabat (ZS) eigenvalue problem[13],

$$\frac{dv}{dt}=\begin{bmatrix}-i\xi & q^*(t)\\ -q(t) & i\xi\end{bmatrix}v \tag{2.10}$$

identifying $\xi=-i\Gamma_2/2$ and $q(t)=q^*(t)=\omega_{real}$ where * mean complex conjugate.

The ZS problem has been extensively studied both as a forward problem, where the behavior of v is determined, given the parameter ξ and function q(t), and as an inverse problem. Here, the behavior of v is specified by giving the "scattering data" of the system. For each set of scattering data, a "potential" q(t) may be uniquely determined [13,14,15,16]. Thus given an M(0) and a M(f), a real RF pulse $\omega_{real}(t)$, can be constructed that takes us from M(0) to M(f).

2.2.3 Choosing M(f)

To achieve T_2 selectivity, we chose a M(f) that was parameterized as a function of T_2. M(f) was chosen to be,

$$M(f)=\begin{bmatrix}0\\0\\ \prod_{j=1}^{r}\frac{\Gamma_2-g_j}{\Gamma_2+g_j^*}\end{bmatrix} \tag{2.11}$$

Parameters g_j may be chosen arbitrarily, as can the number of parameters, r, except that all g_j must be in the right half complex plane, and any g_j off the real axis must be in a (g_j,g_j^*) pair. For such final responces, the inverse scattering problem can be solved using a tool from scattering theory – the "dressing method." [13]. Hence a pulse corresponding to responses of equation 2.11 will be referred to as an r^{th} order dressing pulse.

Figure 2.5 gives a geometric picture of how spin species with different T_2 values evolve during a selective pulse. The magnetization of each T_2 species is moved by the pulse from its initial value, taken to be (0,0,1) to a final scaled value along the z-axis.

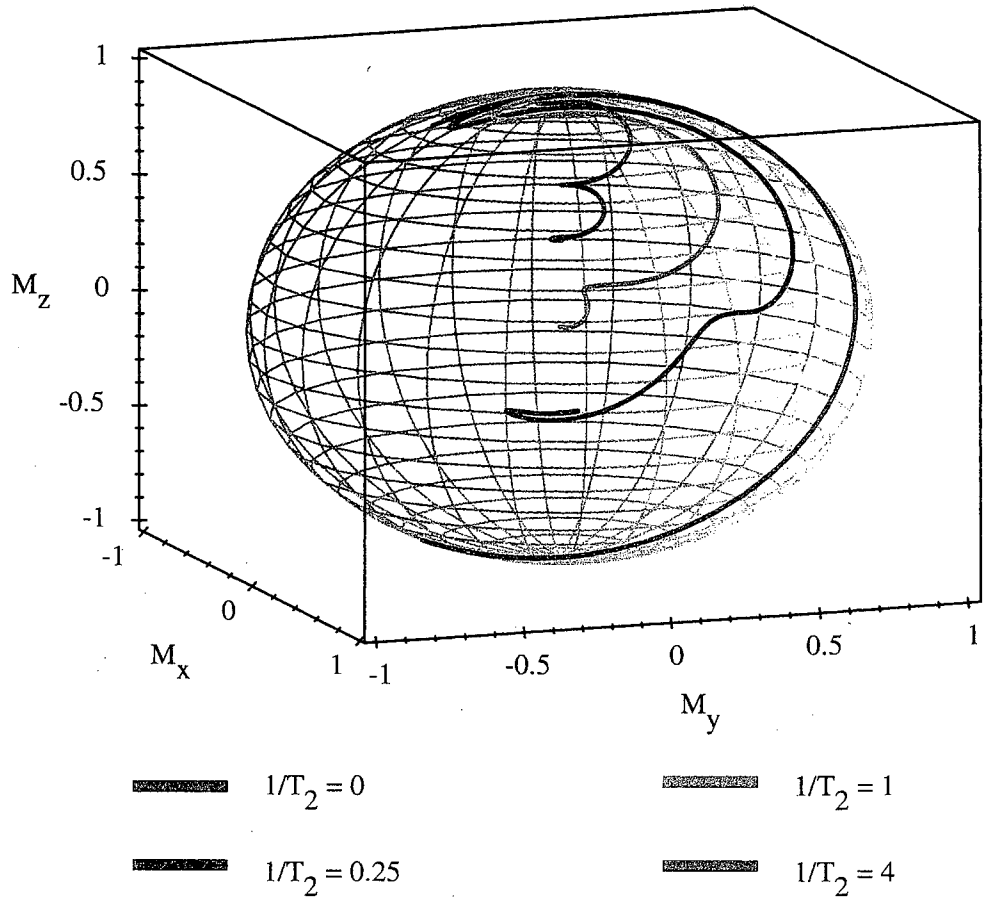

Figure 2.5 Theoretical plots of **M** for a series of T_2 species, during a third order dressing pulse designed to null a species with a T_2 of 1 msec. The trajectory of each species is plotted on a unit sphere.

The final magnetization is therefore encoded according to its T_2 relaxation time. For a particular T_2, which may be chosen as desired, the final magnetization is zero, and this spin species is "nulled" by the pulse. A second spin species will have a non-zero M(f), the size of which is determined by the "filter-function" given in equation 2.12. Optimizing the M(f) becomes a question of optimizing the values of the g_j parameters.

Figure 2.6 shows a theoretical plot of the final M_z as a function of T_2 for

a third order dressing pulse designed to selectively null a species with a T_2 of 6.5 msec.

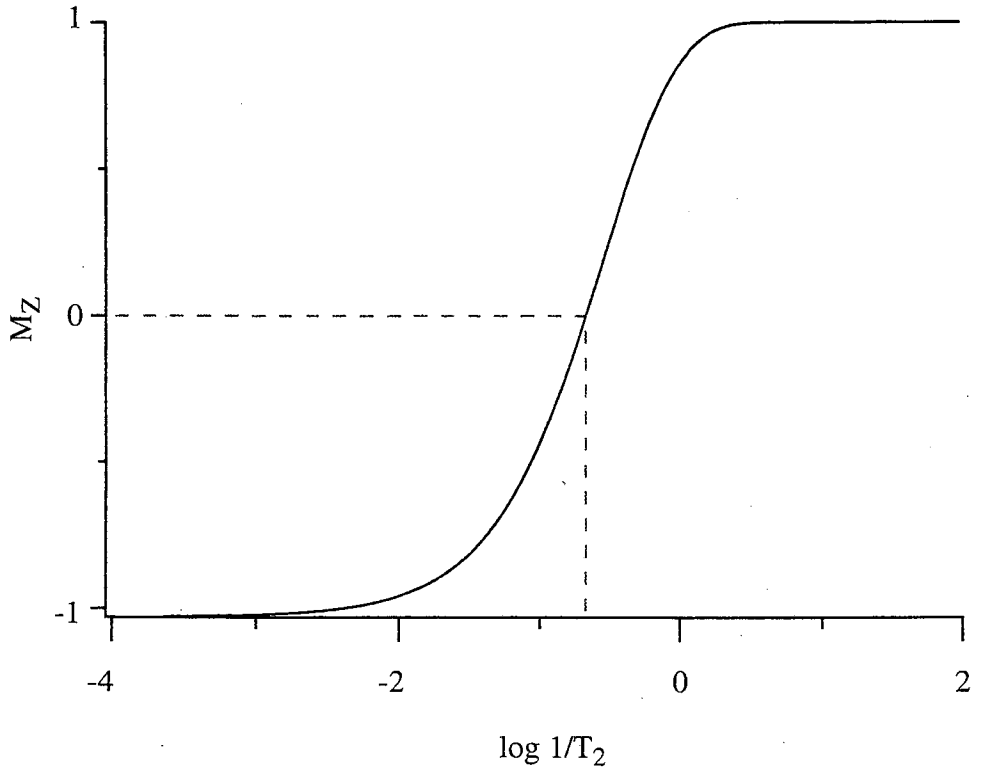

Figure 2.6 Theoretical plot of M_z as a function of T_2 following a third order dressing pulse designed to selectively null species with a T_2 of 4.5 msec.

msec. Of particular importance is the fact that a species with T_2 longer or shorter than 4.5 msec have a non-zero final M_Z. Thus this pulse acts as a "notch" filter in T_2.

2.3 Experimental

This section will outline some of the more utilitarian aspects of the creation of T_2-selective pulses. We will start by describing how to translate a theoretical pulse shape into an experimental tool. We will then delve into the dressing pulse's physical tolerances. Some attention will be paid towards choosing the ideal samples to highlight the selective properties of dressing pulses. Finally the hardware and pulse sequences used for collecting data in these experiments are described.

2.3.1 Dressing Pulses

Selective pulses were constructed as follows. A theoretical pulse backbone for nulling species with T_2 = 1 msec was produced. As can be seen in figure 2.7, the amplitude of the RF takes on both positive and negative real values.

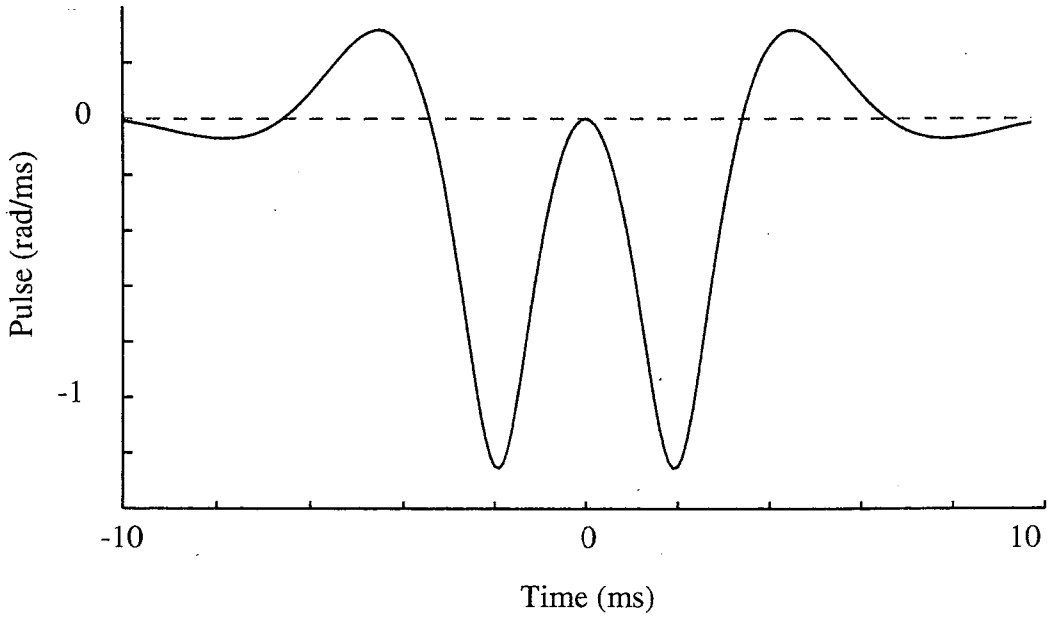

Figure 2.7 A plot of nutation frequency as a function of time for a 3rd order dressing pulse designed to selectively null the magnetization from species with a T_2 of 1 msec.

This backbone can serve as a template for nulling any species by adjusting the pulse length and the pulse power. To make these adjustments, the pulse backbone is broken into 800 steps of equal length with a normalized value between 0 to 1 indicative of the relative nutation frequency at that point in the pulse. This enables us to control the pulse length and the relative pulse power. Next, with a T_2 measurement, an estimate of the power and pulse length required to null the sample of choice was made. With these as starting conditions, the pulse length and power were iteratively adjusted to find the best null on the sample to be selectively removed. To illustrate this, figure 2.8 is a plot of the final M_Z, following a dressing pulse, as a function of pulse length for a sample with T_2=1.1 msec.

As a small digression, we should address how M_z is measured, and thus how a null is found. The integrated area of a spectral peak is proportional to the number of active spins, or M_z before a hard $\pi/2$ "read" pulse. Thus, experimentally M_z is measured by applying a hard "read" pulse to the sample, Fourier transforming the resultant free induction decay, and integrating the peak.

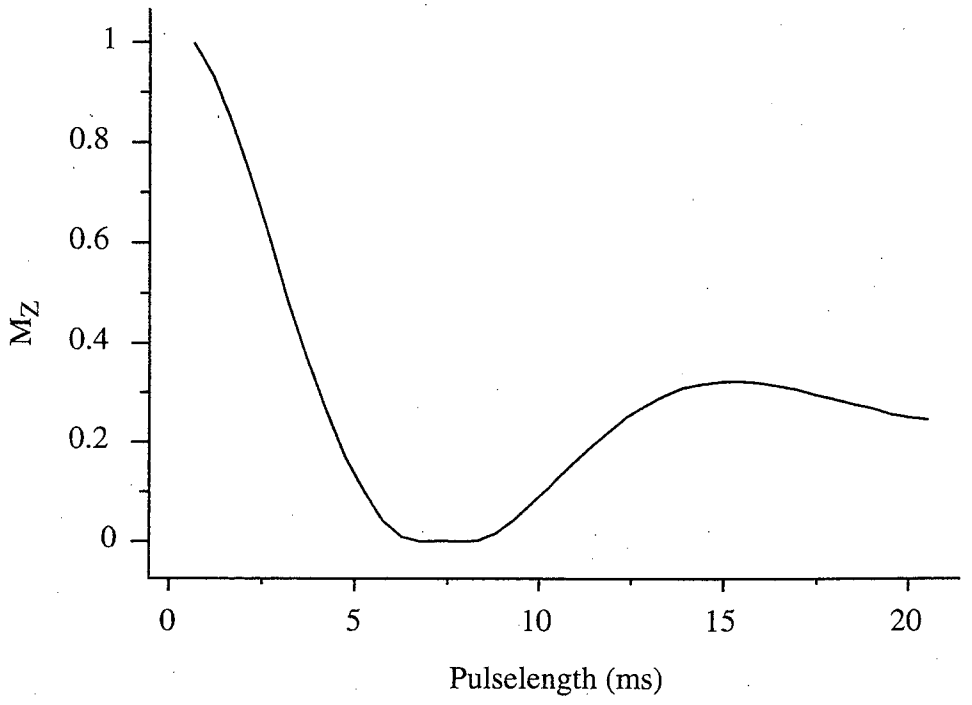

Figure 2.8 A plot of M_z as a function of dressing pulse length. The null for this sample occurs with a dressing pulse that is 6.9 msec long.

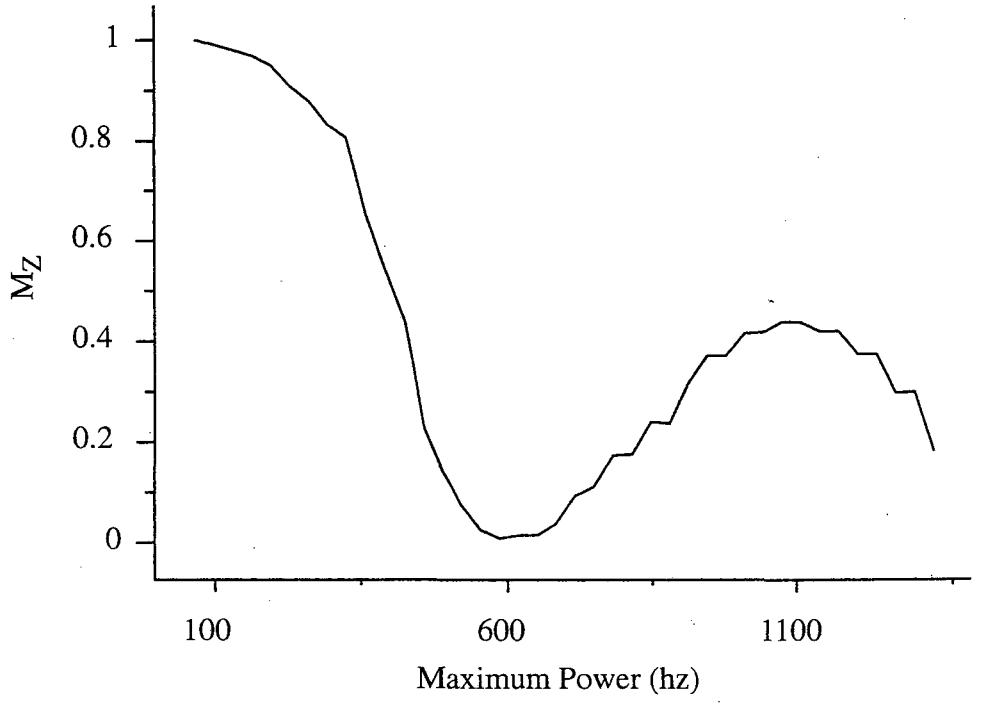

Figure 2.9 A plot of M_Z as a function of maximum dressing pulse nutation frequency. The null for this sample occurs with a dressing pulse that has a maximum nutation frequency of 600 Hz.

The first thing to note about figure 2.8 is M_Z=0 for an optimized dressing pulse, and thus the species is effectively nulled. One can also see that the nulling capability drops off dramatically as the pulse length is misadjusted. A similar plot, figure 2.9, can be made of the final M_Z, following a dressing pulse, as a function of pulse power. Again an optimal nutation frequency can be seen and as one deviates from this position, the nulling capability declines.

One of the assumptions made in designing these pulses is that any species to be nulled is on resonance, ω_{off}=0. The

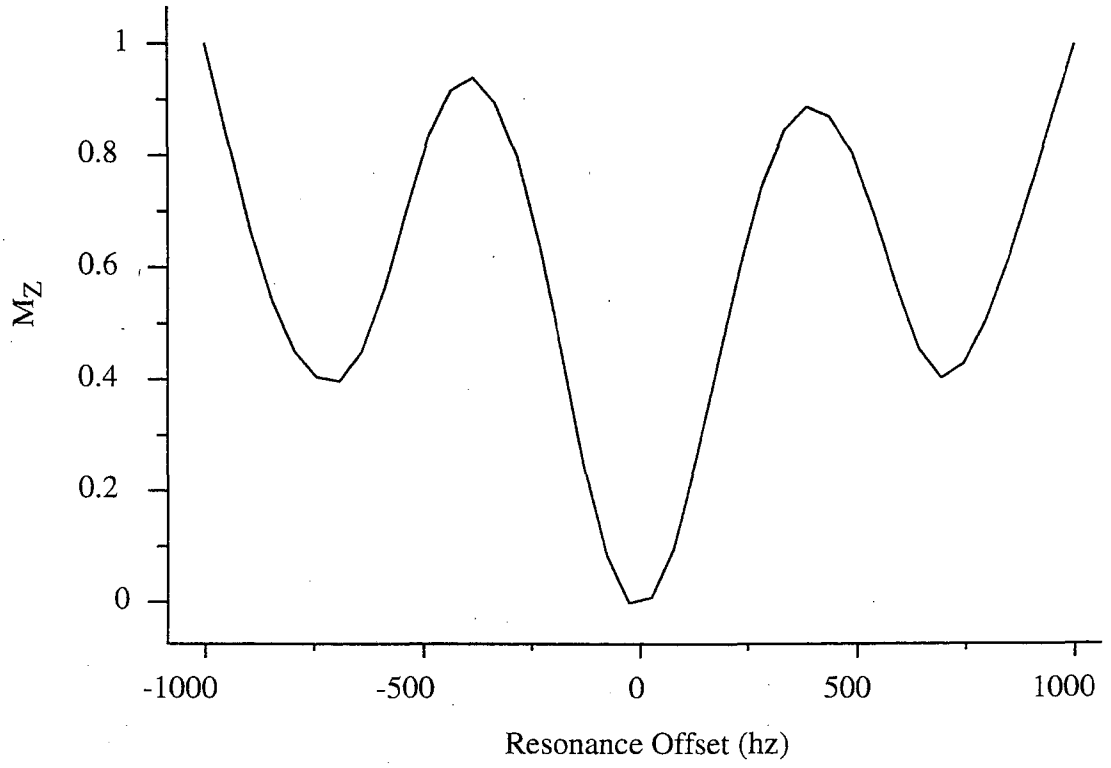

Figure 2.10 A plot of M_Z as a function of resonance offset, ω_{off}, for an optimized 3rd order dressing pulse. The bandwidth of the dressing pulse is approximately 250 Hz.

bandwidth of a real dressing pulse can be seen in figure 2.10. There we see a plot of the final M_Z, following an optimized dressing pulse, as a function of resonance offset. The pulse efficiency falls of sharply as we stray from resonance. The functional bandwidth is approximately ± 125 Hz. This of course is a mixed blessing. In terms of selectivity, it means that not only is the dressing pulse potentially T_2 selective, it is also resonance frequency selective. The advantages of this property are not exploited in this thesis. The disadvantage is that for fair comparisons between samples with different T_2 values, we must make sure that the resonance frequency of each sample

falls within a narrow range. This leads us directly to our next section, samples.

2.3.2 Samples

Choosing the "correct" sample, that will provide a clear explicative vehicle to the fundamental idea you wish to test out, can be a bit tricky. Our primary goal was to demonstrate the T_2-selectivity of the dressing pulses described above. The ideal system, would be a series of samples in which T_2 varies while all other attributes are held constant. In this case, other attributes include resonance offset, sample size, couplings, and T_1. Of these, we need to pay particular attention to the resonance frequency, as figure 2.10 shows that the dressing pulses excite a finite bandwidth.

Our first attempt to design such a system was a series of aqueous $CuSO_4$ solutions. It is well known that paramagnetic ions act as relaxation agents. Thus by varying the concentration of $CuSO_4$ we could impart unique relaxation dynamics to a series of nearly identical samples. This series, as will be shown later, was used to experimentally show the band pass nature of the dressing pulse. This system had two distinct drawbacks. . While Cu^{2+} is a good relaxation agent, it is also a good shift reagent. Thus each sample had a concentration-dependent resonance condition. This prohibited $CuSO_4$'s use in exhibiting the selective aspect of the dressing pulses. The second drawback, which we could correct for, was T_1 is also concentration dependent.

The system used for the selectivity studies was a pair of aqueous $MnCl_2$ (15 and 1.9 mmol) solutions. While T_1 still varied with concentration, Mn^{2+} was seen to be a rather poor shift reagent. Because of this, each sample had

nearly the same resonance conditions. With the incorporation of a sample holder comprised of two concentric tubes, figure 2.11, we were able to simultaneously observe two species with the same resonance condition, but with different T_2 values.

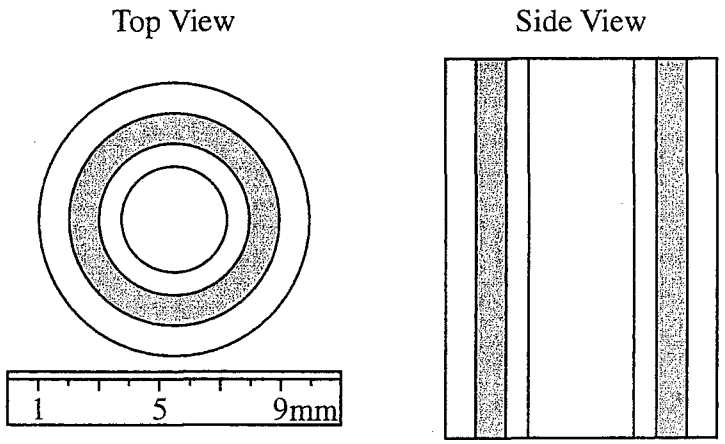

Figure 2.11 The sample phantom. It consisted of two concentric tubes: outer tube 7 mm inner diameter and 9 mm outer diameter, inner tube 3.5 mm inner diameter and 5 mm outer diameter.

T_2 relaxation times were estimated from the full width at half height of the water spectra, using,

$$T_2 = \frac{1}{\pi \cdot (FWHH)} \qquad (2.22)$$

and taking into account the 10 Hz broadening due to residual field inhomogeneity. They were 0.45 msec and 3.3 msec for the 15 and 1.9 mmol $MnCl_2$ solutions respectively. Thus producing an image of just one tube, in

the presence of the second, is the ideal model system to demonstrate T_2 selective pulses.

2.3.3 Hardware

Selectivity experiments were performed in a wide-bore Nalorac magnet (4.2 Tesla) using a home built imaging probe capable of producing linear magnetic field gradients (0.65 Tesla/Meter). These experiments used a Chemagnetics CMX Infinity spectrometer with computer controlled radio frequency (RF) power levels. In order to obtain the rather low nutation frequencies required for the dressing pulses (~1 rad/msec), a few modifications of the spectrometer had to be made. First, the amplifiers were removed and the preamplifier was used as the RF amplification source. Next, a secondary attenuation source capable of lowering the RF power by 100 dB, was added after the preamplifier. Finally, the peak voltage of many dressing pulses was far below 0.7 V. This meant that the crossed diodes in parallel, that are usually inline directly after the amplification stage to prevent signal from being reflected and lost in to the rf amplifier, had to be removed.

Experiments to show the band pass nature of the dressing pulses were performed in a wide-bore magnet (9.4 Tesla) using a commercial two channel (HX) liquid probe. These experiments were also performed with a Chemagnetics CMX Infinity spectrometer as modified above.

2.3.4 Sequences

The pulse sequence, used to obtain one dimensional selectivity data and bandpass data, is a dressing pulse, which parameterizes the initial M_Z magnetization as a function of T_2, followed by a hard "read" pulse, which measures the resultant M_Z magnetization. This is depicted in figure 2.12.

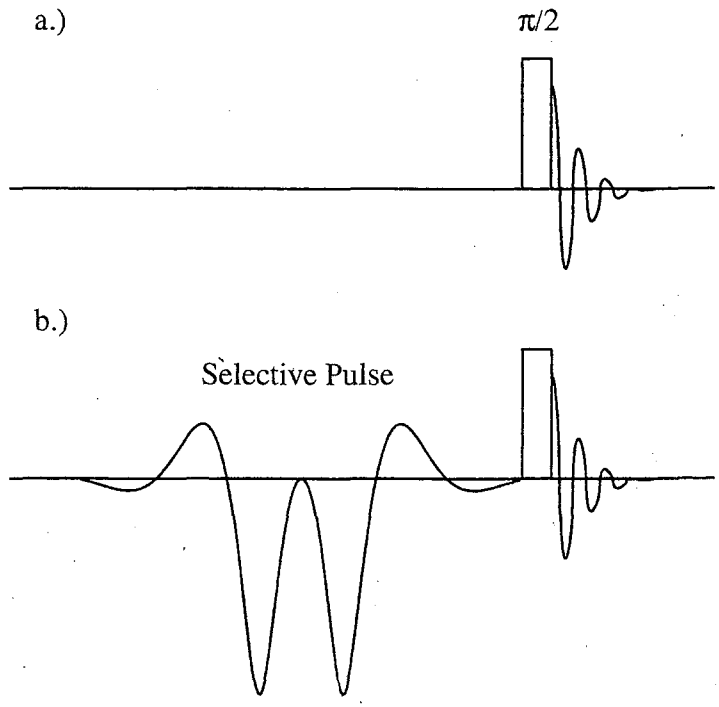

Figure 2.12 The basic pulse sequences used to measure M_Z. a.) is a normal $\pi/2$-detect experiment, used to measure "un-dressed" magnetization. b.) includes a dressing pulse which parameterizes M_Z as a function of T_2.

The spin-warp imaging pulse sequence[17], used to acquire a "normal" two-dimensional map of spin density, is shown in figure 2.13a. The addition of a

relaxation selective preparatory pulse, figure 2.13b, allows one to acquire a relaxation selective map of spin density.

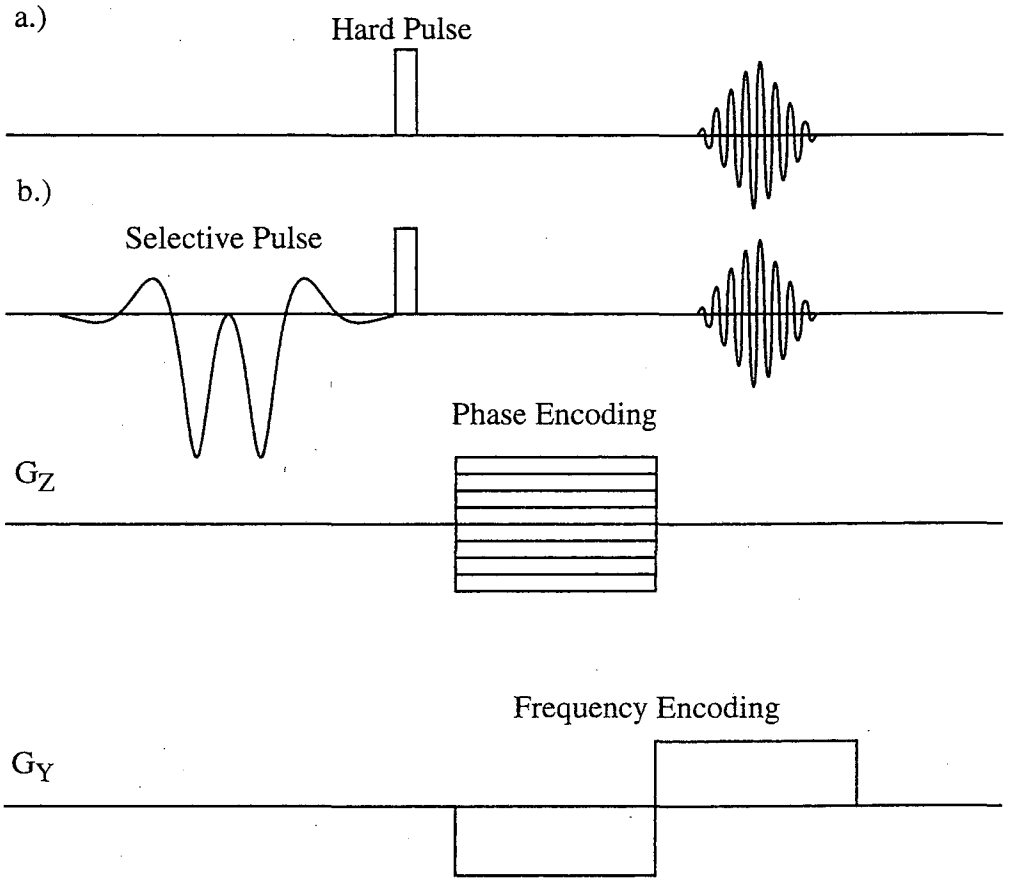

Figure 2.13 Two-dimensional imaging pulse sequences. The basic imaging sequence was adapted from spin-warp imaging [17]. a.) The sequence used to acquire a normal map of the total spin density, b.) The sequence that incorporates a preparatory 3rd order dressing pulse to selectively null the magnetization of a given T_2 species.

2.4 Results

This section will detail the results of three experiments. First it will report on the bandpass experiment, which experimentally supports our theory and shows that dressing pulses are able to create a final magnetization that is parameterized as a function of T_2. Next we will present one-dimensional studies, which highlight the selective nature of the dressing pulses. Finally this selectivity is used as the preparatory stage to create relaxation-selective two-dimensional images.

2.4.1 Bandpass Experiment

The bandpass nature of the 3rd order dressing pulse, as described above, was tested experimentally with the $CuSO_4$ series. First a species with a midrange value of T_2=4.5 msec, was chosen as the species to null. The dressing pulse length and RF intensity were then iteratively adjusted to find an optimal null for this sample. The optimal pulse length was found to be 14.5 msec. M_Z, following this optimized pulse, was then measured for each sample in the $CuSO_4$ series. This was accomplished in a three step process. First a $\pi/2$-detect experiment was run. This allowed us to set the carrier on resonance. As noted above, the integrated area of a spectral peak is proportional to M_Z before a hard "read" pulse. Thus a second $\pi/2$-detect experiment was run and the integrated area of the Fourier-transformed signal was used to measure the "un-dressed" M_Z of the sample. Essentially this was a normalization run. The final step was to use the optimized dressing pulse to parameterize M_Z as a function of T_2 and use a $\pi/2$–pulse to then measure

the resultant M_Z, as shown in figure 2.12. T_1 for these samples was not negligible and was approximately three times longer than T_2. The solid line in Fig 2.14 shows the numerically calculated response for the optimized dressing pulse, as given by equation 2.21 and shown in Fig 2.6, with $T_1=3T_2$ included in the calculation. This curve compares very well with the experimental results, shown as crosses. These results are published in [11] and served as the impetus to begin the selective experiments below.

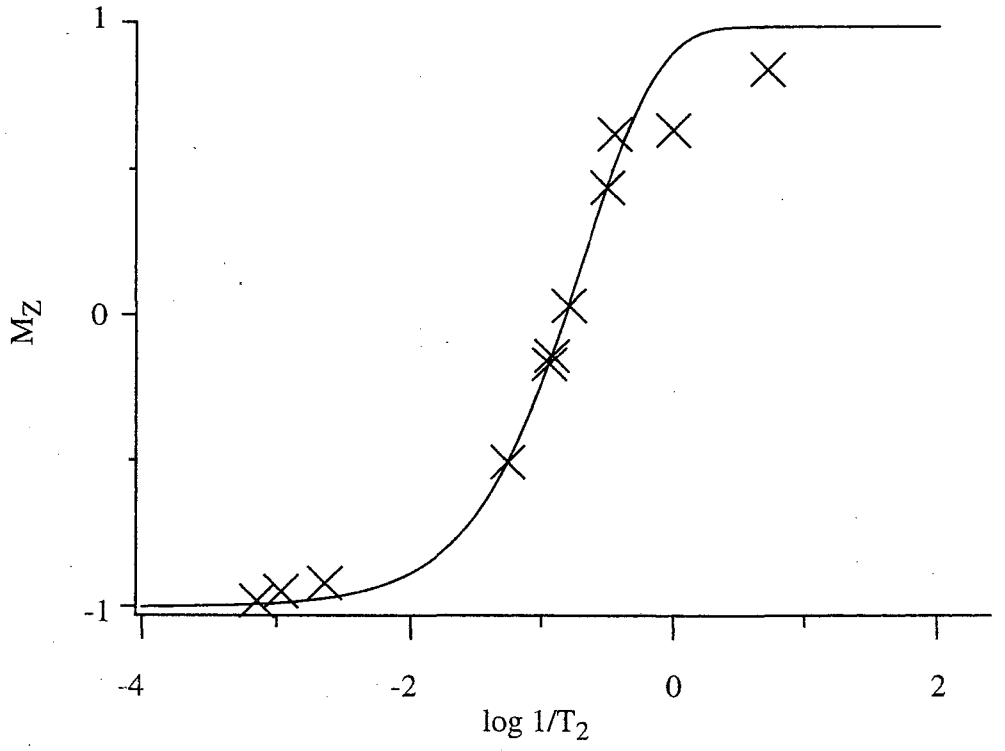

Figure 2.14 The solid line is a theoretical plot of M_Z as a function of T_2, following a third order dressing pulse designed to selectively null species with a T_2 of 4.5 msec. Crosses represent experimental measurements of M_Z following the above dressing pulse, for a series of samples with different T_2 values.

2.4.2 One-dimensional Selectivity

The results of the one-dimensional selective experiments are shown in figure 2.15. The sample, as described above, consisted of two concentric cylinders, with the long T_2 species (1.9 mmol $MnCl_2$) in the outer tube and the short T_2 species (15 mmol $MnCl_2$) in the inner tube. The optimized dressing pulse for nulling the species with a T_2 of 0.45 msec was 3.31 msec long and had a peak power of 1.18 Watts. The optimized dressing pulse for nulling the species with a T_2 of 3.283 msec was 24.5 msec long and had a peak power of 12.5 mWatts.

Figure 2.15a shows the spectra following a hard pulse. This spectrum indicates that both species have nearly the same resonance frequency. This near equality ensures that this is an ideal test sample. Upon expansion, the line shape shows a broad base, indicative of the fast relaxing sample in the inner tube, and a sharp central peak, indicative of the slow relaxing sample in the outer tube. The pulse sequence used to acquire relaxation selective data is shown in figure 2.12. Figure 2.15b shows the spectrum obtained following a 3rd order dressing pulse designed to selectively null the magnetization of the fast relaxing species. Figure 2.15c shows the spectrum obtained following a 3rd order dressing pulse designed to selectively null the magnetization of the slow relaxing species.

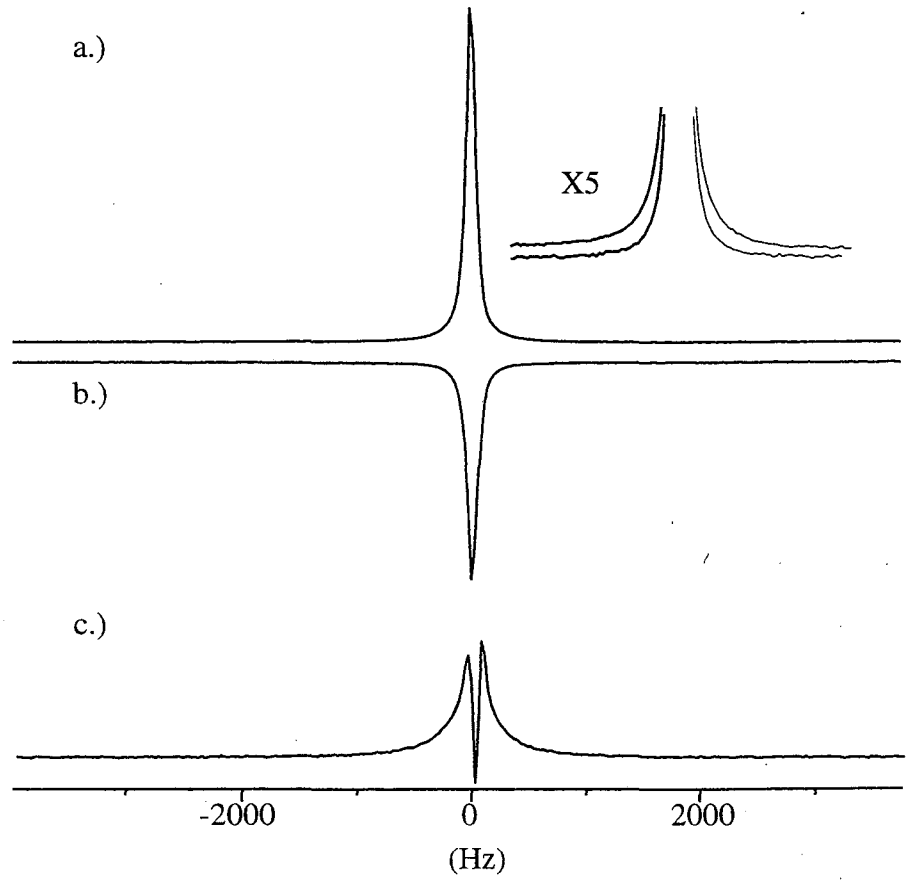

Figure 2.15 One-dimensional spectra taken at 4.2 Tesla. The inner tube contained a 15 mmol $MnCl_2$ solution and the outer tube contained a 1.9 mmol $MnCl_2$ solution. a.) The spectrum resulting from both tubes, following a hard pulse. Note the resonance condition for each tube is nearly identical. b.) The spectrum resulting from both tubes following a 3rd order dressing pulse (3.31 ms), designed to selectively null the species in the inner tube with a T_2 of 0.45 msec and a hard read pulse. c.) The spectrum resulting from both tubes following a 3rd order dressing pulse (24.5 ms), designed to selectively null the species in the outer tube with a T_2 of 3.3 msec and a hard read pulse.

The integrated area of 2.15a should result from the sum of the active spins in the inner tube and the outer tube. Following this example, the integrated area of 2.15b should represent the sum of the active spins in the inner tube (zero, following the dressing pulse) and the active spins in the outer tube (non-zero and scaled, following the dressing pulse). As such, the integrated area of the spectrum of 2.15b (i=-0.49) should be equivalent to the integrated area of just the slow relaxing species in the outer tube scaled by the application of a dressing pulse optimized to null the fast relaxing species. Similarly, the integrated area of the spectrum of 2.15c (i=0.28) should be equivalent to the integrated area of just the fast relaxing species in the inner tube scaled by the application of a dressing pulse optimized to null the slow relaxing species. Using the above argument one can calculate the theoretically expected integrated area values for 2.15b and 2.15c using equation 2.21. Theoretically, 2.15c should have an integrated area i= -0.50 and 2.15c should have an integrated area i=0.26. Experiment and theory match very well and offer direct evidence of the pulse's ability to selectively null the magnetization of one species in the presence of a second.

The narrow line shape of 2.15b is further qualitative evidence that the fast relaxing species, which would have resulted in a broadened base, has been removed. Further, the broad lineshape of 2.15c is also qualitative evidence that the slow relaxing species, which would have resulted in a narrow line, has been removed. At this point, we attribute the sharp negative feature in the center of 2.15c to the spatial distribution of the water in the sample.

2.4.3 T_2-Selective Imaging

The results of the two dimensional experiments are shown in figure 2.16. Using the imaging pulse sequence described in figure 2.13a, a "normal" map of the spin density as a function of position for the concentric tube sample holder, figure 2.11, was obtained (figures 2.16a and d). Figure 2.16a is a one dimensional slice taken from the center of the sample. Note that there is appreciable spin density in both the outer and inner tubes, signifying signal from both the fast and slow relaxing species. However, because an echo is being detected, the relative intensity of the inner and outer tube is scaled by T_2. This explains why in a "normal" image, the outer tube has higher intensity than the inner tube. T_2-selective images, figure 2.16b, c, e, and f, were recorded using the pulse sequence described in figure 2.13b with appropriate 3rd order dressing preparatory pulses. In the one dimensional slice depicted in 2.16b one can see that the signal from the inner spin density was successfully nulled and an image of just the outer tube was created. Conversely, in 2.16c the outer spin density was nulled and an image of just the inner tube was created. Figures 2.16 d-f are the corresponding two dimensional images. Figure 2.16d shows the full "normal" two dimensional image while 2.16e and f are relaxation selective images. Each is plotted on the same scale, with the same maximum and minimum cutoffs. From these images it is clear that the relaxation selective preparatory pulses were successful and the first T_2-*selective* images were acquired.

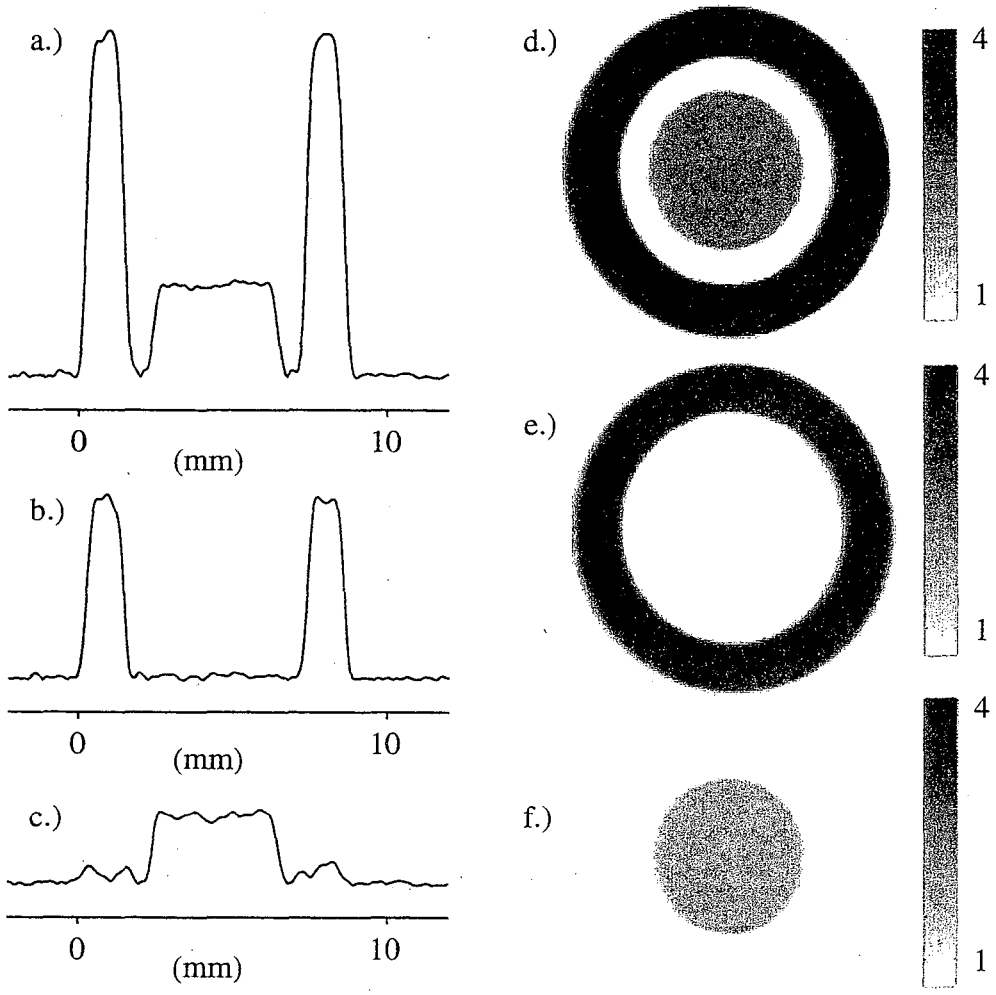

Figure 2.16 Two dimensional images taken at 4.2 Tesla. With the sample cell described in figure 2.11, the inner tube contained a 15 mmol $MnCl_2$ solution and the outer tube contained a 1.9 mmol $MnCl_2$ solution. a.), b.), and c.) are one dimensional slices through the centers of images d.), e.), and f.) respectively. All raw data sets for these images were taken under identical conditions with 128 phase encoding steps with 128 time domain points. During processing, free induction decays were zero filled to 256 by 256 points, apodized with a Gaussian, and then Fourier transformed in both dimensions. a.) and d.) The "normal" image of ^1H spin density. b.) and e.) The image acquired using a

preparatory dressing pulse (24.5 ms, 12.5 mWatts maximum power) designed to selectively null the outer species with a T_2 of 3.3 msec. c.) and f.) The image acquired using a preparatory dressing pulse (3.31 ms, 1.18 Watt maximum power) designed to selectively null the inner species with a T_2 of 0.45 msec .

2.5 Conclusions

Relaxation selective pulses have the potential to be extremely useful in both MRI and NMR spectroscopy. Described above is an application of this powerful new tool to create contrast in magnetic resonance images. Without impinging upon the non-invasive aspects of the basic MRI experiment, one is able to create a selective map of spin-density based on the intrinsic dynamics of the system of interest. This is of particular importance in selective *in vivo* imaging of damaged tissue as it has long been known that many pathologies give rise to areas of biomatter with distinct relaxation dynamics.

REFERENCES

1. F. W. Wehrli, *Progress in Nuclear Magnetic Resonance Spectroscopy*, **28**, 87-135 (1995).

2. W. S. Price, *Annual Reports on NMR Spectroscopy*, **35**, 139-216 (1998).

3. Y. Xia, *Concepts in Magnetic Resonance*, **8**, 205-225 (1996).

4. R. C. Brasch, *Radiology*, **147**, 781-788 (1983).

5. P. C. Lauderbur, *Philosophical Transactions. Royal Society of London B*, **289**, 483 (1980).

6. M. D. Ogan and R. C. Brasch, *Annual Reports in Medicinal Chemistry*, **20**, 277-286 (1985)

7. A. Bifone, Y. -Q. Song, R. Seydoux, R. E. Taylor, B. M. Goodson, T. Pietraß T. F. Budinger, B. Navon, and A. Pines, *Proceedings of the National Academy USA*, **93**, 12932-12936 (1996).

8. M. J. Lizak and M. S. Conradi, *Journal of Magnetic Resonance*, **95**, 548-(1991)

9. L.E. Crooks, C.M. Mills, P. L. Davis, M. Brant-Zawadski and J. Hoenniger, *Radiology*, **144** 843 (1981).

10. N. K. Andreev, A. M. Khakimov and D. I. Idiyatullin, *Instruments and Experimental Techniques*, **41**, 251-256 (1998).

11. D. E. Rourke and S. D. Bush, *Physical Review E*, **57**, 7216-7230 (1998).

12. P. J. Caudrey, *Physica D*, 6, 51 (1982).

13. V. E. Zakharov and A. B. Shabat, *Funct. Anal. Appl*, **13**, 166 (1980).

14 M. J. Ablowitz, B. J. Kaup, A. C. Newell, and H. Segur, *Stud. Appl. Math.*, **53**, 249 (1974).

15 M. J. Ablowitz, *Stud. Appl. Math.*, **58**, 17 (1978).

16 R. K. Dodd, J. C. Eilbeck, J. D. Gibbon, and H. C. Morris, *Solitons and Nonlinear Wave Equations*, (Academic Press, London, 1988), Chap. 6.

17. W. A. Edelstein, J. M. S. Hutchinson, B. Johnson and T. Redpath, *Physics and Medicine in Biology*, **25**, 751 (1980).

CHAPTER 3

HARNESSING RADIATION DAMPING

3.1 Introduction

Nuclear magnetic resonance is an inherently insensitive spectral technique. This limitation arises because at room temperature there is sufficient thermal energy to populate both the lower and upper Zeeman spin states. The sensitivity of the NMR experiment is proportional to this population difference, or polarization, which typically is on the order of parts per million. Thus in a sample of 10^{23} spins only 10^{17} spins contribute to the signal in an experiment.

A tremendous amount of effort has been directed towards pushing the boundaries of sensitivity in NMR. Increasing the external magnetic field strength is a direct means of attacking this problem. As we saw in section 1.2.1, the Zeeman energy difference is proportional to the strength of the external

magnetic field. Thus by moving to higher fields one can create a larger polarization and in turn increase the overall experimental sensitivity.

With these advances, come new, and often troublesome, challenges. Radiation damping, the central topic of this chapter, is one such effect. NMR signals are detected as an induced current in a tuned LCR circuit. Following excitation, this current is generated as the sample spins presses coherently in the x-y plane. The initial Zeeman spin polarization dictates the magnitude of this signal current and hence the overall sensitivity of the NMR experiment. Radiation damping describes the effect that the current induced by the sample has on the sample itself. To the sample, the signal current generates a highly non-linear low power RF "reaction" field, which drives the system back to equilibrium. Thus, as experiments utilize higher magnetic fields, radiation damping becomes more pronounced.

Primarily seen as a nuisance in high-resolution liquid state NMR, the nonlinear distortions of the free induction decay (FID) lead to a broadening of spectral features. This can be seen in figure 3.1 where FIDs are shown for a idealize single resonance sample with and without radiation damping. In a.) we see a long lived, FID that is only damped by T_2. Upon Fourier transformation this leads to a narrow spectral feature with high resolution. Conversely, in b.) we see the damped FID decays quickly. Upon Fourier transformation this leads to a broad spectral feature with lower resolution.

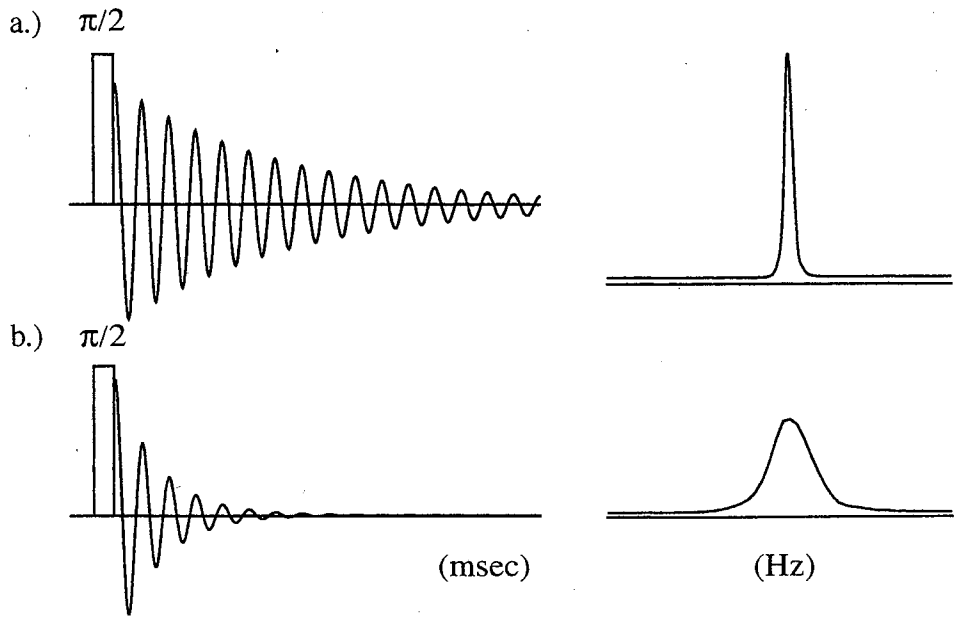

Figure 3.1 The effect of a radiation damping reaction field. a.) shows a long lived free induction decay following a $\pi/2$ pulse and the subsequent narrow Fourier transform. b.) depicts a damped, short lived free induction decay and its broadened fourier transform.

Most work on radiation damping has focused on its removal. One such approach utilizes a feedback scheme to directly "correct" the effect of radiation damping [1]. Measuring the current induced in the coil between points they create a compensation field which is used to negate the radiation damping reaction field. A second strategy reduces the effect of radiation damping by lowering the bulk magnetization of the sample. This is achieved by utilizing perdeuterated solvents such as D_2O.

While these approaches offer a stop-gap mechanism for of dealing with radiation damping, they do not address the central question of understanding its nonlinear effects. This chapter will present recent work that addresses the rich

physics of radiation damping. It will begin with a theoretical outline of radiation damping in an inhomogenous magnetic field. Following a brief description of our experimental set up; attention will be directed towards a series of experiments that seek to capitalize on the sensitivity of radiation damping. There, we will not only outline an experiment which removes the effect of radiation damping, we will describe a family of experiments which seek to exploit the non-linear nature of radiation damping as a potential super sensitive indirect detector of dilute spins.

3.2 Theory

This section will detail the theoretical treatment of radiation damping in an inhomogeneous magnetic field used in this chapter. Our discussion will focus on a symmetric distribution of magnetic isochromats described by g(δ) where δ=0 on resonance. For our purposes we will take g(δ) to be a normalized symmetric Lorentzian distribution

$$g(\delta) = \frac{T_2^*}{\pi}(1 + \delta^2 T_2^{*2})^{-1} \quad (3.1)$$

Here, T_2^* describes the dephasing of x-y in an inhomogeneous field.

As motivated earlier, coherent magnetization oscillating in the x-y plane induces a current in a tuned LCR circuit. This current in turn creates a reaction field, on the order of 100 Hz. In the absence of field inhomogeneity, this non-linear reaction field will drive the magnetization back to the z-axis. The problem becomes more complicated when one incorporates the effect of an

inhomogeneous magnetic field. As the x-y magnetization dephases with T_2^*, the induced current responsible for the radiation damping reaction field decreases. Thus, there is a dynamic interplay between T_2^* and the reaction field. Instead of driving the central magnetization vector of g(δ) distribution all the way back to z-axis, the reaction field is only able to drive the magnetization an angle Δθ. This is depicted in figure 3.2 for the central vector of the distribution g(δ) at δ=0.

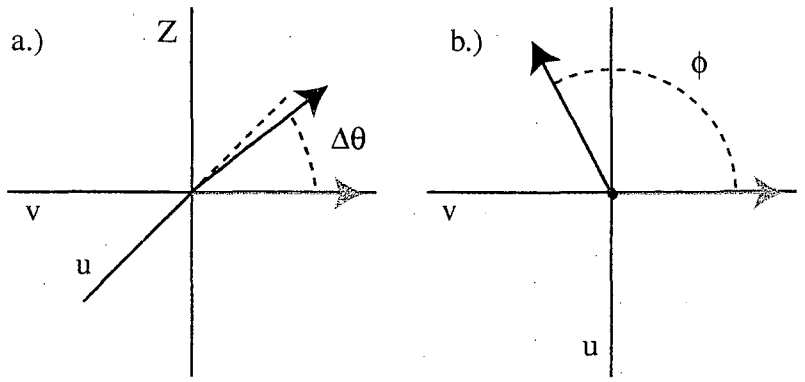

Figure 3.2 Evolution of central magnetization vector due to radiation damping reaction field in following a π/2 pulse. a.) describes the angle Δθ, the degree to which the magnetization vector is pushed back towards the +z-axis. In b.) the phase angle ϕ that central vector accumulates in the u-v plane if it is part of an asymmetric distribution.

There we see that following a π/2 y pulse the central magnetization vector lies along the x-axis (gray vector). The reaction field then pushes the central vector away from the x-axis by an angle Δθ (black vector). If viewed along the z-axis, b.), we see can see that reaction field may also impart a phase ϕ. The primary

goal of this section will be to develop a means of determining this angle $\Delta\theta$ and phase ϕ.

Our theoretical treatment of $\Delta\theta$ and ϕ will follow the model presented by Augustine and Hahn[2,3,4]. We will start by relating the current I(t), which induces the reaction field, and the laboratory frame magnetization, $M_x(t)$ in an LCR circuit,

$$L\frac{d^2}{dt^2}I(t)+R\frac{d}{dt}I(t)+\frac{1}{C}I(t)=-4\pi\xi\eta A\frac{d^2}{dt^2}M_X(t). \tag{3.2}$$

Here L is the inductance, R is the resistance and C is the capacitance in a tuned LCR circuit. The resonant coil is described by η, the number of ampere turns, A, the cross-sectional area, and ξ the filling factor. I(t) can be expressed as,

$$I(t)=\sqrt{\frac{V_C}{\pi L}}H_1(t)\cos(\omega t+\phi), \tag{3.3}$$

where V_C is the coil volume and $H_1(t)$ is the time dependent reaction field. We can then express $M_X(t)$ as,

$$M(t)=u(\delta,t)\cos(\omega t)+v(\delta,t)\sin(\omega t). \tag{3.4}$$

Here, $u(\delta,t)$ and $v(\delta,t)$ are the in-phase and out-of-phase magnetization components of $g(\delta)$ respectively. Where $g(\delta)$, as stated above, describes a symmetric Lorentzian distribution of isochromats. Our next task is to expand equation 3.2 by inserting our definitions of M(t) and I(t). To do this we will need the following derivatives,

$$\frac{\dot{I}(t)}{\omega^2} = \sqrt{\frac{V_C}{\pi L}}\left[\frac{\dot{H}_1}{\omega^2}\cos(\omega t+\phi) - \frac{H_1}{\omega}\sin(\omega t+\phi)\right], \tag{3.5}$$

$$\frac{\ddot{I}(t)}{\omega^2} = \sqrt{\frac{V_C}{\pi L}}\left[\frac{\ddot{H}_1}{\omega^2}\cos(\omega t+\phi) - \frac{2\dot{H}_1}{\omega}\sin(\omega t+\phi) - H_1\cos(\omega t+\phi)\right], \tag{3.6}$$

$$\begin{aligned}\frac{\ddot{M}(t)}{\omega^2} = &\left[\frac{1}{\omega^2}\ddot{u}(\delta,t) - u(\delta,t) + \frac{2}{\omega}\dot{v}(\delta,t)\right]\cos(\omega t) - \\ &\left[\frac{1}{\omega^2}\ddot{v}(\delta,t) + v(\delta,t) - \frac{2}{\omega}\dot{u}(\delta,t)\right]\sin(\omega t)\end{aligned} \tag{3.7}$$

We can simplify these equations by making the slowly varying modulus approximation and keeping only the largest terms. In equations 3.5 and 3.6 we note that terms proportional to ω^{-2} are small and can be dropped leaving,

$$\frac{\dot{I}(t)}{\omega^2} = -\sqrt{\frac{V_C}{\pi L}}\frac{H_1}{\omega}\sin(\omega t+\phi), \tag{3.8}$$

$$\frac{\ddot{I}(t)}{\omega^2} = \sqrt{\frac{V_C}{\pi L}}\left[-\frac{2\dot{H}_1}{\omega}\sin(\omega t+\phi) - H_1\cos(\omega t+\phi)\right]. \tag{3.9}$$

Equation 3.7 is simplified when we make the approximation $u, v >> \ddot{u}/\omega^2, \ddot{v}/\omega^2$ and $\dot{u}/\omega, \dot{v}/\omega$,

$$\frac{\ddot{M}(t)}{\omega^2} = -u(\delta,t)\cos(\omega t) - v(\delta,t)\sin(\omega t). \tag{3.10}$$

Plugging equations 3.3 (divided by ω^2), 3.8, 3.9, and 3.10 into equation 3.2 we get,

$$\begin{aligned}\sqrt{\frac{V_C}{\pi L}}\left[\left(-\frac{2L\dot{H}_1}{\omega} - \frac{RH_1}{\omega}\right)\sin(\omega t+\phi) + \left(\frac{1}{\omega^2 C}H_1(t) - LH_1\right)\cos(\omega t+\phi)\right] = \\ 4\pi\xi\eta A\left[-u(\delta,t)\cos(\omega t) - v(\delta,t)\sin(\omega t)\right]\end{aligned} \tag{3.11}$$

Equation 3.11 in turn simplifies when we note that on resonance, $\omega=1/(LC)^{1/2}$,

$$\sqrt{\frac{V_C}{\pi L}}\left[\left(-\frac{2L\dot{H}_1}{\omega}-\frac{RH_1}{\omega}\right)\sin(\omega t+\phi)\right]=4\pi\xi\eta A\left[-u(\delta,t)\cos(\omega t)-v(\delta,t)\sin(\omega t)\right]. \tag{3.12}$$

At this point we will introduce,

$$\dot{\theta}=\gamma H_1(t), \tag{3.13}$$

$$\ddot{\theta}=\gamma\dot{H}_1(t), \tag{3.14}$$

and multiply both sides of equation 3.12 by $(\omega\gamma/L)(\pi L/V_C)^{-1/2}$. After expanding the $\sin(\omega t+\phi)$ as $\sin(\omega t)\cos(\phi)+\cos(\omega t)\sin(\phi)$ and inserting the relation,

$$\frac{R}{L}=\frac{\omega}{Q}. \tag{3.15}$$

equation 3.12 can be written as,

$$\left[\left(\ddot{\theta}+\frac{\dot{\theta}\omega}{2\pi}\right)\cos\phi+\pi\xi\gamma\omega v(\delta,t)\right]\sin(\omega t)+\left[\left(\ddot{\theta}+\frac{\dot{\theta}\omega}{2\pi}\right)\sin\phi+\pi\xi\gamma\omega u(\delta,t)\right]\cos(\omega t)=0. \tag{3.16}$$

The only way equation 3.16 can be zero for all values of ωt is if both the $\sin(\omega t)$ and $\cos(\omega t)$ terms are zero. After multiplying through by $2Q/\omega$, this leads to,

$$\left(\frac{2Q\ddot{\theta}}{\omega}+\dot{\theta}\right)\cos\phi=-2\pi\xi\gamma Qv(\delta,t), \tag{3.17a}$$

$$\left(\frac{2Q\ddot{\theta}}{\omega}+\dot{\theta}\right)\sin\phi=-2\pi\xi\gamma Qu(\delta,t). \tag{3.17b}$$

We simplify 3.17a and b by noting that $2Q\ddot{\theta}/\omega << \dot{\theta}$ and by introducing the radiation damping constant $T_R = 2\pi\xi\gamma QM_0$. With these modifications we are left with,

$$\dot{\theta}\sin\phi=-\frac{1}{T_RM_0}u(\delta,t), \tag{3.18a}$$

$$\dot{\theta}\cos\phi=-\frac{1}{T_RM_0}v(\delta,t). \tag{3.18b}$$

At this point we can take the distribution of isochromats into account and integrate equations 14a and b over g(δ). For a symmetric distribution ϕ= 0 and we are left with a contribution only from v(δ,t) as,

$$\dot{\theta}=-\frac{1}{T_RM_0}\int v(\delta,t)g(\delta)d\delta. \tag{3.19}$$

In the absence of relaxation, we can then write a set of Bloch equations for M_Z, v(δ,t) and u(δ,t), as

$$\frac{d}{dt}M_Z=-\dot{\theta}v(\delta,t), \tag{3.20}$$

$$\frac{d}{dt}v(\delta,t)=\dot{\theta}M_Z(\delta,t)-\delta u(\delta,t), \tag{3.21}$$

$$\frac{d}{dt}u(\delta,t)=\delta v(\delta,t). \tag{3.22}$$

Integrating equation 3.19 with respect to time will then give us Δθ,

$$\int_0^\infty \dot{\theta} dt' = \theta_\infty - \theta_0 = \Delta\theta = -\frac{1}{T_R M_0}\int_0^\infty dt' \int v(\delta,t')g(\delta)d\delta \,. \tag{3.23}$$

Augustine and Hahn have shown[3,4] that equation 3.23 can be simplified by incorporating a manipulation used to explain self-induced transparency [5]. Here they took note of the relationship between $d/u(\delta,t)dt$ and $\delta v(\delta,t)$ described in equation 3.22 to solve the time integral on the right hand side of equation 3.23,

$$\Delta\theta = -\frac{1}{T_R M_0}\int d\delta \int_0^\infty \frac{\dot{u}(\delta,t')}{\delta} g(\delta)dt' = -\frac{1}{T_R M_0}\int \frac{u(\delta,t=\infty)-u(\delta,t=0)}{\delta} g(\delta)d\delta \,. \tag{3.24}$$

Upon integration over δ, leaves us with a simple transcendental expression for the magnitude of Δθ,

$$|\Delta\theta| = -\frac{T_2^*}{T_R}\sin\left(\theta - |\Delta\theta|\right), \tag{3.25}$$

where θ is the initial tip angle between of the isochromatic central vector M(0,0) att=0 chosen to lie between 0 and π. The interplay between T_2^* and the radiation damping time constant T_R now becomes clear. In a homogenous field, where T_2^* is long, Δθ is large, conversely in an inhomogenous field, T_2^* is short and Δθ is small.

Solutions to transcendental equations can be calculated graphically. To accomplish this one plots both the left and right hand sides of the equation on a similar axis as a function of the dependent variable. Where the plots intersect are solutions to the transcendental equation. In our case one plots $y_1 = |\Delta\theta|$ and

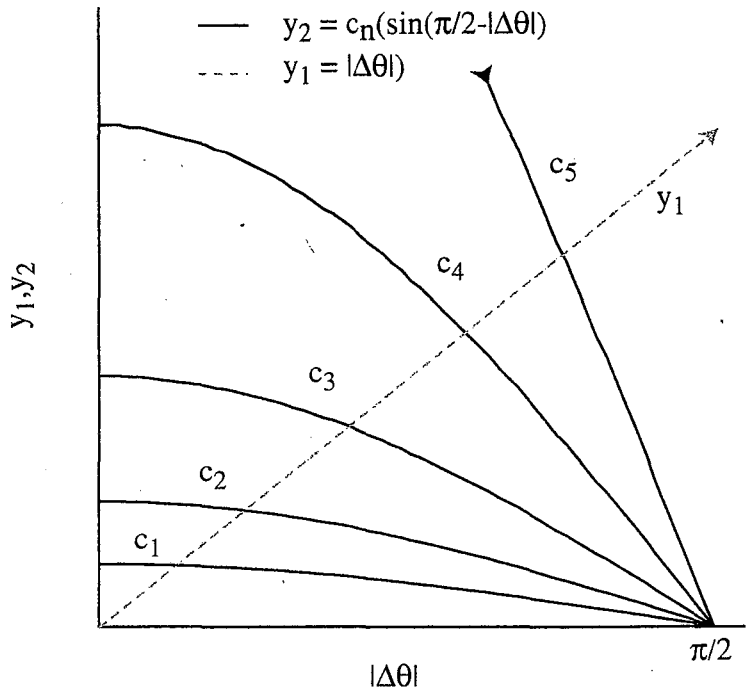

Figure 3.3 Graphical solutions to equation 3.25 for an initial θ pulse of $\pi/2$. Depicted are five evenly spaced values of c_n where $c_{n+1}=2c_n$.

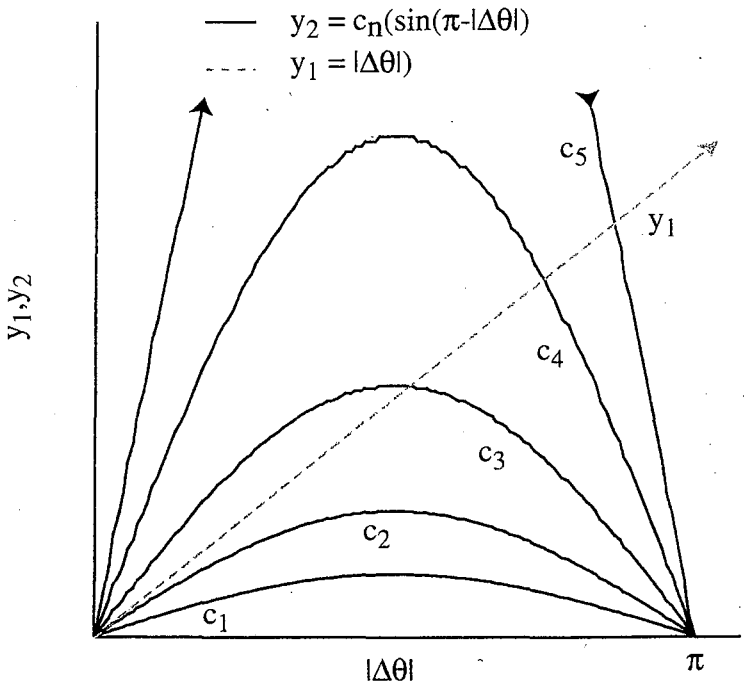

Figure 3.4 Graphical solutions to equation 3.25 for an initial θ pulse of π. Depicted are five evenly spaced values of c_n where $c_{n+1}=2c_n$. Nonzero solutions exist for c_3-c_5.

$y_2=c_n(\sin(\theta - |\Delta\theta|)$ against $|\Delta\theta|$. With $c_n = T_2^*/T_R$. This type of graphical solution can be seen in figures 3.3 and 3.4.

In figure 3.3 we see the result of an initial tip angle of $\pi/2$. To model changing experimental circumstances (varying external magnetic field strength or homogeniety) we have included a number of different values of c_n. As predicted, when c_n is large, ie a very homogenous field, $|\Delta\theta|$ is large.

Perhaps more interesting, in figure 3.4 our initial tip angle is π. Here we see that as we vary c_n we change the number of potential solutions. For values of $c_n < 1$ there are no non-zero solutions and the system does not experience the effects of radiation damping. However, when $c_n \geq 1$ we predict two solutions to equation 3.25. In this case, after the application of a π pulse, a small transverse component (v) can seed the start of the radiation damping reaction field causing the system to jump from the zero solution to the non-zero solution. Once seeded, the system thus behaves like a maser coherently driving the magnetization to its final position described by $|\Delta\theta|$. This results in a "burst" of signal as the magnetization swings through the x-y plane as depicted in figure 3.5.

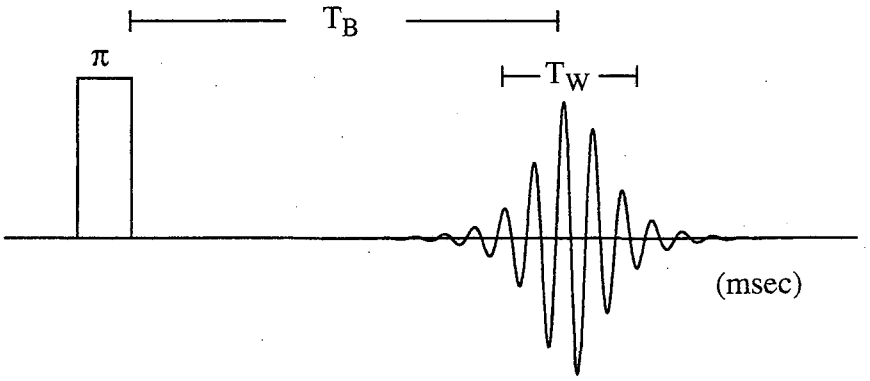

Figure 3.5 Radiation damping burst following a π pulse. The full-width at half-height is T_w and T_B is the time between the excitation pulse and the maximum of the damping burst.

The condition where $c_n \geq 1$ thus defines an effective maser threshold for the system. It is this behavior that we will seek to exploit to create a supersensitive detector. If we can create a coherent seed from a dilute spin subsystem that induces a damping burst, measuring changes in T_B we will give us mechanism for detecting that dilute spin system. The question remains, how small can the seed magnetization be?

In theory our detection is only limited by the size of the natural seed mechanisms. If our coherent seed magnetization is larger than these natural seed mechanisms, the coherence should be detectable. To address this question of detector limits, we need a better understanding of the nature of the natural seed magnetization. In normal situations a natural seed is created via two mechanisms; inaccuracies in initial pulse length and accumulation of thermal coil noise. Inaccuracies in pulse length can be minimized by the application of a magnetic field gradient pulse. A magnetic field gradient pulse following a RF pulse of $\pi + \varepsilon$, where ε is a small error, will cause the transverse components of v to quickly dephase. Once incoherent this error can not act as a seed and will not induce a reaction burst. This process of applying a magnetic field gradient following a RF pulse effectively "cleans up" the transverse magnetization. Coil noise thus serves as the fundamental detection limitation. In typical high-resolution commercial probes coil noise is on the order of nanogauss. This means that we should be able to lower the detection limitation of NMR to $\sim 10^{15}$ spins.

3.3 Experimental

This section will outline the experimental details of the studies presented in this chapter. It will begin by describing the various spectrometers used to produce the data presented in the next section. Then some attention will be paid to our choice of model samples. Finally pulse sequences used for collecting data in these experiments are described.

3.3.1 Experimental Set

Experiments were performed on one of three commercial instruments to be designated A1, A2 and A3. A1 is a Chemagnetics Infinity spectrometer operating at 9.4 Tesla. It utilized a Bruker, single resonance, direct detection probe, tuned to 400 MHz and capable of producing 5 μsec $\pi/2$ pulse. We found that this 9.4 Tesla magnetic field was a lower limit for performing radiation-damping experiments. While this spectrometer did not have an attached gradient stack, a linear Z-axis pulsed magnetic field gradient of 56 G/m could be initiated with the Z1 shim coil. This gradient had the distinct disadvantage of long rise times (1-10 msec) and long ring down times (1-10 msec).

A2 and A3 are Bruker DRX 500 and DRX 600 spectrometers operating at 11.4 Tesla and 14.1 Tesla respectively. Each utilized a Bruker triple resonance probe capable of producing 7 μsec $\pi/2$ pulse. Both were equipped with a gradient stack capable of producing linear pulsed field gradients of arbitrary duration and shape along the X, Y and Z axis. The maximum gradient strength

of A2 and A3 was 0.5 T/m. The rise time and ring down time for both probes was on the order of 0.01 msec.

3.3.2 Samples

The radiation damping time constant, T_R, is directly proportional to the sample magnetization, M_0. Thus we sought to choose simple systems with high spin density. This requirement is met when one uses protonated solvents such as water and benzene. In the case of water we have an approximately 110 molar proton concentration where in the case of neat benzene we have an approximately 74 molar proton concentration. For all of our "just solvent" studies we relied on a deionized mixture of 90% water and 10% D_2O. The deutererated water was incorporated to insure a sufficiently strong deuterium lock signal for shimming.

Our studies developed to push the NMR detector limitations necessitated a model solvate. As will be seen in the next section, this solvated species needed to have a ^1H-^{13}C J -coupled spin pair. This was accomplished with ^{13}C enriched benzene. We utilized the largest coupling, J_{HC} = 154 Hz, for our investigation. We used a 5% labeled benzene in benzene solution with 10% D_6C_6. Again, deuterated solvents insured a sufficiently strong deuterium lock signal for shimming.

All studies were performed in susceptibility matched Shigami NMR tubes. The susceptibility matching reduced artifacts that broaden spectral features, effectively raising T_2^* and increasing the damping efficiency. These tubes also allowed us to restrict the sample volume. In this way we could be sure that the

sample was directly in the middle of the receiver coil here reducing pulse imperfection artifacts.

3.3.3 Pulse Sequences

This section will outline the pulse sequence used in this study. Actual experimental parameters will be given as needed. As might be expected, calibrating inversion time in the presence of the radiation damping reaction field can be problematic. We developed a simple protocol where by the reaction burst is used a π metric.

3.3.3.1 Simple Gradient Clean-up

As noted earlier, imperfect π pulses leave a small magnetization component in the x-y plane. This small transverse magnetization can seed a damping burst. To ensure that this does not induce the seeding process, we need a mechanism for removing the pulse imperfections. A linear magnetic field gradient causes transverse magnetization to dephase quickly. Once dephased it can not seed the damping burst. Figure 3.6 depicts the general "clean up" pulse sequence. Here we see that following a θ pulse of arbitrary length a linear magnetic field gradient along the z-axis is applied. For θ close to π this sequence simply produces a noise-seeded damping burst. This sequence can also be used to measure damping bursts as a function of c_n. Taking note that $c_n = T_2^*/T_R$ and $T_R \propto 1/M_0$ we see that c_n is proportional to M_0. Thus, by varying θ before the gradient we can adjust the initial M_0 and in turn c_n.

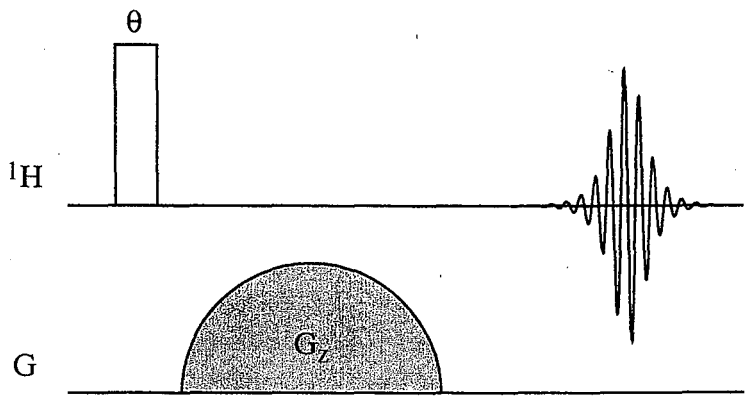

Figure 3.6 Clean up gradient pulse sequence. Following a pulse of arbitrary length a linear magnetic field gradient is placed along the z-axis to quench the transverse magnetization. We found that a 0.5 T/m gradient applied for 1 msec sufficiently dephased all transverse components.

3.3.3.2 Hole Burning

In equation 3.19 we found that for a symmetric distribution of isochromats $\phi = 0$. Because of this, there is no phase accumulation during the radiation damping reaction pulse. One should be able to detect if this symmetry is broken as a modulation of the damping burst. This could be useful in cases where a dilute solvated spin system has a resonance line under a solvent peak. Figure 3.7 shows a hole burning pulse sequence used to induce an asymmetric distribution.

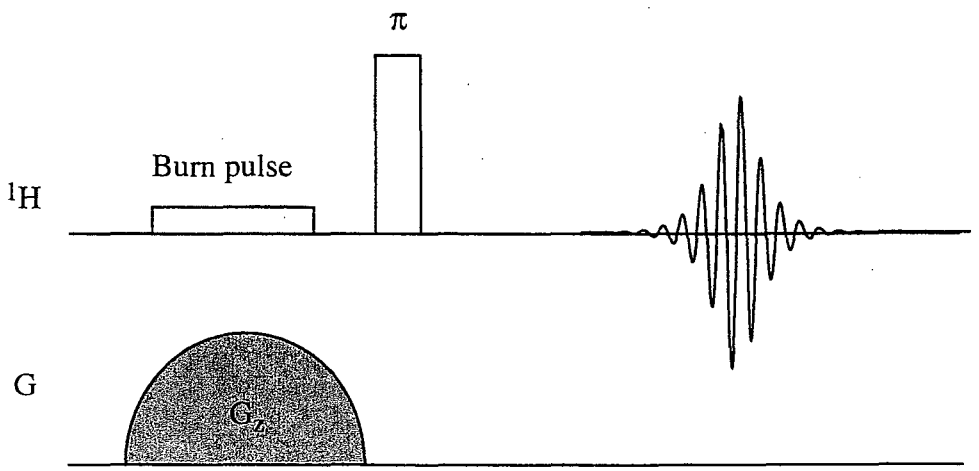

Figure 3.7 Simple hole burning experiment used to create an asymmetric lineshape. Prior to inversion, a field z-field gradient is placed across the sample while a low power RF field selectively saturates a portion of the magnetization. The gradient can be extended during acquisition to acquire a one-dimensional image.

Here while a magnetic field gradient pulse is applied along the z-axis, a long, low power, RF field is used to saturate one portion of the resonance line. This in breaks the symmetry of the distribution. A π pulse is then applied to induce a radiation damping burst modified by ϕ.

3.3.3.3 Sphere Hopping

The application a π pulse at the maximum of the damping burst offers us a means of reversing the radiation damping evolution. Figure 3.8 shows the evolution of the central isochomate following a π pulse.

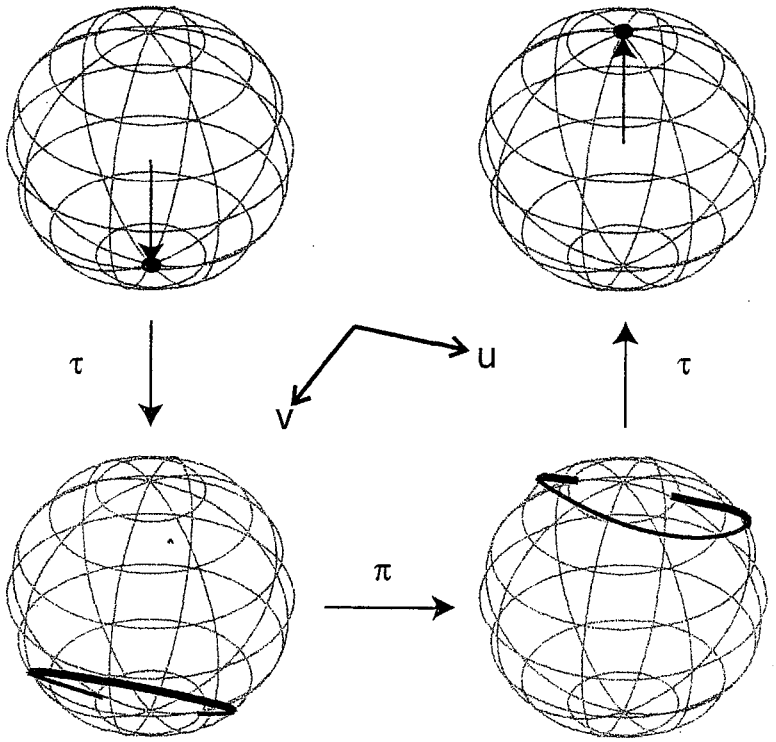

Figure 3.8 Evolution of the central isochromat during a sphere hopping experiment. After the application of the first π pulse the magnetization lies along the –z-axis. The system then evolves under the damping field for a time τ. A second π pulse inverts the system and at a time τ the central isochromat returns to the +z-axis.

A second π pulse, at the burst maximum depicted in figure 3.9, "hops" the system to the right hand evolution sphere of figure 3.8, where the system evolves back towards the +z-axis. As will be reported later, this two π-pulse sequence is able to remove some of the spectral broadening caused by radiation damping.

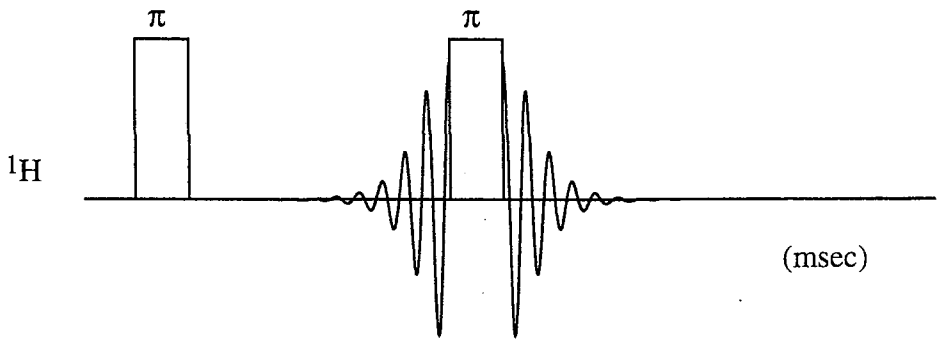

Figure 3.9 Basic sphere hopping sequence. At the maximum of the radiation damping burst a π pulse is used to reverse the isochromat evolution.

The application of a series of sphere-hopping sequences, figure 3.10, offers us a more sensitive means of monitoring the cumulative effects of ϕ, due to an asymmetric isochromat distribution. In 3.10a we see series of simple sphere hopping two π-pulse sequences linked together, with every odd π pulse centered at the maxima of the damping burst. In b.) and c.) we see two preparation stages. b.) is basically no preparation and c.) depicts the preparation of a asymmetric isochromat distribution. As in section 3.3.4.3, a field gradient is used in conjunction with a long, low power pulse to selectively saturate a portion of the solvent magnetization and break the symmetry of the isochromat distribution.

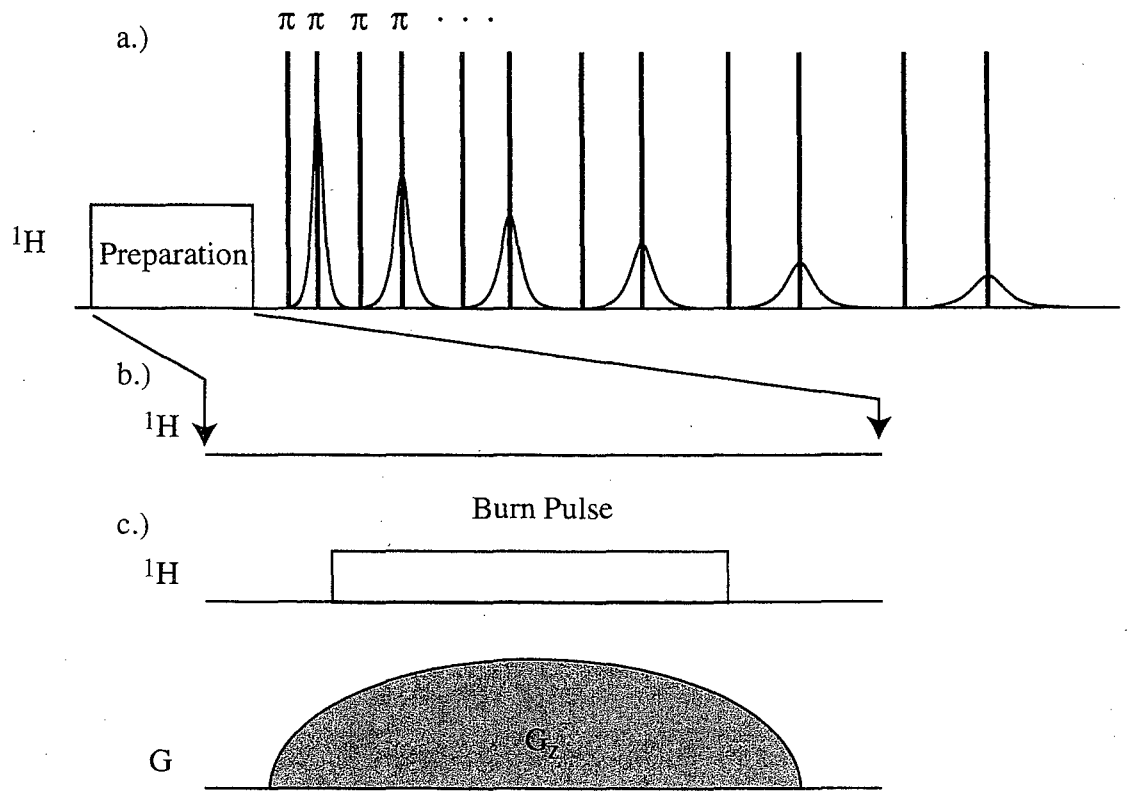

Figure 3.10 Sphere hopping train. a.) depicts a series of two pulse sphere hopping sequences with every second π pulse applied at the subsequent damping burst maximum. b.) no preparation of the magnetization prior to the pulse train. c.) a hole burning sequence applied to prepare an asymmetric distribution.

3.3.3.4 Injection Seed

As noted earlier, we hope to detect a small transverse magnetization by its ability to coherently seed a radiation damping burst. To test the validity of this idea and gain some insight into the practical detection limits, we designed the pulse sequence depicted in figure 3.11.

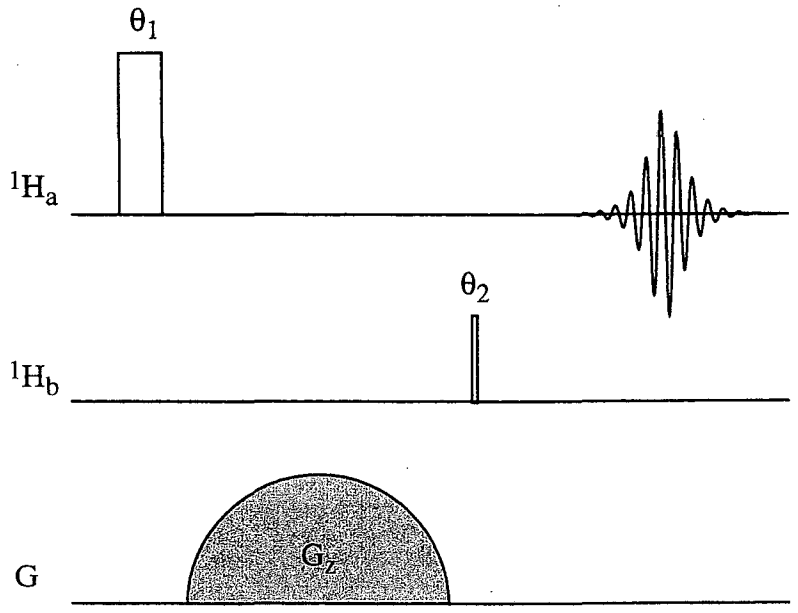

Figure 3.11 Injection seeded maser. Following a clean up gradient sequence a short low power pulse θ_2 is applied to act as a coherent seed for the damping burst.

The first portion of the injection seed experiment is the simple gradient clean up sequence in section 3.3.4.1. Following this preparation a second, very small, ^1H seeding pulse is applied. By varying the length of θ_2 we can adjust the magnitude of the coherent seed.

3.3.3.5 Modified Inverse Inept

To test whether a solvated spin system can be detected as a modulation of a damping burst we need a pulse sequence which affords transverse magnetization from the solvated spin system while leaving the solvent magnetization along the –z-axis. This was accomplished with a modified inverse inept[6] sequence seen in figure 3.12.

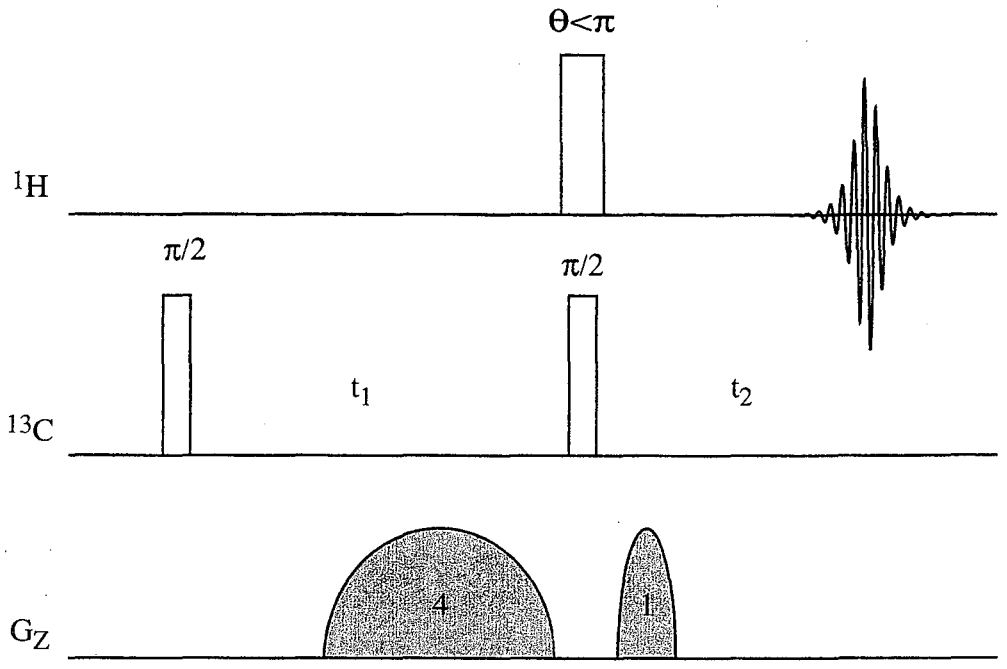

Figure 3.12 Modified inverse inept sequence. The θ pulse followed by the field gradient acts as a clean up gradient sequence, leaving the solvent magnetization scaled along the –z-axis. Dilute ^{13}C-^{1}H pairs induce a small proton coherence through their J-couplings, that triggers the damping burst.

The pulse sequence begins with a $\pi/2$ pulse on the ^{13}C that moves the carbon magnetization into the transverse plane. Ignoring the gradients for the moment, the system is allowed to evolve under J-coupling and chemical shift (set to near zero) for a period of time t_1 at which point simultaneous pulses are applied to both the proton and carbon channels. For the special case where $\tau_1=1/2J_{HC}$ and both the second pulse on both channels is $\pi/2$ (normal inverse inept), proton magnetization from the J coupled pair will be detected at a $\tau_2=1/2J_{HC}$. Using product operators[7,8] we can follow the magnetization evolution, figure 3.13.

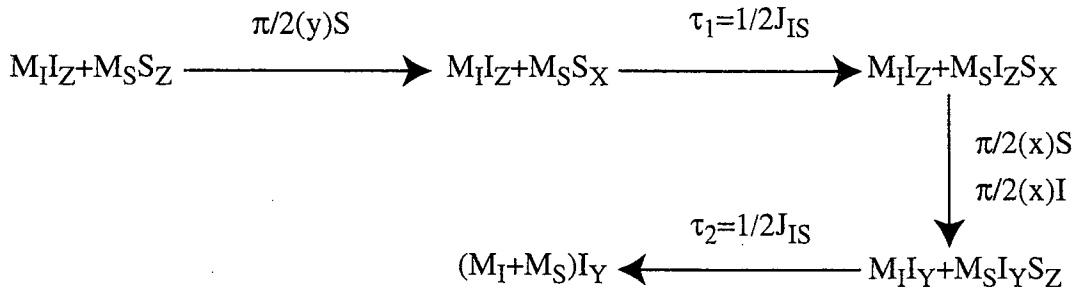

Figure 3.13 Magnetization evolution during normal inverse inept sequence. By choosing $\tau_1=\tau_2=1/2J_{IS}$ we can generate I_Y magnetization from the J coupled spins.

Here we see that the two spin anti-phase operator generated at the end t_1 becomes coherent ^1H magnetization following the simultaneous pulses. This coherence is what we had hoped to use to seed the damping burst. However, only half of our problem is solved. The non-coupled ^1H solvent spins end up in the transverse plane following the ^1H $\pi/2$ pulse instead of being along the –z-axis.

Clearly we need the proton pulse to act as π pulse for the solvent and a $\pi/2$ pulse for the solute. To accomplish this we use the same clean up gradient method described in section 3.3.4.1. We adjust the proton pulse length between $\pi/2$ and π followed by a clean up gradient (x1). The transverse components of the solvent magnetization are dephased leaving the solvent magnetization scaled along the –z-axis. This also dephases the two-spin anti-phase coherence which in principle leave us without our coherent seed. To combat this a preparatory gradient (x4) is implanted prior to the proton pulse. The first gradient effectively pre-wraps the anti-phase magnetization. The net effect of the second gradient is to rephase (rather than dephase) the anti-phase two-spin coherence. The relative magnitudes of the gradients are 4:1 compensating for the difference between the carbon and proton gyromagnetic ratios.

3.4 Results and Discussion

This section will present our preliminary results [9]. The first portion will be dedicated to building and testing the experimental modules described in section 3.3.3. Here we will seek to better understand the practical manifestations of the damping burst. The second portion will report our initial attempts at utilizing radiation damping to detect isolated spins. Here we will outline two types of experiments. The first is geared towards detection of a solvate spin that disrupts the distribution of the solvent isochromats. The second describes our attempts to induce a damping burst with a coherent solute seed.

3.4.1 Understanding the Burst

To utilize the damping burst we must insure that our theoretical suppositions are founded. First we need a mechanism for making sure that our clean-up gradients are able to create a situation where the damping burst is seeded by noise. Next we will test the validity of equation 3.25 and its solutions in figure 3.4 by adjusting the ratio c_n. Then we will report a simple mechanism for removing the broadening due to radiation damping in an inhomogenous field.

3.4.1.1 Clean-up Gradients

The purpose of the clean-up gradient is to ensure a noise induced damping burst. Our first order of business is to develop a metric whereby we

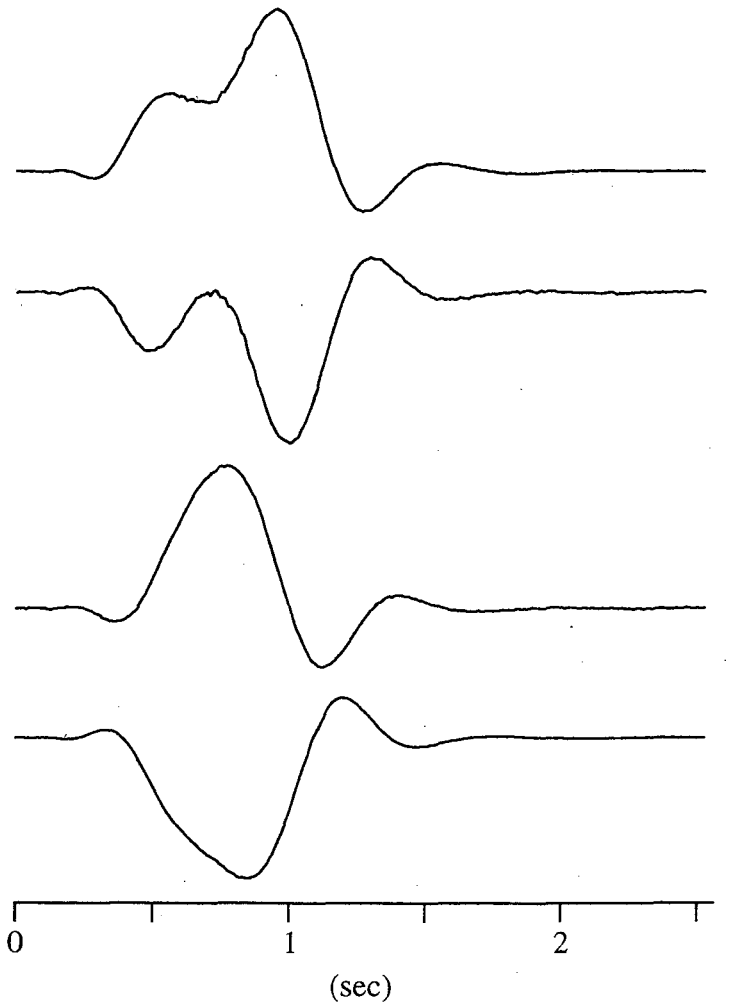

Figure 3.14 On resonance damping burst using a clean up gradient pulse sequence with an initial tip angle of π. Each FID was taken under identical conditions with a 25 second delay between trials. The random burst phase implies that the damping event is induced by an incoherent source.

can differentiate between a noise-seeded burst and a burst seeded by coherent stray x-y magnetization. To accomplish this we take advantage to the fact that any seed generated.by noise will have random phase. As such any damping burst resulting from a noise seed will also have a random phase. Thus a quick check to determine the origin a damping burst is to monitor the burst phase following the application of the magnetic field gradient for a number of identical experiments. Figure 3.14 depicts a characteristic series of four such measurements taken on spectrometer A2 with a sample of 90% H_2O/10%D_2O. Here we see that each burst has a distinct and different phase. We can thus be sure that the damping burst has been induced by noise. A similar set of spectra is taken in each of the following experiments that utilize a gradient clean up module.

3.4.1.2 Noise and Start Up

To use T_B as a metric we need to have a better understanding of the noise initiated burst. A theoretical treatment of this problem is currently being addressed [10]. Our initial findings indicate that, under a given set of experimental conditions, we can only derive an average noise induced burst time that fluctuates from experiment to experiment with a characteristic jitter. We noted that the noise induced burst time fluctuates from 1-5%. This can be seen in figure 3.15 and figure 3.16.

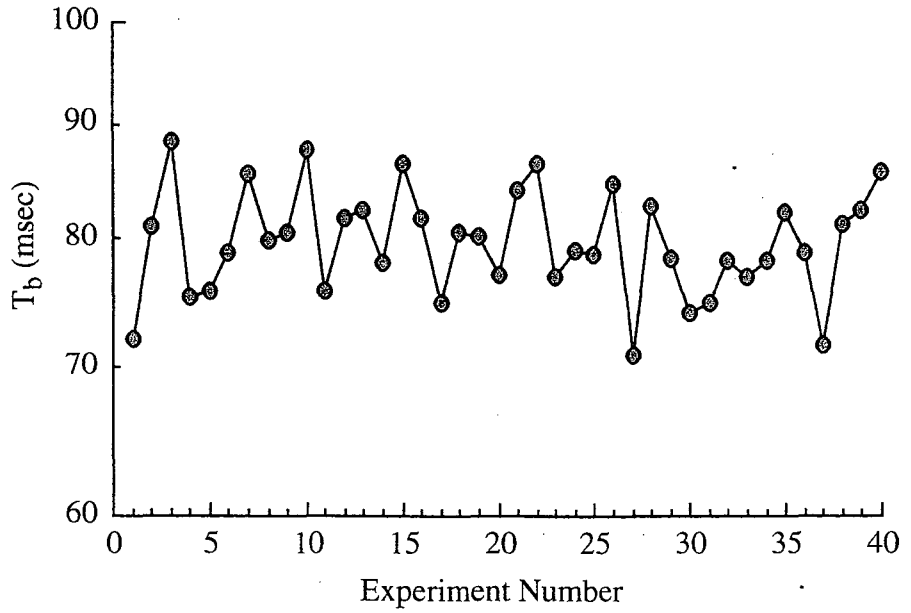

Figure 3.15 Damping burst time for a series of identical inversion experiments. The delay between experiments was 10 seconds.

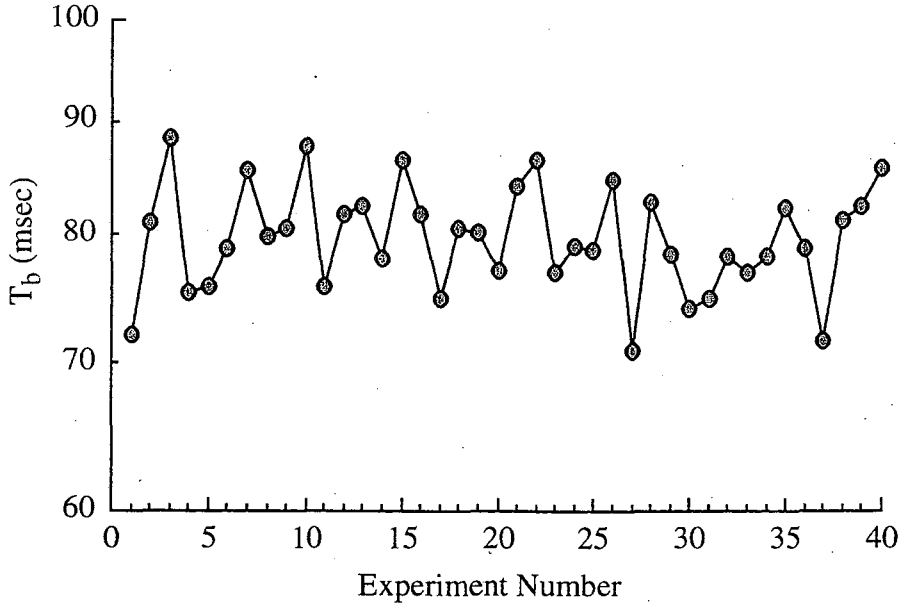

Figure 3.16 Damping burst time for a series of identical inversion experiments. The delay between experiments was 25 seconds.

There we see the burst T_B plotted for a series of identical noise induced bursts taken with the A1 spectrometer using a sample of pure water. To ensure that each experiment has the same initial starting conditions the delay time between each experiment were a.) 10 sec and b.) 25 sec, both at least $5xT_1$. The average burst time was 80 msec and 78 msec with a standard deviation of 4 and 5 msec for figure 3.15 and 3.16 respectively. The standard deviation gives us a handle on the magnitude of the burst jitter. We thus realize a finite limitation in our ability to use T_B as a diagnostic. We can only measure changes greater than the burst jitter. This drawback can be minimized when we average the absolute value of multiple scans.

3.4.1.3 Maser Threshold

In section 3.2 we developed a theory to determine the extent to which the radiation damping reaction field will drive the central isochromat of a symmetric distribution back towards the +z-axis in the presence of an inhomogenous field. From this we derived the simple relationship between $\Delta\theta$ and T_2^*/T_R in equation 3.25. In the case where the initial tipping pulse is π, graphical solutions to 3.25, figure 3.4, predict that above a threshold value of $c_n = T_2^*/T_R > 1$, a coherent seed can induce the system to mase. This maser action is detected as a damping burst, as described above. Conversely, when $c_n > 1$, the system is below the maser threshold, and no damping burst is predicted.

Here we will experimentally verify that this maser threshold exists. To accomplish this we need to record a series of damping bursts as a function of c_n. But the question arises, how does one vary c_n experimentally? As outlined in section 3.3.3.1, we note that $c_n \propto T_R^{-1}$ and that $T_R \propto M_0^{-1}$ and thus we see that

varying the initial magnetization, M_0, is a mechanism for gaining experimental control over c_n. While this is by no mean the only way of adjusting c_n, it is by far the most experimentally expedient.

The simplest means of varying M_0 is to use the gradient clean up sequence described in section 3.3.3.1. By incrementing the initial tip angle, prior to the application of the dephasing gradient, we can effectively scale M_0 and in turn scale c_n.

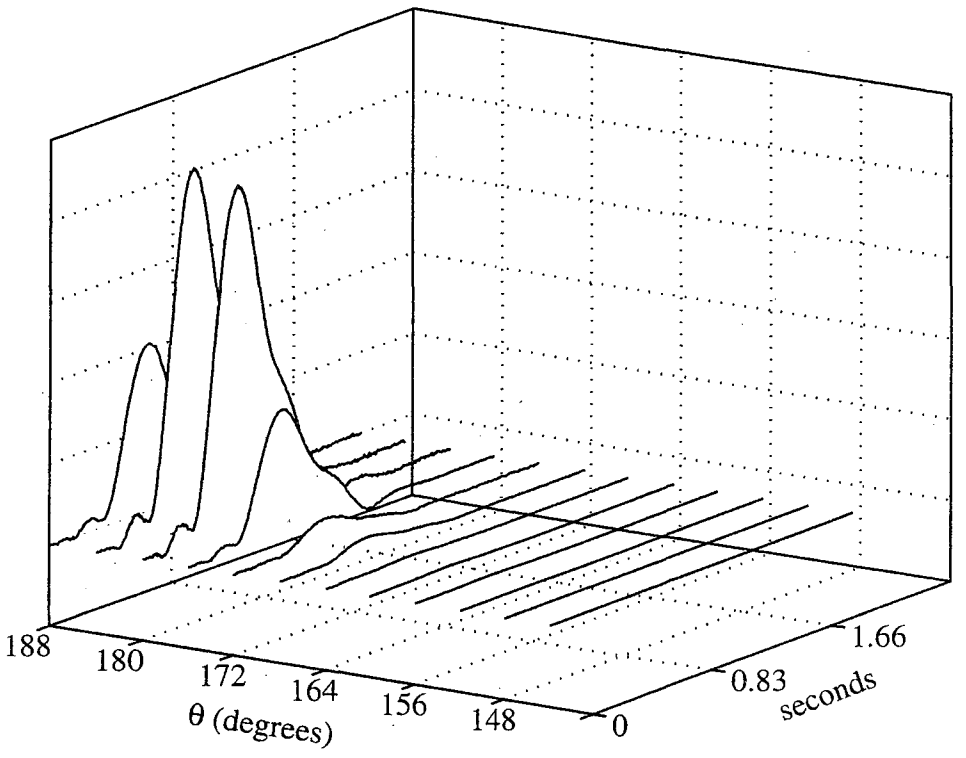

Figure 3.17 Plot of the magnitude of damping burst following a gradient clean-up sequence as a function of the initial tip angle θ. For θ below 172° the burst there is no damping burst indicating that this is below the maser threshold.

Figure 3.17 plots of a series of damping bursts taken on A2 with a water sample using the gradient clean-up pulse sequence. The initial tip angle, prior to the field gradient, is varied from 188° to 148°. To avoid complications due to burst jitter, each damping burst is the average of the absolute value of ten independent measurements. As expected, there is a threshold θ value, below which no burst is generated. This directly supports our theory. This threshold effect can be seen even more clearly in figure 3.18.

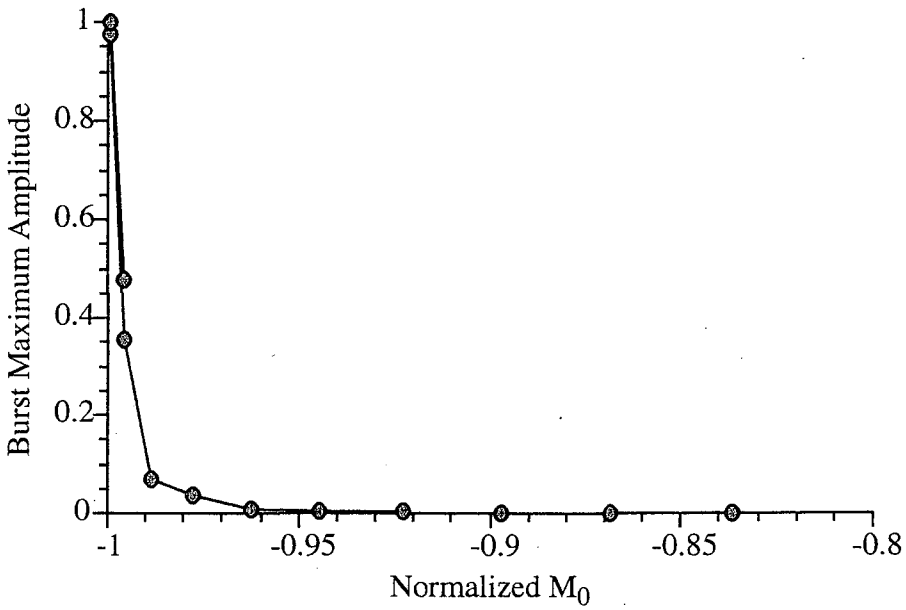

Figure 3.18 plot of burst amplitude as a function of M_0 for data. This plot utilized the data presented in figure 3.17.

Here we see a plot of the maximum intensity of the damping burst as a function of a normalized M_0. The burst threshold cutoff is dramatic and occurs over a very narrow range of M_0.

3.4.1.4 Sphere Hopping and Narrowing

As pointed out earlier, it is often advantageous to eliminate the broadening due to radiation damping. To this end we have met with limited success using the sphere hopping sequence detailed in section 3.3.3.3. In figure 3.19 a.) we see the FID (black) resulting from a "normal" $\pi/2$-detect experiment preformed in an inhomogenous field.

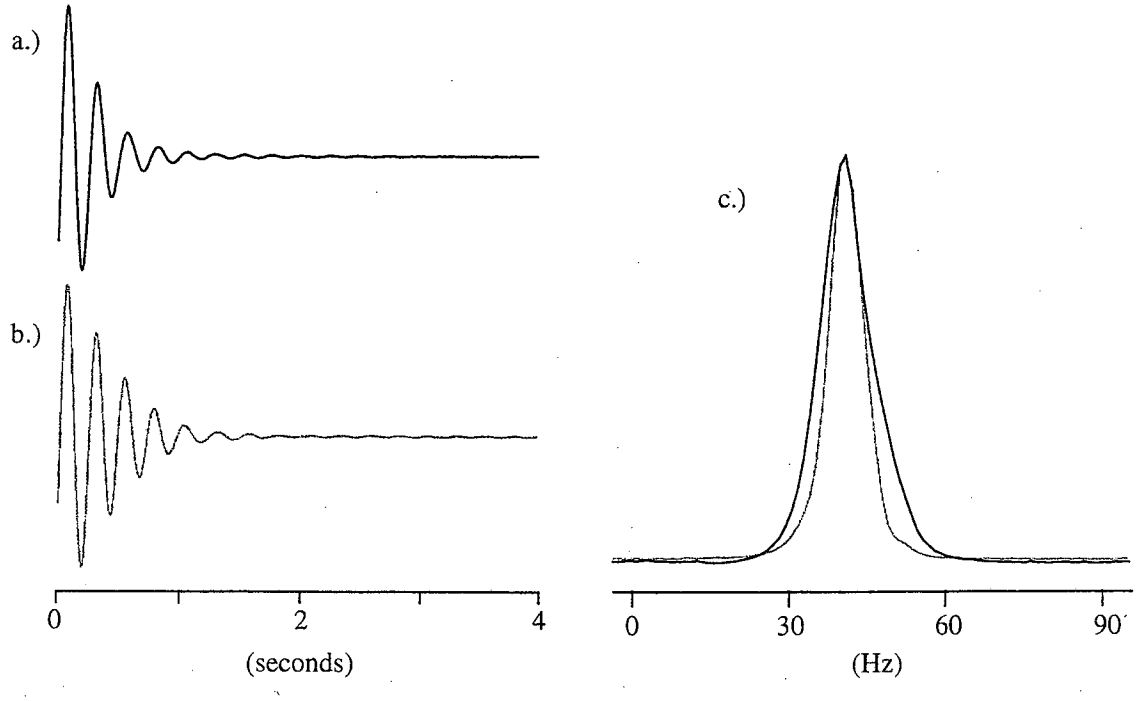

Figure 3.19 Removing the effects of radiation damping using sphere hopping sequence. a.) shows a FID for a pure water sample following a $\pi/2$ pulse in the presence of radiation damping. b.) is a FID for pure water following a two π-pulse hopping experiment where the second π pulse is placed at the maximum of the damping burst. c.) shows the corresponding Fouier transformed spectra superimposed. The black spectra results from a.) while the gray spectra results from b.). Both a.) and b.) were taken under identical conditions using A1.

This data was taken in the presence of a radiation damping reaction field, on a sample of pure water using A1. In b.), with the same sample and spectrometer set up, we see a FID (gray) resulting from a two-π sphere hopping experiment.

3.4.2 Towards Detection Enhancement

Our overall goal is to utilize the sensitive non-linear nature of radiation damping, to create a sensitive detector. This section will report our preliminary results for two types of experiments. The first seeks to utilize the sensitivity of the radiation damping field to the symmetry of the isochromat distribution. Here we will report our initial finding using a train of sphere hopping modules. The second family of experiments seeks to utilize the maser characteristics of the radiation damping burst to detect small transverse magnetization components induced from a dilute solute spin system. To this end we will present data that shows that a small coherent seed can induce the maser action and our preliminary results detecting dilute ^{13}C-^{1}H spin pairs in benzene.

3.4.2.1 Sphere Hopping Train

One potential means of detecting dilute spins, using radiation damping, is to take advantage of the fact that dilute resonance, however small, near the solvent resonance, will break the symmetry of the solvent line. As we have noted, an asymmetric distribution leads to the accumulation of a phase ϕ, that in principal should be detectable as an augmentation of a damping burst. To test the utility of this idea we developed a method for artificially breaking the

symmetry of the solvent resonance line. As described in section 3.3.3.3 we can use a gradient and a long low-level hole-burning pulse to selectively saturated one portion of a spectral feature. Figure 3.20 is a one-dimensional image of pure water with (gray) and without (black), a hole-burning pulse taken on A1.

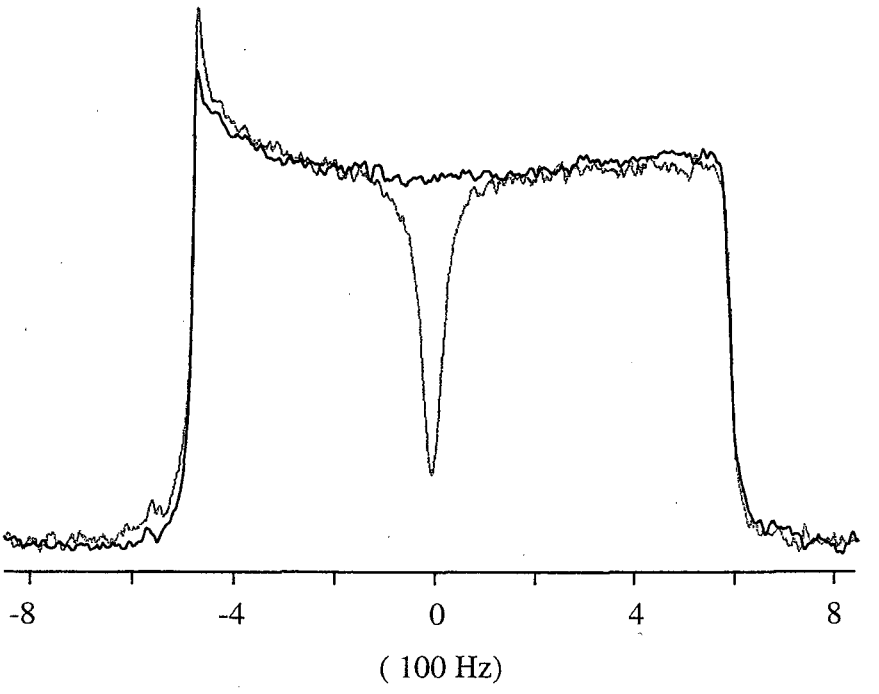

Figure 3.20. One-dimensional water images with and without hole burning. The black image was obtained without a burning pulse. The gray image was obtained with A1 using a linear field gradient of 56 G/m and a 10 msec burn pulse zot.

In figure 3.20 we see that the linear magnetic field gradient left on during acquisition, imparts a spatial dependence upon the resonance condition. In the gray image we see that the spins excited by the hole-burning pulse are saturated, leaving a notch "burned" into our one-dimensional image. When we turn the gradient off during acquisition we see the normal one-dimensional spectra

depicted in figure 3.21.

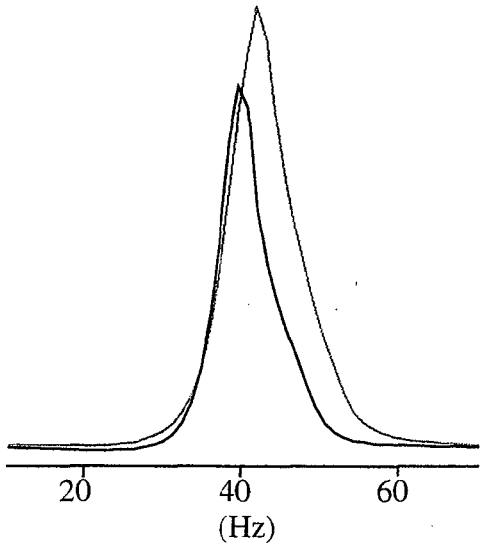

Figure 3.21. Water spectra with and without a pre-saturation pulse. The gray line is a normal water spectrum. The black line is the spectrum acquired when a hole burning preparatory pulse is applied. The preparatory pulse is used to break the symmetry of the initial distribution.

The gray spectrum depicts the case of no-hole burning where we obtain a symmetric distribution. The black spectrum has been made asymmetric with a hole burning pulse.

The question then becomes, can we detect this change as a modulation of the damping burst? We accomplished this by utilizing a train of sphere hopping experiments outlined in section 3.3.3.3. In this experiment series of two π-pulse sphere hopping modules are linked together where every second π pulse is placed directly at the maximum of the damping burst. Figure 3.22 depicts a train of 16 pulse pairs applied to a sample of pure water on A1

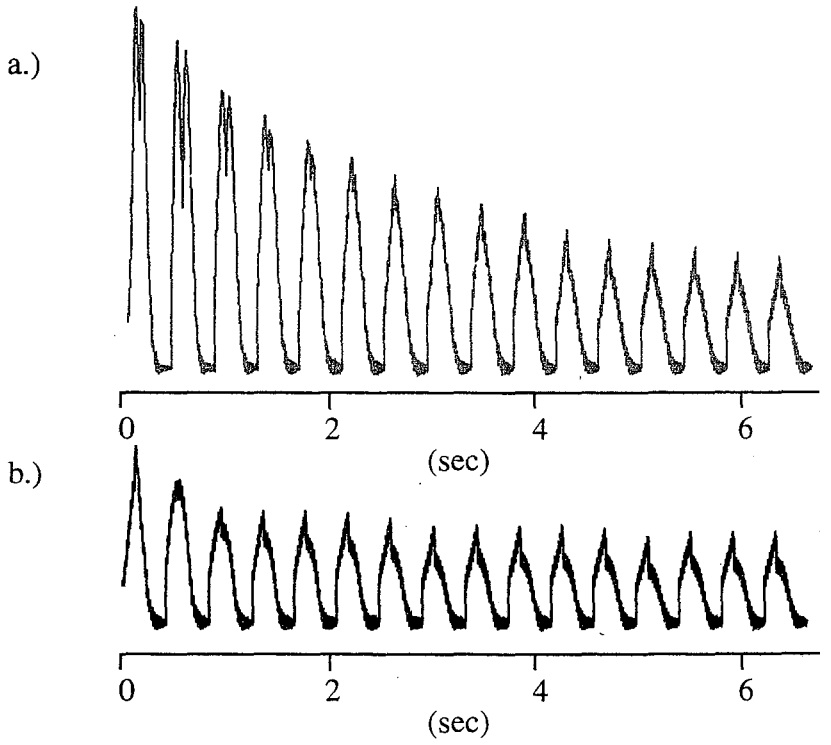

Figure 3.22 Sphere hopping pulse train results for water sample. a.) a symmetric initial distribution. b.) an asymmetric initial distribution. The addition of a ϕ, caused by breaking the magnetization symmetry, induced a dramatic change in the amplitude profile.

Figure 3.22 a.) depicts the series that results from a symmetric distribution and b.) depicts the burst chain resulting from a the gradient-prepared asymmetric distribution described above. Clearly the asymmetry induces a drastic change in amplitude profile. Figure 3.23 is a plot of burst maximum as a function of time with and without the hole burning pulse.

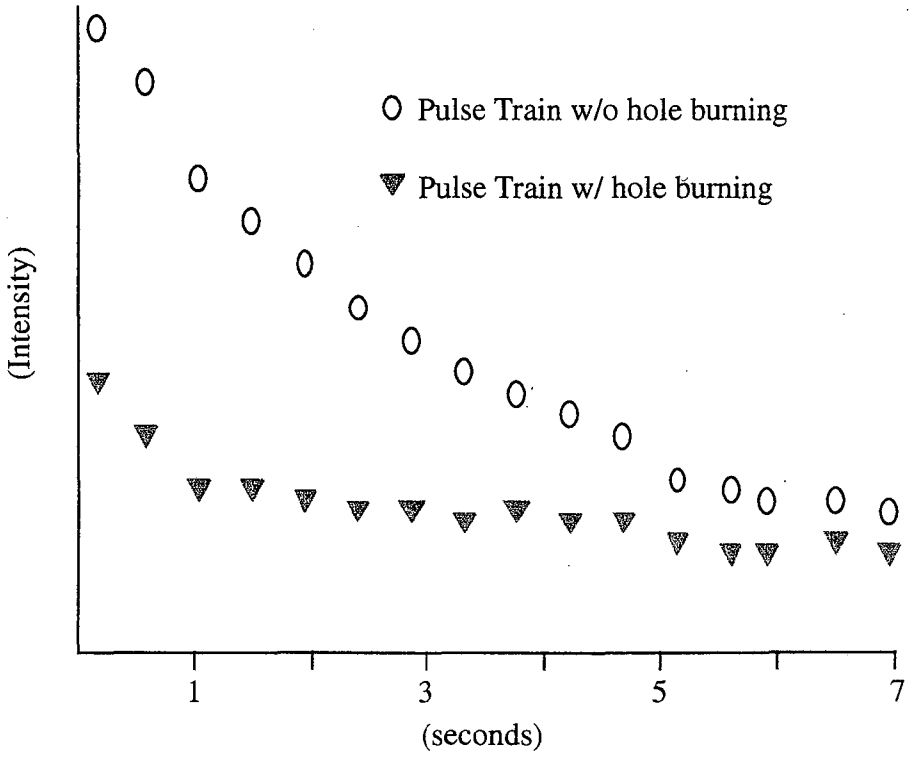

Figure 3.23 Plot of pulse train maximum as a function of time. Again, ϕ induces a dramatic change.

Here we see a dramatic difference between the amplitude profile without hole burning (ovals) and with hole burning (gray triangles).

Backing out useful information from this profile change has been, to date, problematic. What we can see is that the sphere hopping train is able to magnify the effect of an asymmetric distribution. As such, its current use, is limited to asserting whether there is or is not a reduction of symmetry.

3.4.2.2 Injection seeded Maser

The second means of exploiting the damping burst to detect a dilute solvated spin system relies on the dynamics of a coherent seed. If we can create a coherence from a solvated spin system, while the solvent magnetization is inverted, that coherence should induce the solvent magnetization to mase . As such, we should be able determine the relative magnitude of this dilute coherence by measuring its effect on T_B. As an initial model of the dilute coherence, we have incorporated a low power seed pulse as described in section 3.3.3.4.

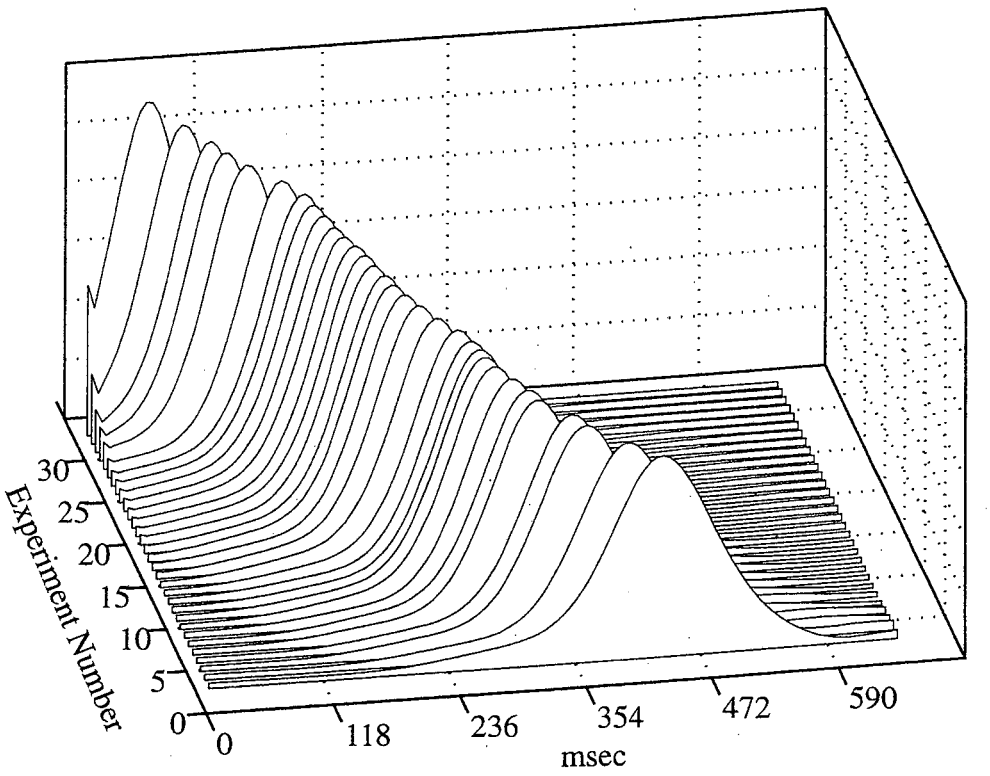

Figure 3.24 Damping bursts for a series of injection seeded experiments. The absolute value of the damping bursts is plotted to simplify the plot.

Figure 3.24 depicts a series of seeded damping bursts for a water sample using A3 and the injection seeded pulse sequence in 3.3.3.4. The seed pulse length for each experiment is given in table 3.1. The clean-up gradient length was set to 2 msec to ensure that the damping bursts were not induced by imperfections from the initial π pulse.

Taking the seed pulse lengths from table 3.1 we can see that as the seed length increases, the damping burst maximum, T_B, decreases. This indicates that in principle we can detect a transverse component of magnetization as a perturbation of the reaction burst, just as we had hoped. Although it is not presented here, it is important to note that the phase of the damping burst becomes coherent even for the smallest seed pulse. This suggests that our metric for ensuring a noise-seeded burst is valid.

Exp #	θ (deg)	Exp #	θ (deg)	Exp #	θ (deg)
1	1.7×10^{-3}	12	7.3×10^{-2}	23	0.55
2	3.4×10^{-3}	13	0.11	24	0.62
3	1.0×10^{-2}	14	0.14	25	0.69
4	1.7×10^{-2}	15	0.18	26	1.1
5	2.4×10^{-2}	16	0.21	27	2.1
6	3.1×10^{-2}	17	0.24	28	3.1
7	3.8×10^{-2}	18	0.28	29	4.1
8	4.5×10^{-2}	19	0.31	30	6.9
9	5.2×10^{-2}	20	0.35	31	13.7
10	5.9×10^{-2}	21	0.42		
11	6.6×10^{-2}	22	0.48		

Table 3.1 Experimental seed pulse lengths.

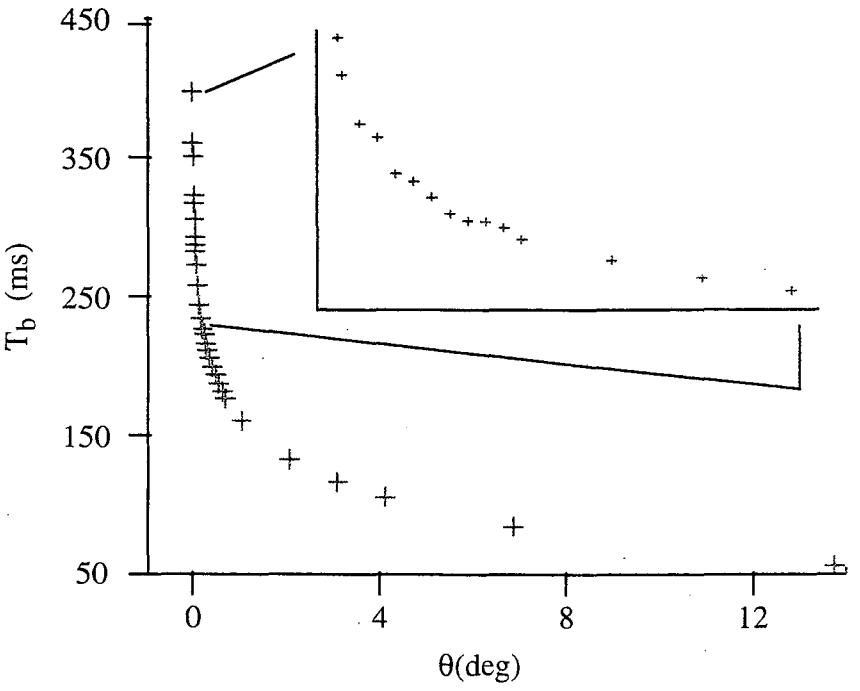

Figure 3.25 Plot of maximum burst time as a function of seed tip angle. As hoped, the burst time is highly dependent upon the magnitude of this seed pulse.

Figure 3.25 plots T_B as a function of seed tip angle. Of primary importance we see, as suspected, T_B decreases as the seed pulse length is increased. Even for the smallest values of θ, we see large changes in T_B. This indicates that a small coherent seed should translate into a large detectable change in T_B. In addressing our detection limits, the smallest value of θ, 1.7×10^{-3}°, can give us an idea of how small a transverse magnetization we can detect.

A quantitative relationship between T_B and θ can now be addressed. For a narrow line one can solve equation 3.21,

$$v = M_0 \sec h\left(\frac{t - T_B}{T_R}\right). \tag{3.26}$$

Letting t=0 we can solve for T_B,

$$T_B = T_R a\sec h\left(\frac{v}{M_0}\right). \tag{3.27}$$

But we know how v will evolve during a pulse,

$$v = M_0 \sin\theta. \tag{3.28}$$

Thus,

$$T_B = T_R a\sec h(\sin\theta). \tag{3.29}$$

Weighting each point of 3.25 by the asech(sinθ) we get the linear relation in figure 3.26.

From this simple model of coherent burst seeding, we gain our first experimental evidence that our radiation damping detection scheme is feasible. Satisfied with these preliminary results, we then sought try this detection scheme on a real system.

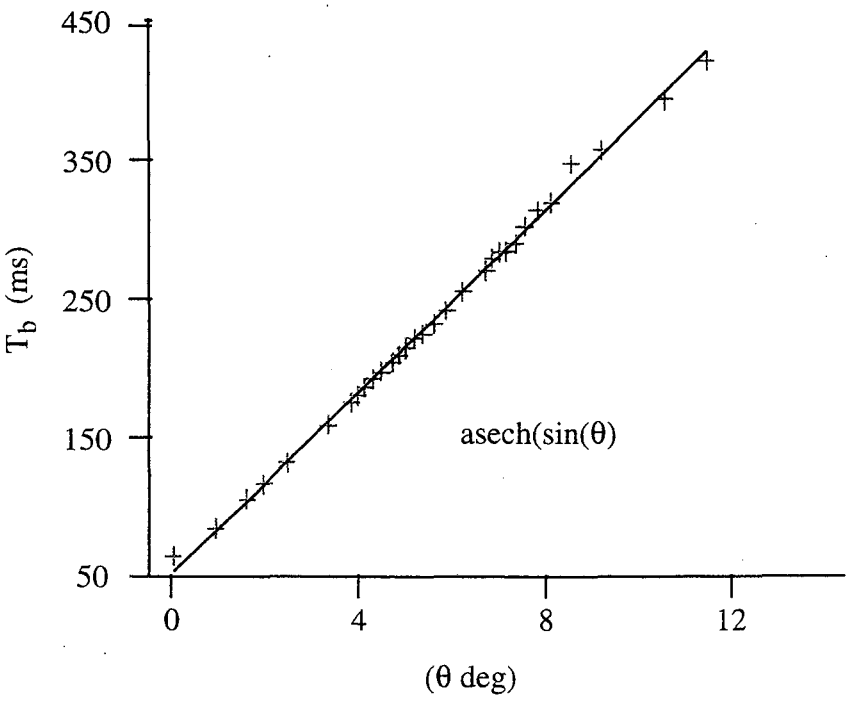

Figure 3.26. Adjusted plot of damping burst time as a function of seed tip angle. A linear plot is arrived at when each value of T_B is weighted by asech(sinθ).

3.4.2.1 *Inverse Inept*

Taking heart from our experimental evidence that changes in T_B can be induced via a coherent seed pulse, we turned our attention to the detection of a dilute spin species. Using the modified inverse inept experiment detailed in section 3.3.3.5, we attempted to create a coherent ^1H magnetization seed from ^1H-^{13}C J-coupled pairs in benzene. We should be able to scale the magnitude of the proton seed by varying τ as seen in figure 3.27. Here we see that when $\tau=(2n+1)(1/2J)$ we generate the largest proton seed. In principle we should be able to back out J_{CH} by recording damping bursts as a function of τ.

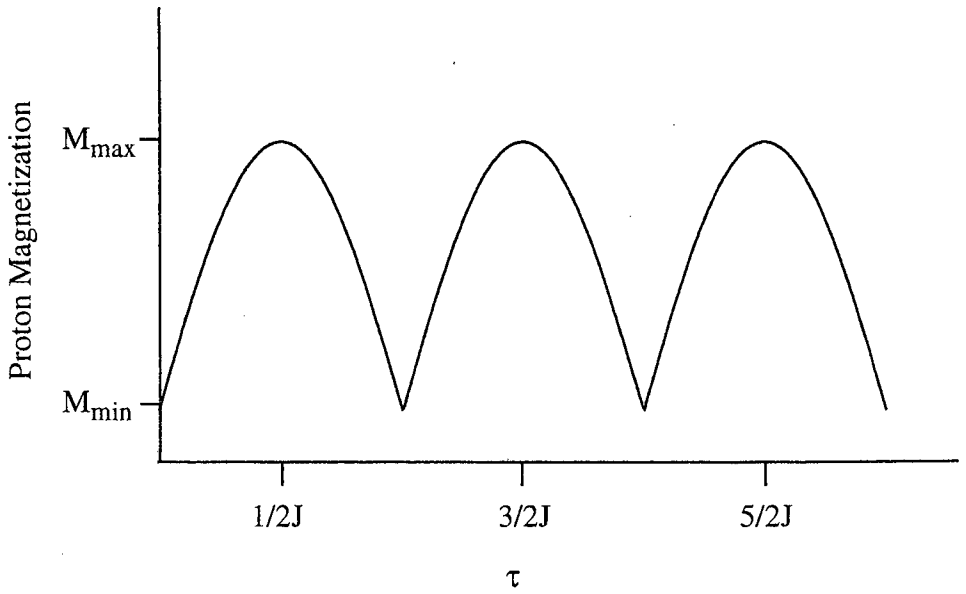

Figure 3.27 Plot of expected seed magnetization as a function of τ. At odd multiples of 1/2J the seed magnetization is maximum. Fourier transform of such a function will lead to a single line at J.

Figure 3.28 plots a series of damping bursts as a function of τ using a benzene sample on A3. The largest heteronuclear J-coupling in benzene is 154 Hz. thus 1/2J = 3.25 msec. Unlike the case where the seed is generated from a coherent pulse, here we see that the inept seeded bursts change both amplitude and position as a function of seed strength. As a qualitative note, the phase of each burst, not depicted here, is coherent. This implies that these damping bursts are generated via a coherent mechanism. Because we have eliminated all other coherences (random phase test) we can be sure that the J-coupled seed is initiating the damping event.

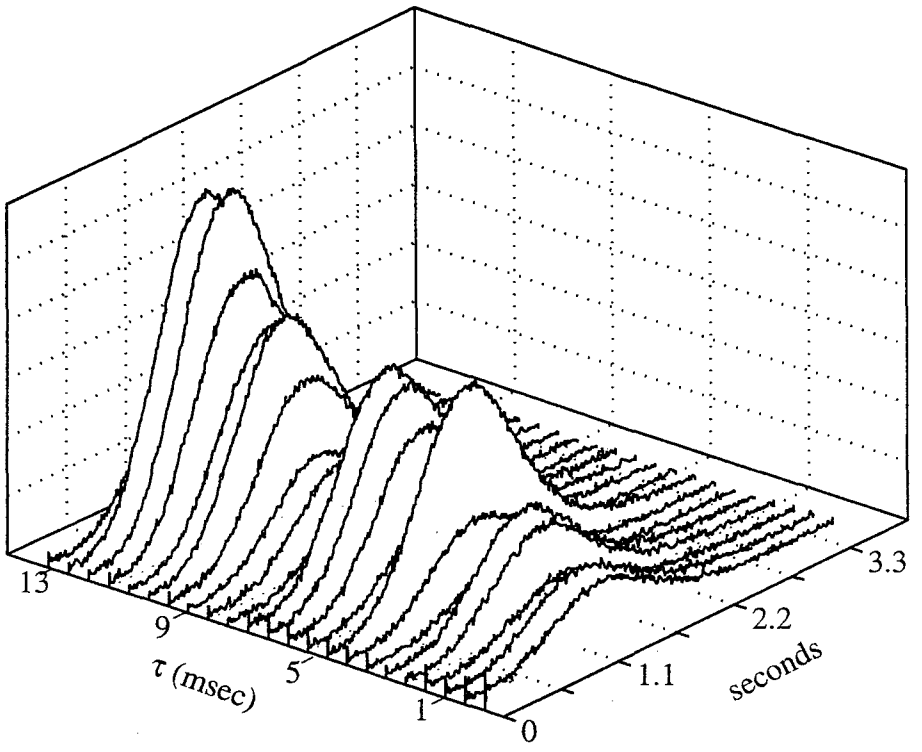

Figure 3.28 Damping bursts following a modified inverse inept sequence as a function of τ for a benzene sample. The pre-wrap gradient was 4 msec and the rephase gradient was 1 msec. The absolute values are reported.

Unfortunately quantifying these results has been, to date, problematic. Figure 3.29 is a plot of T_B as a function of τ. We do not see the periodicity that had been predicted. Rather unexpectedly, however, the burst intensity changes dramatically as a function of τ. This can be seen more clearly in figure 3.31.

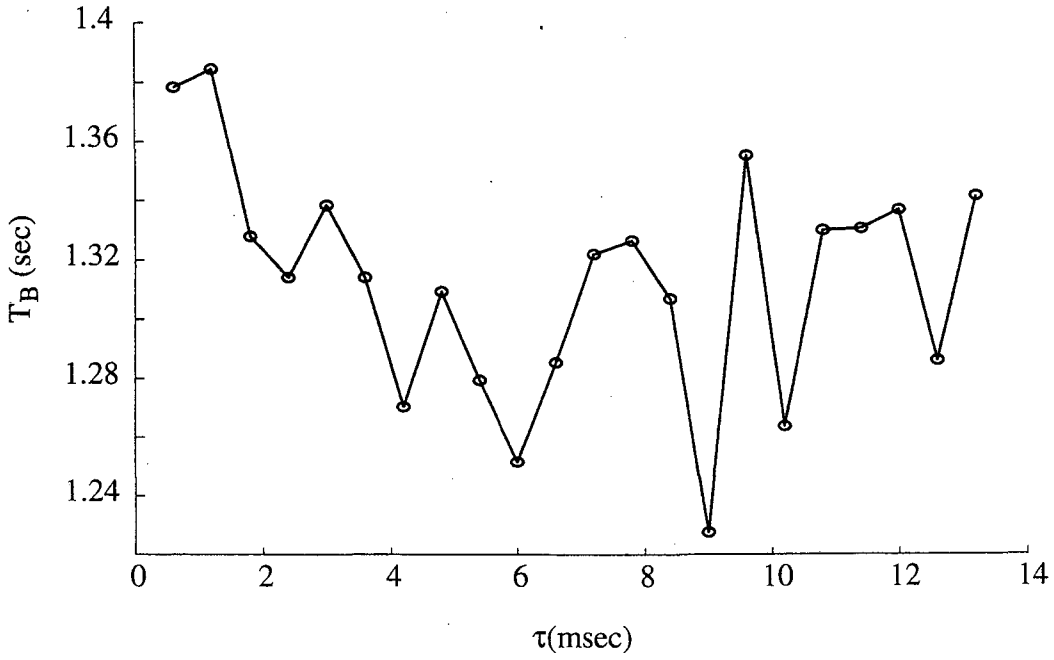

Figure 3.30 Plot of T_B as a function of τ for an modified inverse inept sequence.

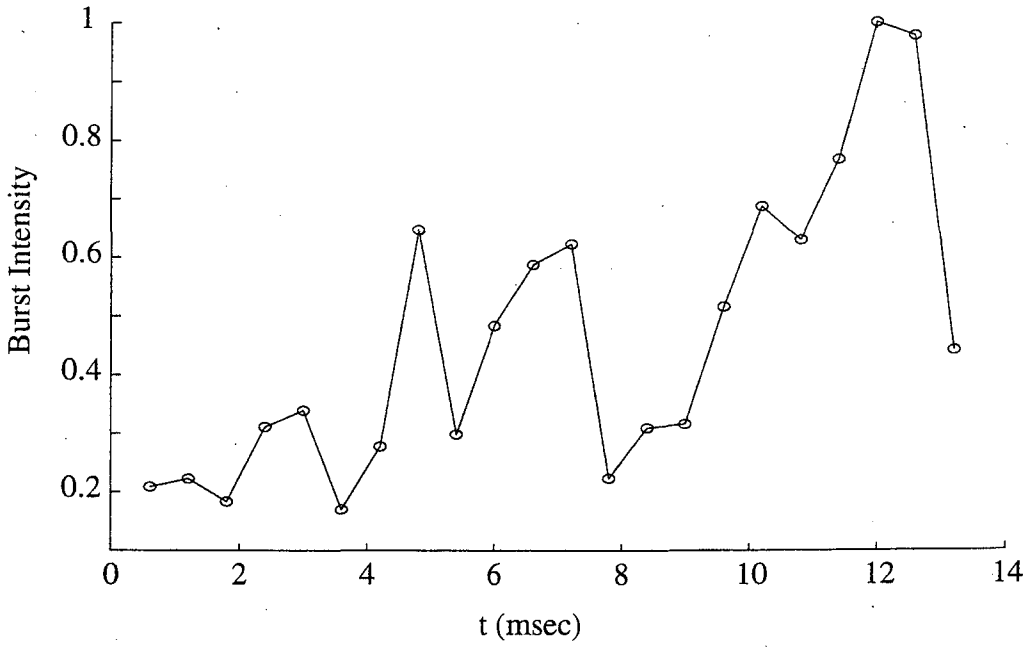

Figure 3.31 Plot of normalized damping burst intensity as a function of τ for an modified inverse inept sequence.

Here we find that the maximum burst intensity occurs when $\tau=1/2J_{CH}$. At this point we do not have a good explanation of why the burst intensity is modulated and how its intensity is related to the seeding process. To this point we have ignored the two and three bond J couplings. Because they are much smaller, they are responsible for developing coherences on a much larger τ time scale. While our initial results are inconclusive, we do see that in principle a damping burst can be modulated by a dilute coherence.

3.5 Conclusions

As NMR hardware technology advances and experiments utilize higher magnetic fields, radiation damping becomes a persistent source of line broadening and spectral distortion. In this chapter we have endeavored to understand and harness the non-linear nature of the radiation damping reaction field.

In our attempt to understand this phenomena, we developed a theory to predict, $\Delta\theta$, the extent to which the reaction field will drive the magnetization back towards the +z-axis in an inhomogeneous magnetic field. Graphical solutions to equation 3.25, for an initial tip pulse of π, figure 3.4, suggested that for certain ratios of $T_2^*/T_R=c_n>1$ the addition of a small seed pulse will induce an inverted system to mase. This is detected as a damping burst. For values of c_n below this threshold, we do not expect to see the creation of a damping burst. Using a simple protonated solvent this maser threshold was experimentally verified in section 3.4.1.3.

The broadening caused by the reaction field is a detriment to both the overall selectivity and sensitivity of the NMR experiment. As such its removal is often advantageous. In section 3.3.3.3 we presented a simple two π-pulse sphere hopping sequence that is able to remove the broadening due to radiation damping.

Next we turned our attention to developing a means of utilizing the nonlinear nature of the reaction field as a sensitive detector. In section 3.4.2.1 we showed that we can detect when the symmetry of an isochromat distribution is disrupted as a modulation of a sphere hopping train profile. In principle this in can be used to detect a solute resonance line that lies under or near the solvent line. Clearly future work should concentrate on quantifying the effects of asymmetry on the sphere hopping train profile.

For an inverted spin system, above the maser condition, a coherent seed pulse should induce a damping burst. This was verified experimentally in section 3.4.1.3 where a small tip angle pulse is used to seed the damping burst. There we saw that as the seed pulse-length increased, the damping burst time, T_B, decreased. Next we attempted to create a coherent seed from a solvated ^{13}C-^{1}H spin pair in benzene. Using a modified inverse inept sequence, section 3.3.3.5, we collected a series of damping bursts in which the magnitude of the seed magnetization created from the ^{13}C-^{1}H spin pair is varied. While we did not see a straight-forward relationship between T_B and the seed magnitude, we found a qualitative relationship between the burst maximum and the seed magnitude.

REFERENCES

1. P. Broekaert and J. Jeener, *J. Magn. Reson. Ser. A*, **113**, 60 (1995).

2. E. L. Hahn, *Concepts in Magn. Reson.*, **9**, 65 (1996).

3. M. P. Augustine and E. L. Hahn, *J. Phys. Chem. B.*, **102**, 8229 (1998).

4. M. P. Augustine and E. L. Hahn, *Mol. Phys.*, **95**, 737 (1998).

5. S. L. McCall and E. L. Hahn, *Phys. Rev.*, **183**, 457 (1969).

6. G. A. Morris and R. Freeman, *J. Am. Chem. Soc.*, **101**, 760 (1979).

7. J. Cavanagh, W. J. Fairbrother, A. B. P. III and N. J. Skelton, *Protein NMR Spectroscopy*, (Academic Press, Inc., San Diego, 1996).

8. R. R. Ernst, G. Bodenhausen, and A. Wokaun, *Principles of Nuclear Magnetic Resonance in One and Two Dimensions*, (Clarendon Press, Oxford, 1992).

9. Unpublished Data

10. Personal communication, Professor Erwin Hahn.

CHAPTER 4

SECOND-ORDER RECOUPLING OF CHEMICAL-SHIELDING AND DIPOLAR-COUPLING IN THE SOLID STATE

4.1 Introduction

Solid State Nuclear Magnetic Resonance (SSNMR) is a powerful method for gaining local structural information, be it inter-atomic distances or bond angles, in large molecular systems. In contrast to X-ray crystallography and neutron diffraction, SSNMR is amenable to systems without long-range order. This makes it possible to gain structural information in systems such as membrane bound proteins [1], amaloydogenic plaques [2], and glasses [3].

In static powder samples, this structural information comes in the form of broad spectral features which often overlap. This leads to spectra with poor resolution in which the potential to gain useful structural information is low. A number of methods have been developed to enhance spectral resolution. Among these are spatial averaging (magic-angle spinning (MAS) and dynamic-angle

spinning (DAS)), spin-space averaging (homo- and heteronuclear decoupling), and site-selective isotropic enrichment.

High-power CW decoupling (spin-space averaging) with cross polarization while spinning at the magic angle (CPMAS) is a very common method of simplifying spectra of powdered samples in the solid state. Provided that the decoupling power is greater than the dipolar interaction and the spinning rate is greater than the chemical shielding anisotropy, under CPMAS conditions one expects to see the narrow lines of an isotropic spectra.

This chapter will focus on an anomalous second-order recoupling of the chemical-shielding and dipolar-coupling tensors that causes a splitting and broadening when a combination of two of these methods is used. In particular, we have investigated the effect of heteronuclear decoupling on an isolated two spin system, ^{1}H-^{15}N, in Tri(trideuteromethyl)-amine (TMA) [4].

4.1.1 The CW Decoupling Quandary

When one runs a CPMAS experiment without decoupling on a powdered sample of TMA at spinning speeds considerably less than the dipolar coupling frequency one obtains a "normal" pattern of spinning side bands indicative of partial averaging. This can be seen pictorially in Figure 4.1.

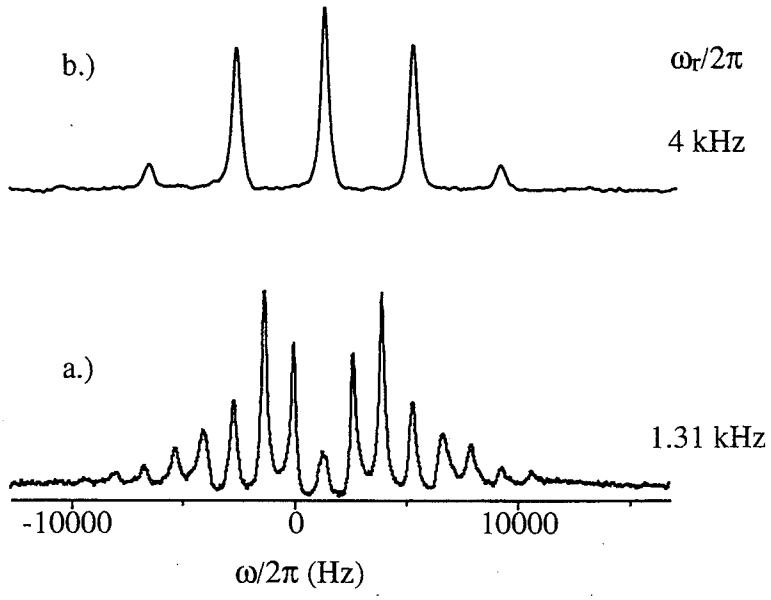

Figure 4.1 ^{15}N MAS spectra of fully ^{15}N-labeled TMA with no decoupling. a.) spinning at 1.31 kHz, b.) spinning at 5 kHz. a.) and b.) show the evenly spaced sharp lines of a normal spinning sideband pattern indicative of partial averaging.

In a.) we see an MAS spectrum where the spinning speed is 1.31 kHz. From this we calculate the dipolar coupling constant to be 15.9 kHz which agrees very well with the literature distance measurement [5]. In b.) we see the result of increasing the spinning speeds to 5 kHz. The side bands spread out, are relatively narrow and are centered about the isotropic value.

This system becomes interesting when we apply a CW decoupling field during acquisition. With the application of a CW decoupling field of 71.5 kHz, while spinning at 5 kHz, we obtain the spectrum depicted in figure 4.2.

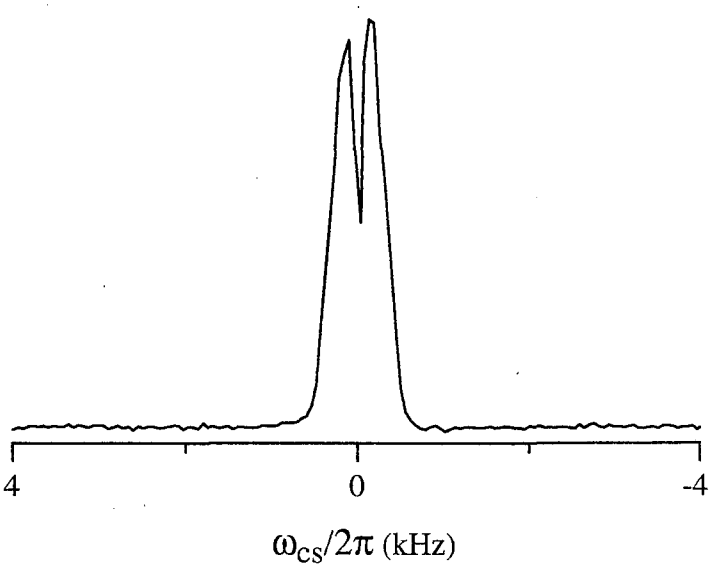

Figure 4.2 ^{15}N MAS spectra of fully ^{15}N-labeled TMA spinning at 5 kHz with a CW decoupling of 71.5 kHz. Under proton CW decoupling the line is split and broadened. This spectrum clearly illustrates that CW decoupling does not give the expected result in isolated heteronuclear two-spin systems.

It is important to note that the decoupling field is much stronger than the dipolar interaction. Under these conditions one would expect to see a single narrow line. What we see is a broad doublet.

We can explain this broadening and splitting as the second-order recoupling of the dipolar-coupling tensor and the proton chemical-shielding tensor. Experiments and theory will be presented to support this explanation. This coupling is useful in that it contains structural information about the relative orientation of the proton chemical-shielding tensor to the dipolar-coupling tensor. This information can be extracted by fitting an experimental spectrum with numerical simulations. If high spectral resolution is required,

removal of this broadening is advantageous. To achieve this we developed more efficient decoupling schemes for isolated spin pairs.

4.1.2 The System

We chose to model site selective isotropic enrichment by designing a molecule with an isolated two-spin system. Here we have created an isolated ^{1}H-^{15}N spin pair in ^{15}N-labeled tri-(trideuteromethyl)-ammoniumchloride (TMA). Depicted in figure 4.3, the average directly bound inter-atomic ^{15}N-^{1}H bond distance measured is 1.06 A.

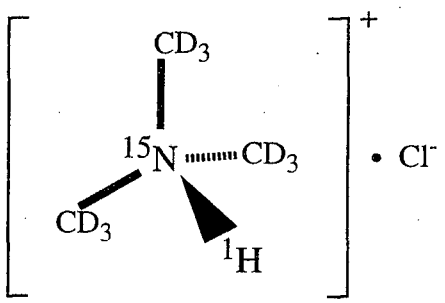

Figure 4.3 Stick drawing of ^{15}N labeled tri-(trideuteromethyl)-ammoniumchloride (TMA). TMA serves as an model of isotropic labeling with an isolated ^{1}H-^{15}N spin pair.

This corresponds to a ^{15}N-^{1}H dipolar-coupling constant of 15.9 kHz. The intramolecular couplings, both heteronuclear and homonuclear, are much smaller. From X-ray crystallography[5] the average ^{15}N-^{15}N and ^{1}H-^{1}H intramolecular

distances are ~6 A. In section 1.2.4 we saw that dipolar couplings scale as a function of r^{-3}. As such ^{15}N-^{15}N dipolar couplings can be estimated as 87 Hz and the ^{1}H-^{1}H couplings are on the order of 800 Hz. This is two to three orders of magnitude smaller than the directly bound species and as such can be safely neglected in our discussion.

4.1.3 Theory

We will start our theoretical discussion of second-order recoupling with the NMR Hamiltonian for a two heteronuclear spin system developed in section 1.3. Here we assume that we are in the double rotating frame and that we have made the appropriate secular approximation. For two spin 1/2 nuclei we can write our Hamiltonian under CW decoupling as,

$$H = H_D + H_{CS(I)} + H_{CS(J)} + H_{RF(I)}. \tag{4.1}$$

Where we have neglected the J-coupling and have no quadrupolar coupling. We can expand each term as,

$$H_D = \omega_D \cdot I_Z S_Z, \tag{4.2}$$

$$H_{CS(I)} = \omega_{CS(I)} \cdot I_Z, \tag{4.3}$$

$$H_{CS(S)} = \omega_{CS(S)} \cdot S_Z, \tag{4.4}$$

$$H_{RF(I)} = \omega_{RF(I)} \cdot I_X. \tag{4.5}$$

Here we have arbitrarily placed our decoupling field along the x-axis. The spatial portions of each interaction are functions of the Euler angles (α,β) and can be written as,

$$\omega_D = \frac{\hbar\gamma_j\gamma_k\mu_0}{\pi r^3}(1-3\cos^2\beta), \tag{4.6}$$

$$\omega_{CS(I,S)} = \gamma B_0\left(\sigma_{iso} + \frac{\delta}{2}\left(\left(3\cos^2\beta - 1\right) - \eta\sin^2\beta\cos 2\alpha\right)\right). \tag{4.7}$$

We can expand this Hamiltonian using the Pauli matrices into a 4 x 4 two spin matrix, where the state labels $|M_I, M_S\rangle$ are included for clarity,

$$H = \frac{1}{2}\begin{bmatrix} |+,+\rangle & |+,-\rangle & |-,+\rangle & |-,-\rangle \\ \omega_D+\omega_S+\omega_I & -\omega_{rf} & 0 & 0 \\ -\omega_{rf} & -\omega_D+\omega_S-\omega_I & 0 & 0 \\ 0 & 0 & -\omega_D-\omega_S+\omega_I & -\omega_{rf} \\ 0 & 0 & -\omega_{rf} & \omega_D-\omega_S-\omega_I \end{bmatrix}. \tag{4.8}$$

Analytically diagonalizing this Hamiltonian we obtain the four eigenvalues,

$$E_{1,2} = \frac{1}{2}\omega_I \pm \frac{1}{4}\omega_{rf}\sqrt{1+\left(\frac{\omega_D+\omega_S}{\omega_{rf}}\right)^2}, \tag{4.9a}$$

$$E_{3,4} = \frac{1}{2}\omega_I \pm \frac{1}{4}\omega_{rf}\sqrt{1+\left(\frac{\omega_D-\omega_S}{\omega_{rf}}\right)^2}, \tag{4.9b}$$

that can be used to deduce the four transition frequencies,

$$\omega_{1,2} = \omega_I \pm \frac{1}{2}\omega_{rf}\left(\sqrt{1+\left(\frac{\omega_D+\omega_S}{\omega_{rf}}\right)^2}+\sqrt{1+\left(\frac{\omega_D-\omega_S}{\omega_{rf}}\right)^2}\right), \tag{4.10a}$$

$$\omega_{3,4} = \omega_I \pm \frac{1}{2}\omega_{rf}\left(\sqrt{1+\left(\frac{\omega_D+\omega_S}{\omega_{rf}}\right)^2}-\sqrt{1+\left(\frac{\omega_D-\omega_S}{\omega_{rf}}\right)^2}\right). \tag{4.10b}$$

To address the relative importance of each transition, we can calculate the time-domain signal. Given an initial density operator, S_x, and a phase sensitive detection operator S_-, the time domain signal is given by,

$$S(D,CS_I,CS_S,t) = \sum_{m=1}^{4} S_m(D,CS_I,CS_S)\cdot e^{i\cdot\omega_m(D,CS_I,CS_S)\cdot t}. \tag{4.11}$$

Using the elements of the transformation matrix used to diagonalize the Hamiltonian in equation 4.8, combined with the detection operator S_-, the corresponding signal intensities can be written as,

$$S_{1,2} = \frac{1}{4} - \frac{1}{4}\left(1+\frac{4\omega_D^2\omega_{RF}^2}{\left(\omega_D^2+\omega_I^2+\omega_{RF}^2\right)^2}\right)^{-1/2}, \tag{4.12a}$$

$$S_{3,4} = \frac{1}{4} + \frac{1}{4}\left(1+\frac{4\omega_D^2\omega_{RF}^2}{\left(\omega_D^2+\omega_I^2+\omega_{RF}^2\right)^2}\right)^{-1/2}. \tag{4.12b}$$

In the limit of strong decoupling, $\omega_{RF}^2 > \omega_D^2, \omega_I^2$, both S_1 and S_2 are small. We will therefore drop the transitions centered at ω_1 and ω_2 in the rest of our discussion. Conversely, the intensities of S_3 and S_4 tend towards 0.5 for strong decoupling fields. These transitions thus play an important role in our discussion. To

analyze the interference of the dipolar-coupling and chemical-shielding tensors in equation 4.10b, we can expand the square root in a power series,

$$\omega_{3,4} = \omega_I \pm \frac{1}{2}\omega_{rf}\left(1+\frac{1}{2}\left(\frac{\omega_D+\omega_S}{\omega_{rf}}\right)^2+\ldots-1-\frac{1}{2}\left(\frac{\omega_D-\omega_S}{\omega_{rf}}\right)^2+\ldots\right). \qquad (4.13)$$

Here we have made the implicit assumption that the decoupling field is much larger than either the dipolar-coupling or chemical-shielding tensors. Truncating this equation after the first two terms, we obtain an approximate expression for the transition frequencies,

$$\omega_{3,4} \approx \omega_I \pm \left(\frac{\omega_D\omega_S}{\omega_{rf}}\right). \qquad (4.14)$$

The $\omega_D\omega_S$ term describes a second-order recoupling of the chemical-shielding and dipolar-coupling tensors. A similar effect is well known in liquid-state NMR as off-resonance decoupling. There an apparently scaled J coupling is obtained by off-resonance irradiation of a coupled heteronuclear two-spin system [6,7]. In that case both J coupling and resonance offset are scalar quantities and as such their product is also a scalar. Off-resonance decoupling in solids results in a coupling of the scalar isotropic resonance offset and the second-rank dipolar-coupling tensor which results in a purely second-rank interaction. This second-rank tensor is averaged out under MAS conditions. The second-order recoupling of the two tensors shows very different properties compared to the recoupling of a tensor and a scalar in off-resonance CW decoupling in solid-state NMR. The

fact that both the dipolar coupling and the chemical shielding are second-rank tensors has new and interesting consequences.

The product of two second-rank tensors can generally be described by a weighted sum of a zeroth-rank, a second-rank, and a fourth-rank tensor [8]. To decompose the tensor products into the sum of tensors and calculate the influence of single-axis rotations of the different components, we have to consider the transformations of both tensors from their respective PAS into a common laboratory-fixed coordinate system.

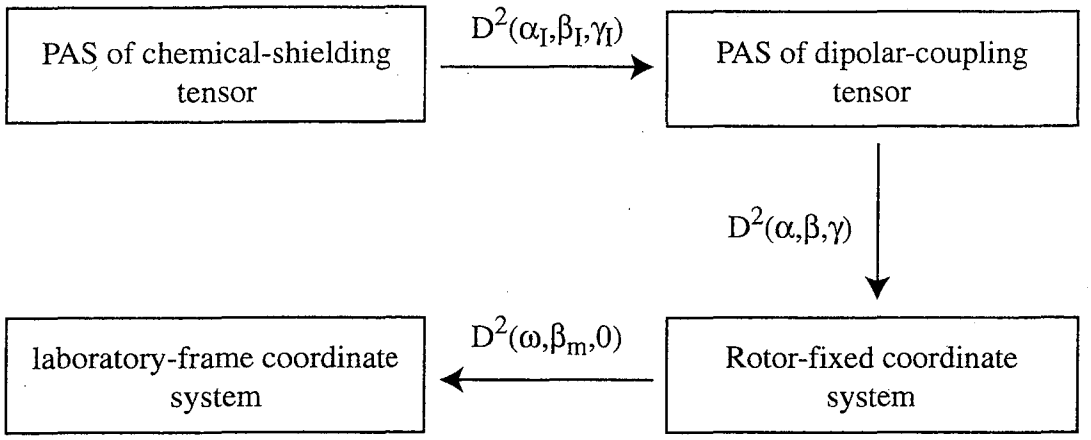

Figure 4.4 Sequence of transformations and Euler angles necessary to rotate the chemical shielding and dipolar-coupling tensors from their respective principal-axis systems into the laboratory fixed coordinate system. The chemical-shielding tensor is first rotated into the PAS of the dipolar-coupling tensor ($\hat{D}^2(\alpha_I,\beta_I,\gamma_I)$), and then both tensors are rotated into the rotor-fixed frame ($\hat{D}^2(\alpha,\beta,\gamma)$). From there the tensors are rotated into the laboratory-fixed frame ($\hat{D}^2(\omega_r t,\beta_m,0)$).

From the PAS of the dipolar coupling tensor both tensors can be rotated into the rotor-fixed frame and subsequently rotated into the laboratory frame. This is seen graphically in figure 4.4. This leads to the following time dependent transformation for the two tensors,

$$\omega_D(t) = \frac{1}{\sqrt{6}} \sum_{n=-2}^{2} D^2_{n,0}(\omega_r t, \beta_r, 0) D^2_{0,n}(\alpha, \beta, \gamma) \cdot \rho^D_{n,0}, \tag{4.15}$$

$$\omega_S(t) = \frac{2}{\sqrt{6}} \sum_{m=-2}^{2} \sum_{m'=-2}^{2} \sum_{m''=-2}^{2} D^2_{m,0}(\omega_r t, \beta_r, 0) D^2_{m',m}(\alpha, \beta, \gamma) \cdot D^2_{m'',m'}(\alpha_I, \beta_I, \gamma_I) \cdot \rho^I_{2,m''}. \tag{4.16}$$

Here we have used the Wigner rotation matrices [8] described in section 1.3.3. The angle β_r is the inclination angle of the rotation axis to the static magnetic field and ω_r is the sample spinning frequency. The set of angles (α,β,γ) describe the orientation of a selected crystallite (powder average), and $(\alpha_I,\beta_I,\gamma_I)$ are the three Euler angles describing the orientation of the I-spin chemical-shielding tensor in the PAS of the dipolar coupling tensor. The dipolar coupling tensor is always axially symmetric and is defined in its PAS in section 1.3.4 as,

$$\rho^D_{2,0} = \sqrt{\frac{3}{2}} \frac{\hbar \gamma_j \gamma_k \mu_0}{\pi r^3}. \tag{4.17}$$

The chemical-shielding tensor components in their PAS as defined in section 1.3.3 are,

$$\rho^I_{2,0} = \sqrt{\frac{3}{2}} \delta_I, \tag{4.18}$$

$$\rho^{I}_{2,\pm 2} = \frac{1}{2}\eta_I \delta_I . \tag{4.19}$$

where δ_I and η_I are the anisotropy and the asymmetry of the chemical-shielding tensor described in section 1.3.3 respectively. We are interested in the time-averaged transition frequencies given by,

$$\begin{aligned} \omega_{3,4} &= \left\langle \omega_{3,4}(t) \right\rangle_{\beta_r} \\ &\approx \left\langle \omega_I \pm \left(\frac{\omega_D \cdot \omega_S}{\omega_{rf}} \right) \right\rangle_{\beta_r} . \end{aligned} \tag{4.20}$$

Where $\langle \cdots \rangle_{\beta_r}$ represents the time average over a full rotor period. Equation 4.20 only has non-vanishing contributions under conditions where m=-n, where m and n are the summation indices from equations 4.15 and 4.16. Under this condition the time average in equation 4.20 can be recast as,

$$\begin{aligned} \omega_{3,4} = & \sqrt{\frac{2}{3}} d^2_{0,0}(\beta_r) \sum_{m'=-2}^{2} D^2_{m',0}(\alpha,\beta,0) \times \sum_{m''=-2}^{2} D^2_{m'',m'}(\alpha_I,\beta_I,0) \cdot \rho^I_{2,m''} \\ & \pm \frac{1}{3\omega_{RF}} \cdot \rho^D_{2,0} \cdot \sum_{j=0,2,4} C(2,2,j;0,0) \cdot d^j_{0,0}(\beta_r) \times \sum_{m'=-2}^{2} D^j_{m',0}(\alpha,\beta,0) \\ & \cdot C(2,2,j;0,m') \times \sum_{m''=-2}^{2} D^2_{m'',m'}(\alpha_S,\beta_S,0) \cdot \rho^I_{2,m''} \end{aligned} \tag{4.21}$$

Here, $C(j_1,j_2,j;m_1,m_2)$ are Clebsch-Gordan coefficients[9] and $d^j_{m,n}$ are the reduced Wigner rotation elements in table 2.1. Equation 4.21 shows that we indeed obtain the sum of three different terms (j=0,2,4) which scale as a zero-rank, a second-rank, and a fourth-rank tensor under single-axis rotation. Setting the

angle of the rotation axis to β_r=0° gives the solution for the static spectrum. If the inclination angle of the rotation axis to the static magnetic field corresponds to the magic angle, all second-rank contributions to the transition frequencies will be averaged. The chemical-shielding tensor of the S spin and the second-rank contribution to the second-order term are thus scaled to zero. Under MAS conditions, only the isotropic portion and scaled fourth-rank tensor contribution will remain. These residual interactions give rise to an isotropic spitting of the line described by the zeroth-rank scalar and an orientation-dependent splitting described by the fourth-rank tensor contribution. It is possible to average both the second-rank and the fourth-rank tensor components in equation 4.21 simultaneously by using either dynamic-angle spinning (DAS) or double rotation (DOR) [10,11,12]. In these experiments the sample is spun about two effective axis. Under these conditions one is able to average both the second-rank and fourth-rank tensor components. The second-order coupling is reduced to its fully isotropic component and will give rise to a spectrum that consists of a sharp doublet.

Although the second-order recoupling contains interesting information concerning the orientation of the two tensors, it is often desirable to remove the splitting to increase the resolution and obtain a single sharp line for each resonance. The simplest way to calculate the Hamiltonian under a multiple-pulse sequence is to use average Hamiltonian theory [13,14]. For CW decoupling with the RF field placed along the x-axis, the average Hamiltonian to first order is given by,

$$\overline{H}^{(0)} = \omega_I \cdot I_z, \tag{4.22}$$

$$\overline{H}^{(1)} = \frac{\omega_D{}^2 + \omega_S{}^2}{2\omega_{RF}} S_X + \frac{2\omega_D\omega_S}{\omega_{RF}} S_X I_Z. \tag{4.23}$$

The first term of equation 4.23 is the second-order isotropic dipolar shift. Since it commutes with the I-spin subspace of the density operator it has no influence on the time evolution of the I spin. The second term describes the second-order recoupling of the chemical-shielding and dipolar-coupling tensors. In the limit of strong decoupling, the result from average Hamiltonian theory is equivalent to the result derived from second-order static perturbation theory. Using the well known fact that symmetric pulse sequence eliminate all odd orders of the average Hamiltonian[13], we can design very simple pulse sequences to remove the second-order recoupling term (first-order average Hamiltonian). The simplest such experiment consists of alternating 2π and -2π pulses. All multiple-pulse sequences used in high-resolution liquid-state NMR also fulfill this symmetry condition and could also be used. Under MAS conditions the length of the pulse sequence is an important consideration. The repetition rate of the sequence should be considerably faster than the mechanical spinning speed of the sample to avoid interferences between the two different averaging processes, [14,15,16]. The phase-alternating sequence and other symmetric sequence will be experimentally analyzed in section 4.4.

The reason that the second-order recoupling of the dipolar-coupling and the chemical-shielding tensors is not as prominent in normal solids is the strong homonuclear dipolar-coupling network among protons. The spin flip-flop terms of the homonuclear dipolar-coupling Hamiltonian lead to an additional

modulation of the heteronuclear dipolar coupling which results in a narrowing of the lines of the decoupled heteronuclear spin. This effect is known as "self-decoupling" [17,18,19].

4.2 Experimental

This section will outline the experimental aspects of the work presented in this chapter. It will start by describing sample preparation techniques and then move on to detail the hardware and software used in both the MAS and DAS studies.

4.2.1 Sample Preparation

Fully deuterated ^{15}N labeled TMA was obtained from Herbert Zimmerman. To produce the ^{1}H-^{15}N spin pair we needed to exchange the labile amide deuterium for a hydrogen atom. To accomplish this the sample was dissolved in a 0.07 M aqueous HCl solution (500 mg/ml). This solution was allowed to stir at room temperature for 30 minutes while the labile deuterium exchanged. After this period the sample was placed under vacuum overnight to remove the excess solvent and recrystalize the now singly protonated TMA. This process yielded fairly regular micro crystals that were used without any further purification. Not surprisingly, we found the TMA to be very air sensitive. Upon

exposure to atmospheric water, the crystal could be visually seen to "moisten" and the sample took on the smell of old fish. Thus, all manipulations of our sample were performed in a glove bag under an inert nitrogen environment.

After recrystalization the sample was pulverized using a small mortar and pestle to form a fine powder. Powdered samples were then placed in either a 7 mm DAS rotor or a 4 mm MAS rotor and sealed. Between experiments the sample rotors were stored in an evacuated round bottom flask to avoid prolonged exposure to the atmosphere.

4.2.2 Magic Angle Spinning Experiments

Magic angle spinning experiments were performed with a home-built spectrometer utilizing a Techmeg Libra pulse programmer and a 7.1 Tesla Oxford superconducting magnet. These studies used a commercial 4 mm MAS two channel Chemagnetics probe. The spinning frequency was controlled using a home-built spinning speed controller.

The experiments under MAS conditions were performed using a standard Harman-Hahn cross-polarization sequence in which the decoupling characteristics were changed depending upon the experiment. This can be seen in figure 4.5.

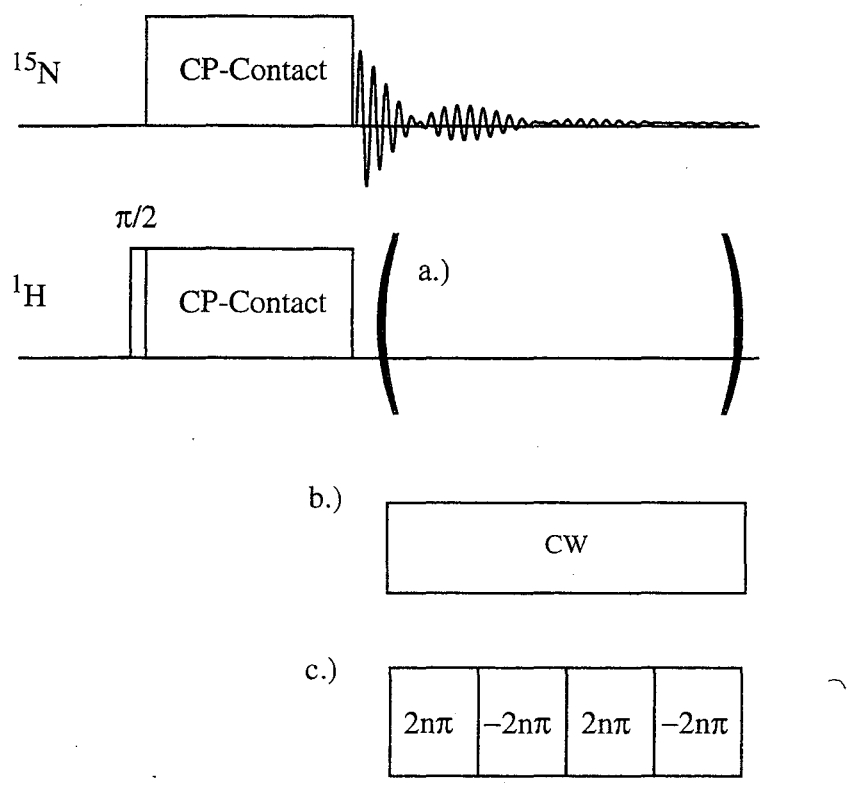

Figure 4.5 The basic Hartmann-Hahn cross polarization experiment with a.) no decoupling during acquisition, b.) CW decoupling during acquisition, and c.) a simple symmetric $2n\pi$ $-2n\pi$ decoupling sequence during acquisition. The basic CP experiment applies a $\pi/2$ pulse to the ^{1}H spins followed by CP-Contact pulses applied to both ^{1}H and ^{15}N. The CP-Contact pulses allow transfer of polarization from the ^{1}H spin reservoir to the ^{15}N spin reservoir when they satisfy the condition $\gamma_H B_{1H}=\gamma_N B_{1N}$.

It should be noted that the relative efficiency of the Hartmann-Hahn matching condition, in our experiments, decreases with increasing spinning speeds. We opted to use standard Hartmann-Hahn matching to make sure that the cross-polarization process does not favor certain crystallite orientations. The spectra reported herein were recorded with a CP contact time of 0.5 msec. Each was recorded as the sum of 1024 signal transients with 256 time points.

4.2.3 Dynamic Angle Spinning Experiments

Dynamic angle spinning experiments were performed with a home-built spectrometer utilizing a Techmeg Libra pulse programmer and a 7.1 Tesla Oxford Instruments superconducting magnet. These studies used home-build variable-angle probe [10,20] with a Doty Scientific 7 mm spinning module.

The pulse sequence used to record the isotropic second-order recoupled spectrum under DAS conditions is shown in figure 4.6. The experiment is implemented as a pure-phase experiment [21] in t_1 and uses States-type processing[22] in ω_1 to distinguish between positive and negative frequencies. Since the second-order recoupled Hamiltonian is quantized along the decoupling field for the S spins, additional storage pulses for the S spins before and after the change of the rotor axis are needed compared to a standard pure-phase DAS experiment[21].

For the 2D-DAS experiment 50 t_1 times were recorded with 256 scans of 256 points in t_2 for each of the two complex data sets. During t_2, phase-alternating 2π pulse decoupling was employed to obtain a narrow line in ω_2. The flipping time to change the angle β_1-37.38° to 79.19° was set to Δ = 100 msec. During this time no noticeable loss of magnetization was observed because the longitudinal relaxation times of both spins are considerably longer than 100 msec. The RF field strength during the CW decoupling in t_1 was ω_{rf}=35.7 KHz.

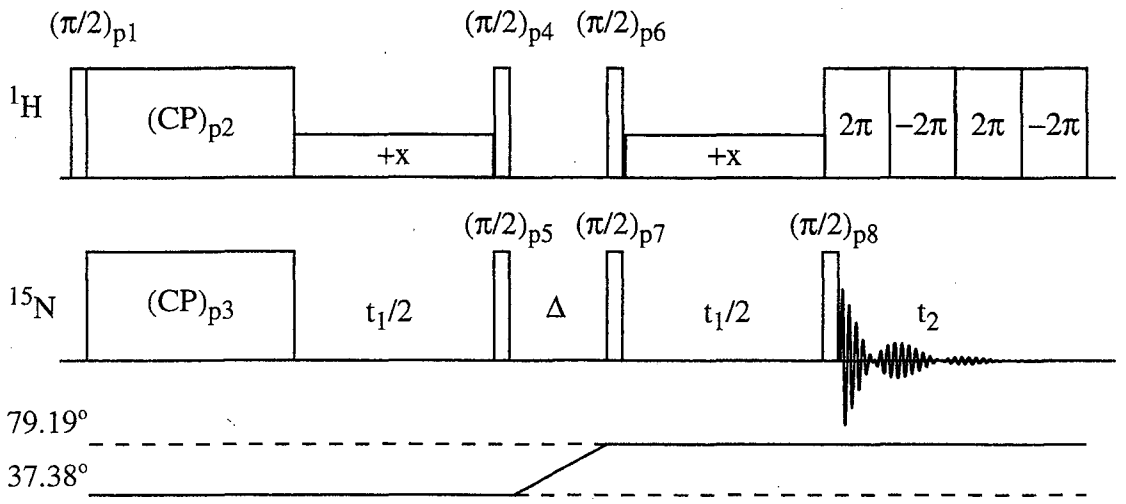

Figure 4.6 Pulse sequence used to measure the DAS spectrum of the second-order recoupling. The pulse sequence implements pure phase[21] during t_1 by storing the appropriate orthogonal components during the change of rotor axis and adding up two data sets modulated as $\cos^2(\omega t_1/2)$ and $\sin^2(\omega t_1/2)$. The RF field strength during the two decoupling periods must be equal. The phase cycle was as follows (phases are given in multiples of $\pi/2$): p_1: 0,2; p_2: 1,3; p_3 and p_8: 0,0,1,1,2,2,3,3; p_4: 1; p_5 and p_7: 0,0,1,1,2,2,3,3,3,3,0,0,1,1,2,2; p_6: 3. The receiver phase was: 2,0,3,1,0,2,1,3. To record the second data set needed for the States-type processing in t_1 the phase of p_3 was shifted by $\pi/2$ while keeping the phase of all other pulses and the receiver unchanged.

4.3 Results

This section will present our experimental results. The first portion of this section will be dedicated to examining the recoupling phenomena. Here we will attempt to add experimental justification for our assertion that the effect we are seeing is due to a recoupling of the chemical-shielding and dipolar-coupling

tensors. As we have stated earlier, it is often advantageous to remove this broadening to raise the overall spectral resolution. In the second portion of this section we will then turn our attention towards methods of removing this broadening via the use of symmetric decoupling sequences and dynamic angle spinning. Again, this data will be used as experimental support of our theoretical assertions.

4.3.1 The Effect

In section 4.1.1 we presented data which at first glance did not make intuitive sense. Under MAS conditions, in "normal" solids, the application sufficiently strong continuous wave (CW) spin-decoupling pulse, should lead to a single sharp line for each resonance. When we introduced CW proton decoupling spectrum showed a broad split line, figure 4.2. Here we will experimentally investigate this deviation from expectation.

4.3.1.1 CW Power

To make sure that the splitting was not simply a result of insufficient decoupling power and investigate the role decoupling power plays in spectral lineshape, we ran a series of CW CPMAS experiments in which the CW decoupling power was varied. These experiments are depicted in figure 4.7

where decoupling field is varied from 8.6 kHz (less than the ^{15}N-^{1}H dipolar coupling) to 71.5 kHz (much greater than the dipolar coupling).

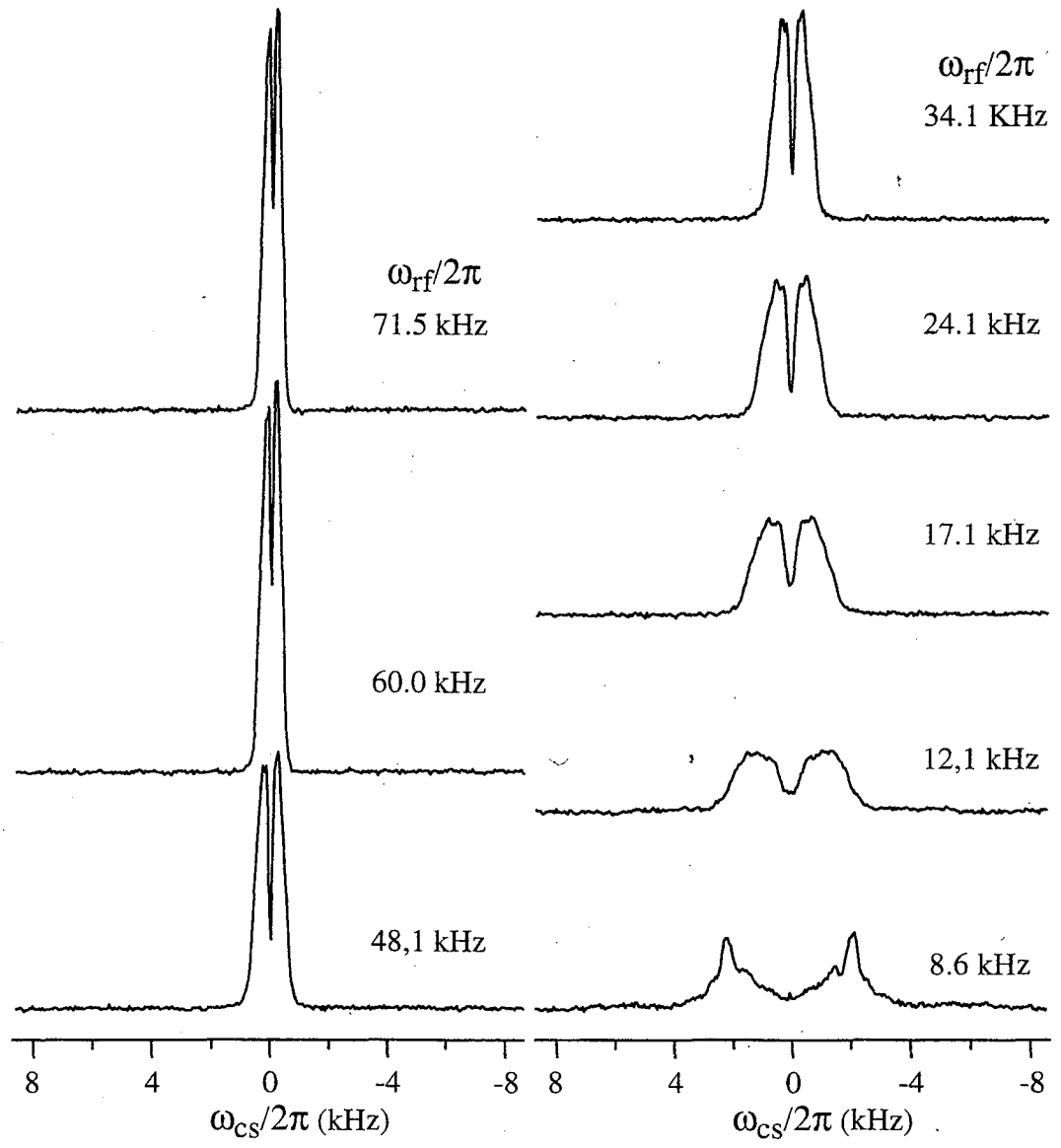

Figure 4.7 15N spectra of 15N-labeled TMA as a function of proton decoupling power. The decoupling field strength was varied from 8.6 kHz to 71.5 kHz. Even for the highest decoupling power the line is still split and rather broad.

The spectra were recorded while spinning at 5 kHz. Even with the highest decoupling field strength we see both a broadening and a splitting. It is our contention that this splitting and broadening are due to the zeroth-rank and fourth-rank tensor contributions to the second-order recoupling that are not averaged out under MAS conditions. Evidence that supports this assertion is seen in figure 4.8.

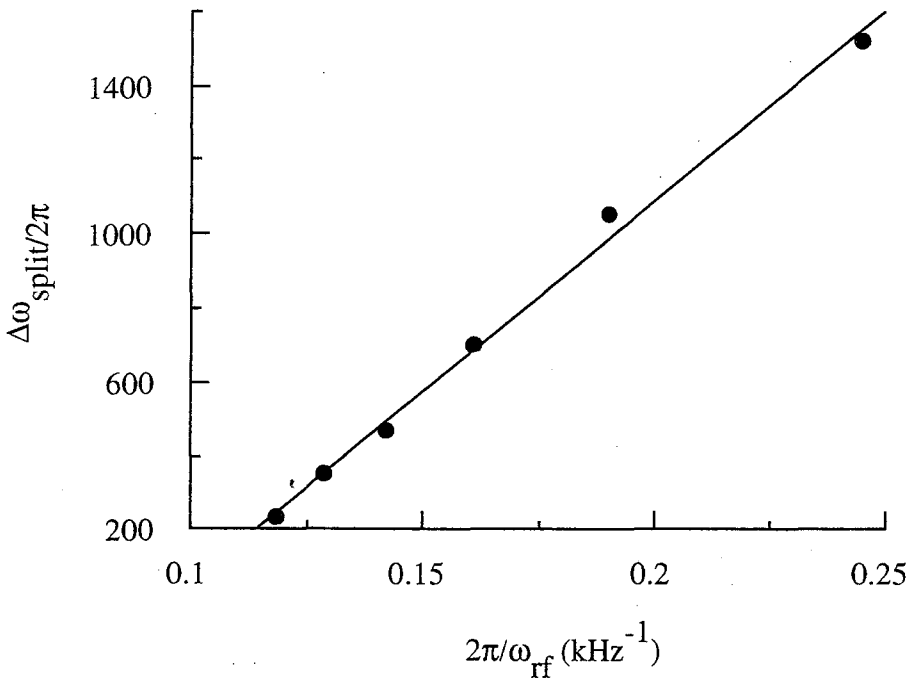

Figure 4.8 Plot of the second-order splitting $\Delta\omega_{split}$ as a function of $1/\omega_{rf}$. The splitting scales linearly with the inverse of the decoupling field strength (r=0.998), as expected from equation 4.14.

Here we see a plot of spectral line width as a function of the inverse decoupling power. From equation 4.14 we expect the recoupling effect (and hence line width) to be linearly related to the inverse decoupling power. This inverse relationship is confirmed (figure 4.8) the data exibit a linear correlation

coefficient, R=0.998. This is direct experimental evidence that we are justified in our theoretical treatment of this problem. Further it shows that we were justified in neglecting all terms higher than second order in the expansion of equation 4.13.

4.3.1.2 CW Spinning

In order to investigate the influence of the spinning speed on the second-order recoupling and rule out rotational-resonance phenomena [23,,24,,25,,26] as a source of observed splitting, we recorded a series CPMAS spectra, with and without a CW decoupling field, as a function of spinning speed. In figure 4.9 we have turned the decoupling field off and see a series of CPMAS spectra as a function of spinning speed. Here we see that as we raise the spinning speed the spinning side bands spread out and the center, isotropic line grows. Again we should note that as the spinning speed increases the CP efficiency decreases which accounts for the decline in overall intensity as we raise the spinning speed. In figure 4.10, with the CW decoupling field held constant at 71.5 kHz, the spinning speed is varied from 4 kHz to 9 kHz.

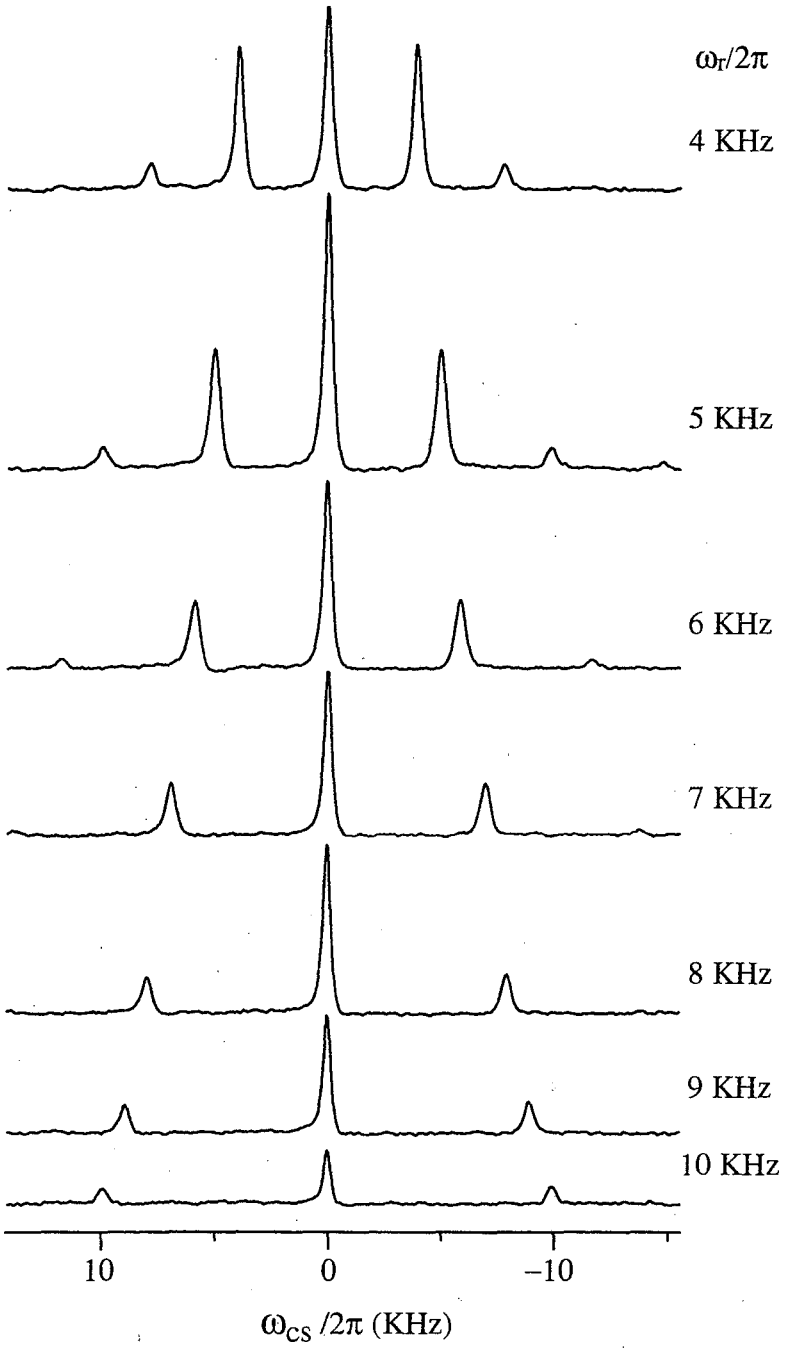

Figure 4. ^{15}N MAS spectra without decoupling at spinning speeds ranging from 4 kHz to 10 kHz. The decrease in the relative spectral intensity as the spinning speed is increased is due to lowered CP efficiency at higher spinning speeds. Without a CW decoupling field we see normal spinning side band pattern.

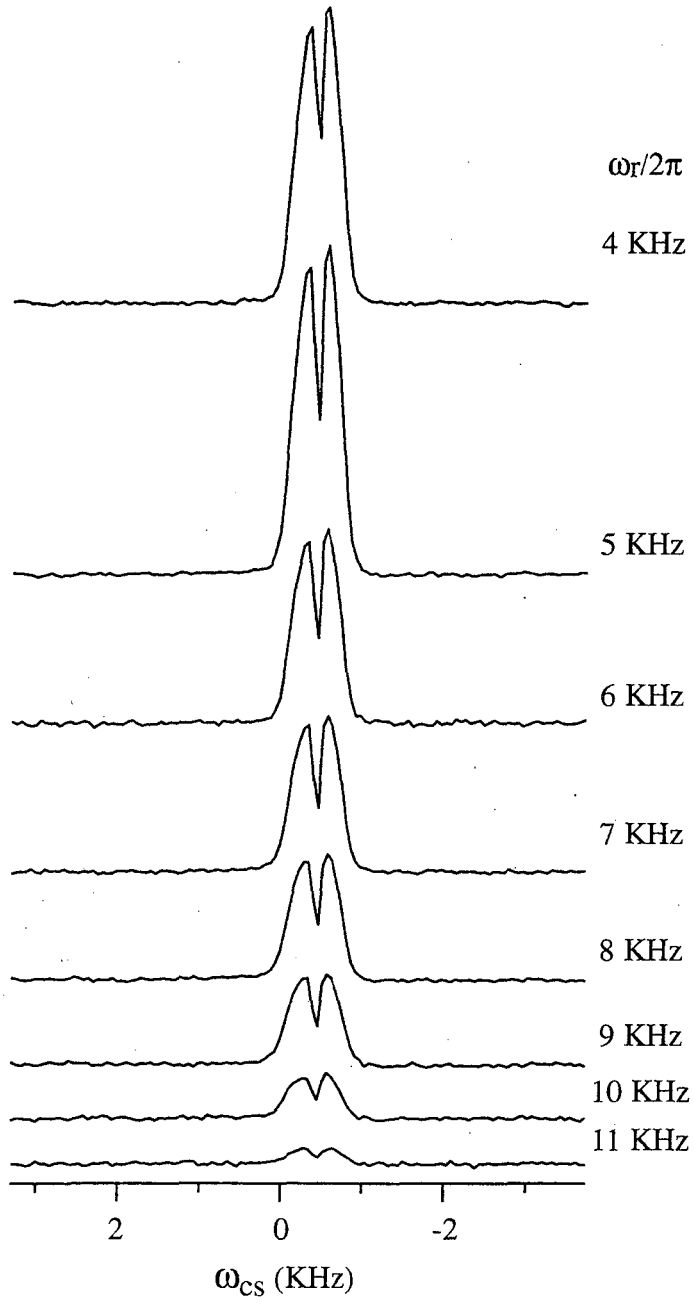

Figure 4.10 ^{15}N MAS spectra under CW proton decoupling with spinning speeds ranging from 4 kHz to 11 kHz. The decoupling field strength was held constant at 71.5 kHz. The width of the line is independent of the MAS spinning speed. Again variations in the line intensities are due to varying cross-polarization efficiencies at different spinning speed.

The spectra are unchanged over the full range of spinning speeds except for an overall decrease in intensity with increasing spinning speeds. This decrease in intensity is explained as above. Most importantly, the line shape clearly is independent of spinning speed. In "normal" solids, when the line width is not dictated by the inhomogenity of the external magnetic field, one would expect the line width to be inversely proportional to the spinning speed. From the narrow line widths in figure 4.9, where we see a CPMAS spectrum without decoupling, we know that in the CW decoupled spectra have line widths that are not dictated by the inhomogenity of the external magnetic field. The insensitivity to spinning speed seen in figure 4.10 is thus evidence that supports the recoupling hypothesis: equation 4.14 shows no dependence on spinning speed.

4.3.1.3 Fits and Simulations

Removing this second-order recoupling is important when one wants to maximize spectral resolution. However, this splitting is inherently information rich. It is dependent upon the relative orientation chemical shielding and diplar coupling tensors. Thus one should be able to back out this orientation from the second-order line shape. This dependence is illustrated in figure 4.11.

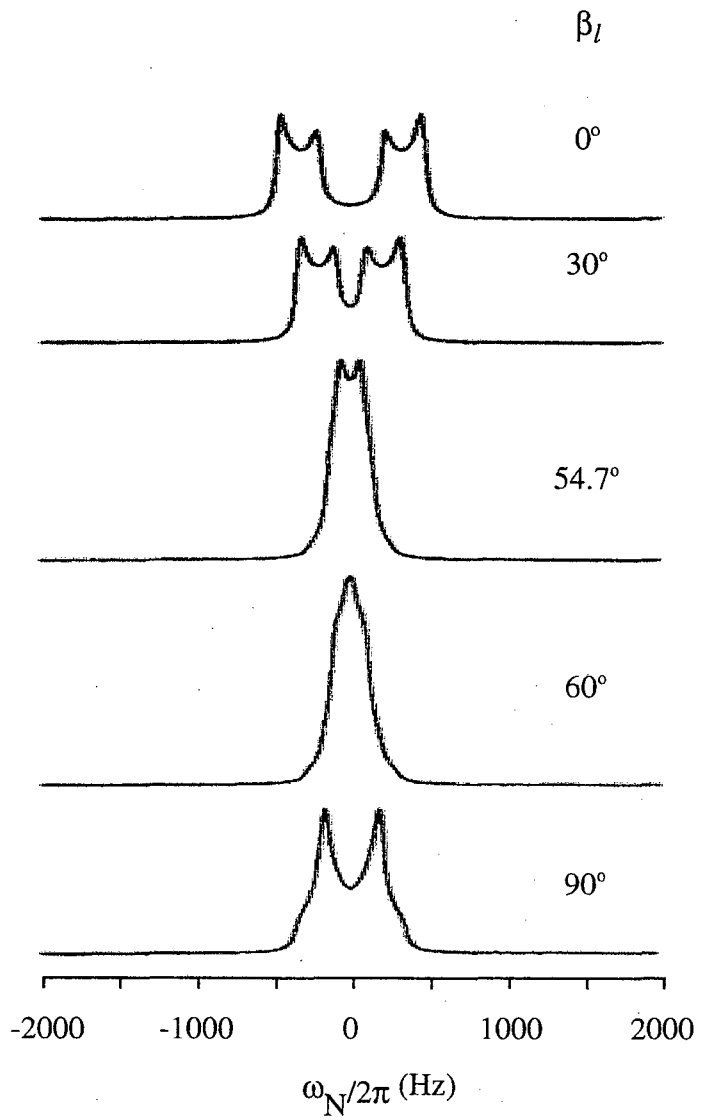

Figure 4.11 Dependence of the second-order recouped spectrum on the orientation of the chemical-shielding tensor relative to the dipolar-coupling tensor. The chemical shielding tensor was assumed to be axially symmetric so only one parameter (β_I) is needed to describe the orientation of the PAS of the two tensors. The line shape of the spectrum depends very strongly on β_I, suggesting that is should be possible to determine the β_I between the two tensors from experimental spectra. The parameters used for these simulations were: $w_{rf}/2\pi$=70 kHz, $\delta_d/2\pi$=20 kHz, $\delta_I/2\pi$=6.8 kHz, and η_I=0.0. The spinning speed was 5 kHz.

These simulations were done as frequency-domain simulations using a decoupling field of 70 kHz using the NMR simulation environment GAMMA [27].

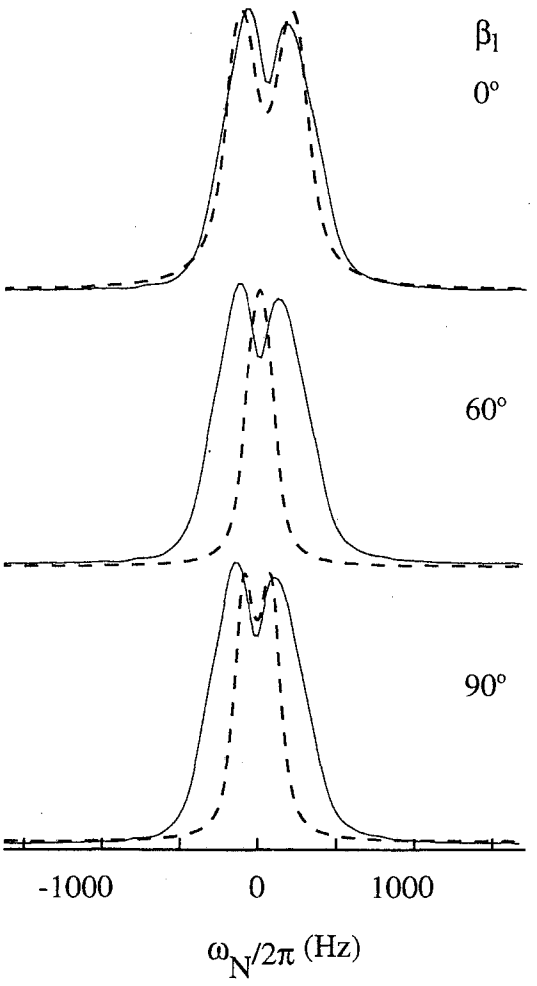

Figure 4.12 Here we see three simulations (dashed lines) with different β_1 values superimposed over the experimental results presented in figure 4.2. The most accurate match is for β_1=0, or colinear dipolar-coupling and chemical-shielding tensors. These simulations used the same parameters described in figure 4.11 but with a decoupling field of 71.5 kHz.

There is clearly a strong line shape dependence on the angle β_l. as expected from equation 4.21. It is not straight forward to predict the line shape from equation 4.21 especially if the chemical-shielding tensor is not axially symmetric. However, the simulations in figure 4.11 show that the variations should be strong enough to allow the determination of the angle between the two tensors from this type of second-order spectrum. Figure 4.12 shows a series of three simulated spectra with varying B_l values superimposed upon an experimental spectrum. From this were able to back out the relative orientation of the chemical-shielding and dipolar-coupling tensors. We saw that they are colinear in this sample. This geometry is well within the range expected from separated local field experiments that measure the relative orientation of the chemical-shielding and dipolar-coupling tensors in a ^{1}H-^{15}N bond pair[28].

4.3.2 Solutions

As pointed out earlier, it is often advantageous to remove the second-order recoupling to achieve higher spectral resolution. This section will offer three mechanisms where by this effect can be either removed or modulated.

4.3.2.1 Symmetric Decoupling

We can eliminate second-order effects in the rotating frame by exchanging standard CW irradiation for a symmetric decoupling. The simplest such pulse

sequence is a series of phase alternating $2\pi x$, 2π-x pulses. Figure 4.13 shows a series of 1D spectra obtained with this type of synchronous phase-alternating decoupling with an RF field strength of 71.5 kHz taken at different spinning speeds. Here we see a narrow ~45 Hz line that varies only slightly over a spinning speed range of 4 kHz to 9 kHz. Clearly the broadening due to the second-order recoupling is removed and we are left with "normal" solids spectra.

A similar simple symmetric decoupling sequence can be constructed out of phase alternating 4π -4π. Figure 4.14 shows a series of 1D spectra obtained with this type of synchronous phase-alternating decoupling with RF decoupling field strength of 71.5 kHz taken as a function of spinning speeds. Again we see the same qualitative behavior. The line narrows, FWHH=45 Hz, but now we see that at higher spinning speeds the decoupling efficiency decreases and the lines broaden. We believe this to be a result of interferences between the spin-space and real-space averaging mechanisms. That is as the decoupling "sequence" begins to be comparable to the cycle time of the rotor interference effects can lead to broadening of the line and give rise to sidebands. This type of interference between two averaging processes is well know and has been described in the literature [14,15,16].

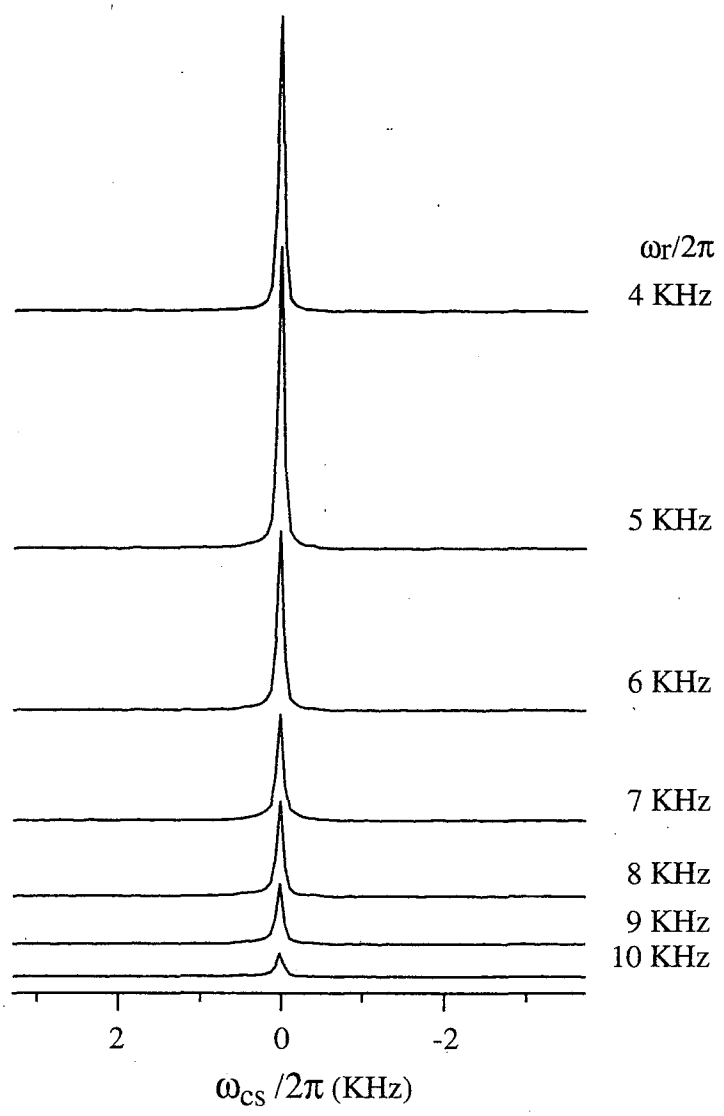

Figure 4.13 ^{15}N MAS spectra under proton decoupling using a phase alternating 2π -2π sequence as a function of spinning speed. The half width at half height is 45 Hz and is independent of spinning speed. The narrowing (1 kHz to 45 Hz) is an indication that the second-order recoupling has been removed. Again, the variation in spectral intensity is due to varying cross-polarization efficiency at different spinning speeds.

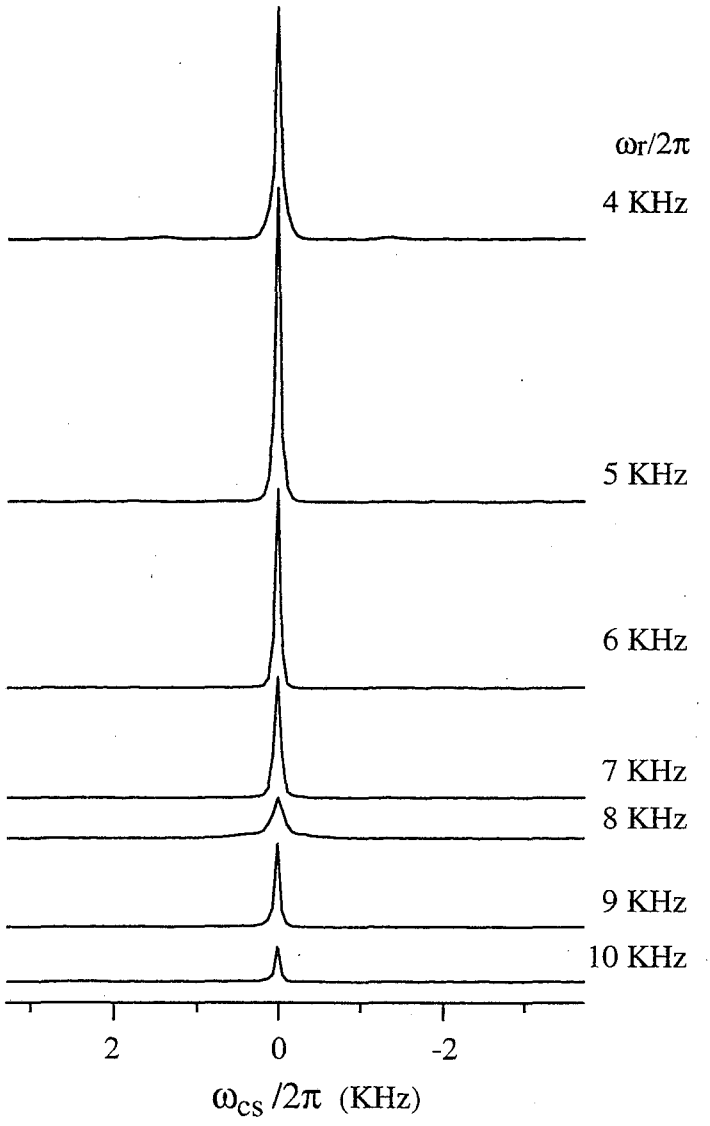

Figure 4.15 ^{15}N MAS spectra under proton decoupling using a phase alternating 4π -4π sequence as a function of spinning speed. The half width at half height is 45 Hz and is independent of spinning speed. The apparent broadening at 8 kHz may be the result of interference between spin and spatial averaging processes.

4.3.2.2 MLEV-4/WALTZ-4

Other simple decoupling schemes have also been implemented. Here we will report on the use of two such decoupling sequences, MLEV-4 [29,30] and WALTZ-4 [31,32]. Each uses a four phase supercycle of composite pulses. The pulse sequence for each decoupling scheme is depicted in figure 4.15.

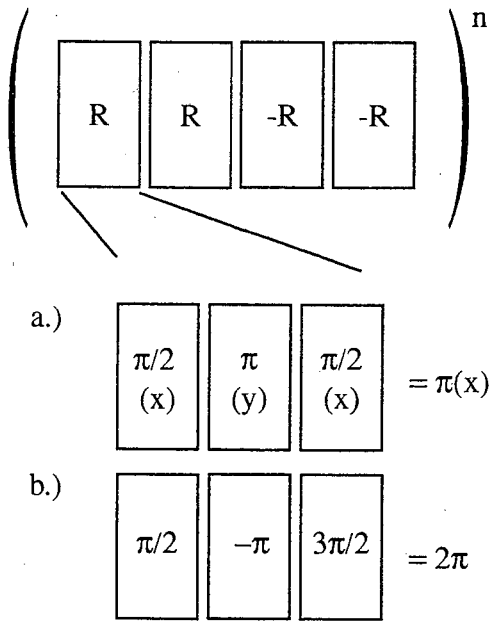

Figure 4.15 MLEV-4 and WALTZ-4 decoupling sequences. Each contains a repeating composite pulse with a four phase supercycle. a.) depicts the three pulses used to form a composite π x pulse in the MLEV-4 supercycle. b.) depicts the three pulses used to form a composite 2π pulse in the WALTZ-4 supercycle.

Figure 4.17 and 4.18 show a series of MLEV-4 and WALTZ-4 decoupled spectra as a function of spinning speed.

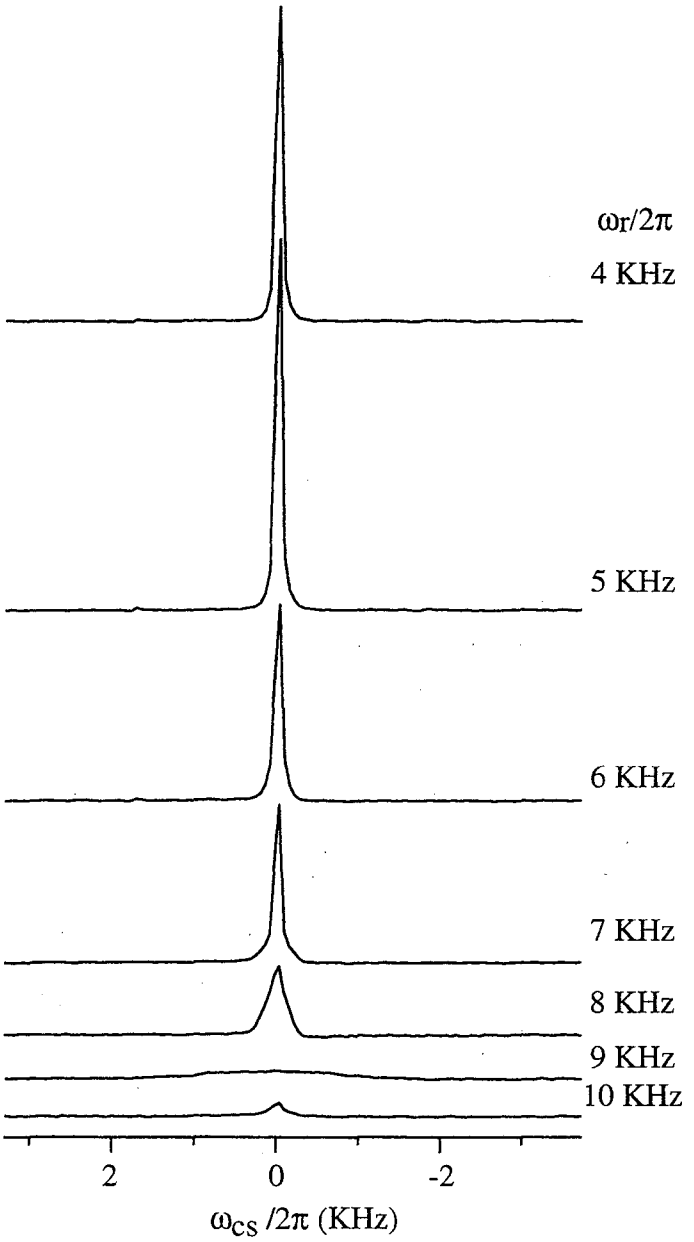

Figure 4.16 ^{15}N MAS spectra as a function of spinning speed under proton decoupling using MLEV-4 decoupling sequence. The half width at half height for the slower spinning spectra is 30 Hz. When the spinning speed is increased the line broadens due to the interference between spin and spatial averaging processes.

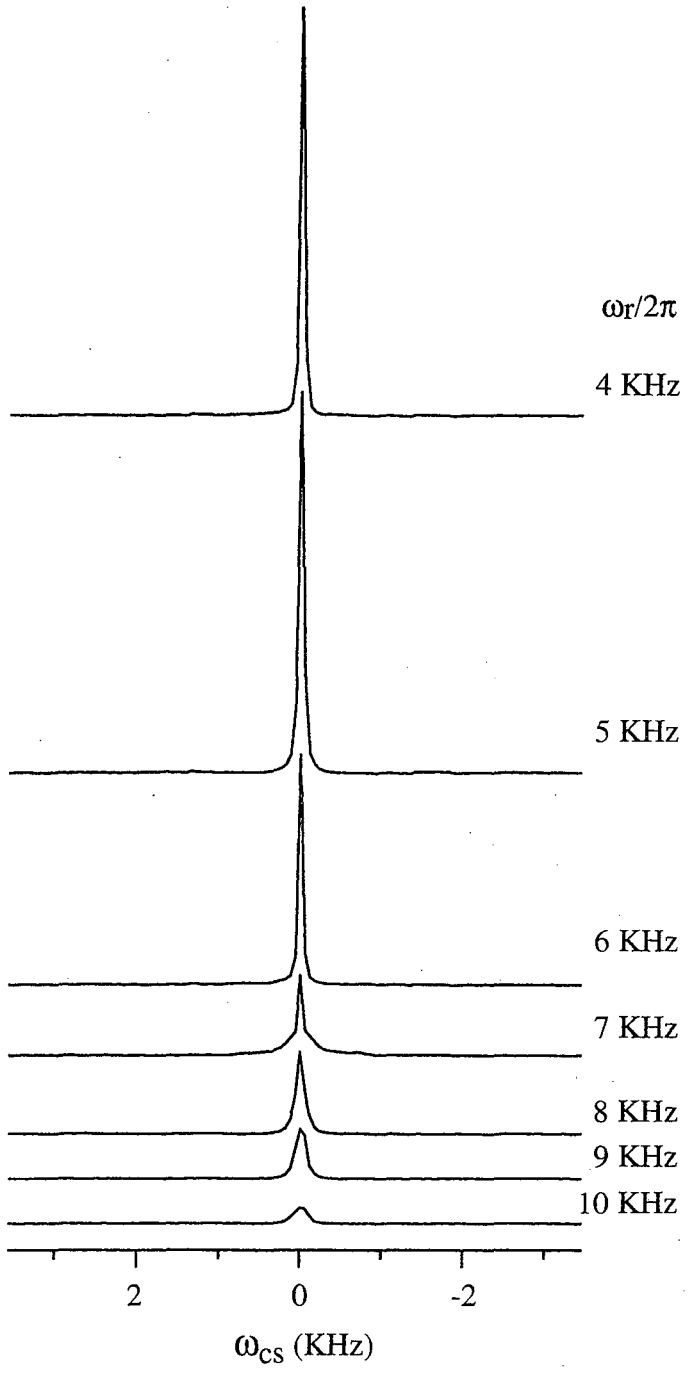

Figure 4.17 ^{15}N MAS spectra as a function of spinning speed under proton decoupling using WALTZ-4 decoupling sequence. The half width at half height for the slower spinning spectra is 30 Hz. Again, the lines broaden at higher spinning speed due to the interference between spin and spatial averaging processes.

While these give slightly narrower lines ~30hz at lower spinning speeds, they become fairly inefficient at higher spinning speeds when the time of the decoupling pulse sequence cycle becomes comparable to the rotor cycle.

4.3.2.3 Dynamic Angle Spinning

Dynamic angle spinning (DAS) and double rotation (DOR) offer a mechanism for simultaneously averaging both the second-rank and fourth-rank tensors components of the second-order recoupling. This has the net effect of keeping only the isotropic zeroth-order component. DAS experiments were performed as described in section 4.2.3. After a hypercomplex Fourier transformation and phase correction, a slice through the highest point in ω_2 along ω_1 was taken and is shown in figure 4.19. A comparison with a MAS spectrum recorded under similar conditions shows a significant narrowing of the line due to the simultaneous averaging of the second-rank and fourth-rank tensors. However, the DAS spectrum still has very broad lines. These may be due to inaccuracies in adjusting the two DAS angles or differences in the CW-decoupling field strengths at the two different rotor orientations. This narrowing is direct support that the effect we are seeing is the result of a fourth-rank interaction. This supports our assertion that we are dealing with second-order recoupling. The spitting obtained by a fit of the DAS spectrum to two Lorentzian lines is $\Delta\omega$=650±100 Hz. It would be advantageous to implement a similar experiment under DOR conditions. Both problems with angle adjustments and RF field strengths would not be present under DOR.

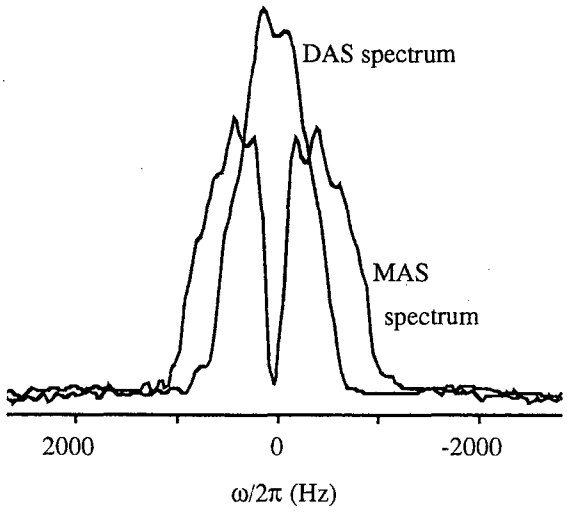

Figure 4.19 MAS and DAS spectra ^{15}N spectra for a decoupling field strength of 35.7 kHz. The MAS spectrum was recorded as a 1D CP CW decoupling spectrum, while the DAS spectrum was recorded with the pulse sequence described in figure 4.19. The 1D spectrum shown is the slice through the highest point in ω_2 along the ω_1 dimension. The DAS spectrum is narrower due to the simultaneous averaging of second-rank and fourth-rank tensor contributions. The splitting of the two lines in the DAS spectrum corresponds to the isotropic value of the second-order recoupling of the chemical-shielding and dipolar-coupling tensors.

4.4 Discussion

We have shown that the second-order recoupling of the dipolar-coupling and the chemical-shielding tensors is an important source of residual broadening in CW-decoupled spectra of isolated two-spin systems. Since this residual

broadening results from the coupling of two second-rank tensors it will not average out under MAS conditions because of the zeroth-rank and fourth-rank tensor contributions. In the case of our model system we have seen a broadening of nearly 1000 Hz when a CW decoupling field of 71.5 kHz is used. The use of a simple phase-alternating sequence, which is symmetric in the sense of the average Hamiltonian theory, removes the second-order broadening in spin systems with weak homonuclear dipolar-coupling networks.

The impact of this second-order recoupling will most visibly be seen in doubly labeled substances that are now more commonly used in the structure determination of peptides in proteins by solid-state NMR. We can estimate the magnitude of the broadening for a ^{13}C-^{15}N spin pair based on the analytical results of equation 4.14. For a one bond distance, a carbon CSA tensor of 9750 Hz, and a decoupling field strength of 70 kHz one obtains a residual linewidth of approximately 200 Hz.

It is also possible to use the second-order recoupling to extract information about the magnitude or the orientation of the principal-axis system of the two interfering tensors from the second-order spectrum. In systems with strongly dipolar coupled protons, the use of off-resonance decoupling, with the effective decoupling field along the magic angle, can reduce the quenching of the second-order recoupling by the homonuclear flip-flop modulations. Such experiments may allow the extraction of structural information from the second-order recoupled spectra even in systems with strong homonuclear dipolar-coupling networks.

REFERENCES

1 S. Oplla, *Nat. Struct. Bio.*, **4**, 845 (1997).

2. D. Selkoe, *Science*, **248**, 1058 (1990), A Goate et al., *Nature*, **349**, 704 (1991).

3. R. M. Wenslow and K. T. Mueller, *J. Phys. Chem B*, **102**, 9033 (1998).

4. M. Ernst, S. Bush, A. Kolbert, and A. Pines, *J. Chem. Phys*, **105 (9)**, 3387 (1996).

5. J. Lingren and I. Olovsson, *Acta Cryst. B*, **24**, 73 (1976).

6. H. J. Reich, M. Jautelat, M. T. Messe, F. J. Weigert, and J. D. Roberts, *J. Am. Chem. Soc.*, **91**, 7445 (1969).

7. B. Birdsall, N.J. M. Birdsall, and J. Feeney, *J. Chem Soc. Chem. Comun*, **1972**, 316.

8. D. M. Brink and G. R. Satchler, *Angular Momentum* (Claredon, Oxford, 1993).

9. M. E. Rose,*Elementary Theory of Angular Momentum* (Dover, New York, 1995).

10. K. T. Mueller, B. Q.Sun, G. C. Chingas, J. W. Zwanziger, T. Terao, and A. Pines, *J. Magn. Reson.*, **86**, 470 (1990).

11. A. Llor and J. Virlet, *Chem. Phys. Lett.*, **152**, 248 (1988).

12. A. Samoson, E. Lippmaa, and A. Pines, *Mol. Phys.*, **65**, 1013 (1988).

13. U. Haeberlen, *High Resolution NMR in Solids-Selective Averaging* (Academic, New York, 1976).

14. U. Haeberlen and J. S. Waugh, *Phys. Rev.*, **175**, 453 (1968).

15. W. P. Aue, D. J. Ruben, and R. B. Griffin, *J. Chem.. Phys.*, **80**, 1729 (1984).

16. D. Suter, A. Pines, J. H. Lee, and B. Drobney, *Chem. Phys. Lett.*, **144**, 324 (1988).

17. M. Mehring, *Principles of High Resolution NMR in Solids* (Springer, Berlin, 1983).

18. A. Abragam, *Principles of Nuclear Magnetism* (Clarendon, Oxford, 1961).

19. A. Abragam and J. Winter, *Comput. Rend.*, **249**, 1633 (1959).

20. M. A. Eastman, P. J. Grandinetti, Y. K. Lee, and A. Pines, *J. Magn. Reson.*, **98**, 333 (1992)

21. P. J. Grandinetti, J. H. Baltisberger, A. Llor, Y. K. Lee, U. Werner, M. A. Eastman, and A. Pines, *J. Magn. Res.*, **103**, 72 (1993).

22. D. J. States, R. A. Haberkorn, and D. J. Ruben, J. Magn. Reson., **48**, 286 (1982).

23. D. P. Raleigh, A. C. Kolbert, T. B. Oas, M. H. Levitt, and R. G. Griffin, *J . Chem. Soc. Faraday Trans.*, 1 **84**, 3691 (1988).

24. T. G. Oas, R. G. Griffin, and M. H. Levitt, *J. Chem.. Phys.*, **89**, 692 (1988).

25. M. H Levitt, T. G. Oas, and R. G. Griffin, *Isr. J. Chem.*, **28**, 271 (1988).

26. A. C. Kolbert, D. P. Raleigh, R. G. Griffin, and M. H. Levitt, *J. Magn. Reson.*, **89**, 133 (1990).

27, S. A. Smith, T. O. Levante, B. H. Meier, and R. R. Ernst, *J. Magn. Reson.*, A **106**, 75 (1994).

28. A. Ramamoorthy, L. M. Giersch and S. J. Opella, *J. Mag. Res. B*, **110**, 102 (1996).

29. M. H. Levitt and R. Freeman, *J. Magn. Reson.*, **43**, 502 (1981).

30. M. H. Levitt, R. Freeman, and T. Frenkiel, *J. Magn. Reson.*, **47**, (1982).

31. A. J. Shaka, J. Keeler, T. Frenkiel, and R. Freeman, *J. Magn. Reson.*, **52**, (1983).

32. A. J. Shaka, J. Keeler, R. Freeman, *J. Magn. Reson.*, **53**, 313 (1983).

Ernest Orlando Lawrence Berkeley National Laboratory
One Cyclotron Road | Berkeley, California 94720

Prepared for the U.S. Department of Energy under Contract No. DE-AC03-76SF00098